

Search for long-lived supersymmetry in final states with jets and missing energy in the CMS detector

Christian Laner Ogilvy
Imperial College London
Department of Physics

A thesis submitted to Imperial College London
for the degree of Doctor of Philosophy

Abstract

An inclusive search for supersymmetry in final states with jets and missing transverse momentum is performed in proton-proton collisions at a centre-of-mass energy of 13 TeV. A data sample corresponding to an integrated luminosity of 35.9 fb^{-1} recorded by the CMS detector in 2016 at the CERN LHC is analysed. The observed signal candidate event counts are found to be in agreement with the standard model expectation. Within the context of simplified models, the masses of promptly decaying bottom, top and mass-degenerate light-flavour squarks are excluded at 95% confidence level up to 1050, 1000 and 1325 GeV, respectively. The gluino mass is excluded up to 1900, 1650 and 1650 GeV for a gluino decaying promptly via the aforementioned squarks. The result is also interpreted in the context of simplified models of split supersymmetry. Lower limits are placed on the mass of a long-lived gluino for a wide range of lifetimes. Gluino masses up to 1750 and 900 GeV are excluded for gluinos with a lifetime of 1 mm and metastable gluinos, respectively. These results provide complementary coverage to dedicated searches for long-lived particles at the LHC.

Declaration

I declare that this thesis is the result of my own work. All work produced by others is referenced appropriately. The analysis strategy described in Chap. 4 was developed collaboratively within a team of researchers, of which I was a key member and large contributor. The interpretation in long-lived supersymmetry described in Chap. 5 is the result of my own independent work.

Christian Laner

The copyright of this thesis rests with the author and is made available under a Creative Commons Attribution Non-Commercial No Derivatives licence. Researchers are free to copy, distribute or transmit the thesis on the condition that they attribute it, that they do not use it for commercial purposes and that they do not alter, transform or build upon it. For any reuse or redistribution, researchers must make clear to others the licence terms of this work

Acknowledgements

Thank you to everyone I have worked with and who has supported me during this journey. Oliver Buchmueller for his supervision and for providing me with this opportunity. Rob Bainbridge, Stefano Casasso, Sarah Malik and Bjoern Penning for their continual support and sharing of knowledge. The entire RA1 team for their hard work and extraordinary teamwork, in particular Mark Baber, Shane Breeze, Matt Citron, Adam Elwood, Ben Krikler and Lucien Lo. Fellow members of CERN and the Imperial HEP group for providing an enriching environment. And last but not least, thank you to my family, particularly my parents and my wife, for their loving and relentless support.

Contents

1. Introduction	1
2. Theory and motivation	3
2.1. The standard model of particle physics	3
2.1.1. Fundamental fermions	5
2.1.2. Fundamental bosons	5
2.2. Beyond the standard model	6
2.3. Supersymmetry	7
2.4. Exotic long-lived particles	9
2.4.1. Split supersymmetry	10
2.5. Simplified models	11
2.6. Status of searches for supersymmetry and long-lived particles . . .	13
3. Experimental setup	14
3.1. The Large Hadron Collider	14
3.2. The Compact Muon Solenoid	16
3.2.1. Tracker	18
3.2.2. Electromagnetic calorimeter	19
3.2.3. Hadronic calorimeter	20
3.2.4. Magnet	21
3.2.5. Muon system	21
3.2.6. Trigger and data acquisition	22
3.3. Event reconstruction	23
3.3.1. Particle flow algorithm	23
3.3.2. Tracks and vertices	24
3.3.3. Muons	24
3.3.4. Electrons and photons	25
3.3.5. Jets	25
3.3.6. Isolation	27

3.3.7. Energy sums	29
3.4. Simulation	29
4. Search strategy	31
4.1. Physics objects	33
4.2. Baseline selection	36
4.3. Standard model backgrounds	38
4.3.1. Electroweak processes	39
4.3.2. QCD processes	40
4.4. QCD background rejection	41
4.4.1. The α_T variable	42
4.4.2. The $\Delta\phi_{\min}^*$ variable	44
4.4.3. The H_T/E_T variable	45
4.5. Event selection	46
4.5.1. Signal region	47
4.5.2. Control regions	48
4.6. Event categorisation	50
4.7. Trigger	54
4.7.1. Signal and control region triggers	55
4.7.2. Trigger efficiency	57
4.8. Data sets and simulation samples	58
4.8.1. Data sets	60
4.8.2. Simulation samples	60
4.9. Corrections to simulation	62
4.9.1. Pileup	62
4.9.2. Jet energy	62
4.9.3. b-tagging	62
4.9.4. Lepton identification, isolation and triggering	64
4.9.5. Trigger	68
4.9.6. Theoretical calculation of V+jets production	68
4.9.7. Initial state radiation in $t\bar{t}$ events	69
4.9.8. Cross-sections	69
4.9.9. Statistical precision at large n_b	70
4.10. Estimation of electroweak background processes	72
4.10.1. The n_{jet} , n_b and H_T dimensions	72
4.10.2. The H_T dimension	74

4.11. Estimation of QCD background processes	75
4.12. Uncertainties on background estimation	77
4.12.1. Uncertainties derived from variations in simulation	79
4.12.2. Uncertainties derived from data-driven closure tests	84
4.12.3. Uncertainties on the \cancel{H}_T distribution	87
5. Results and interpretation	88
5.1. Characterisation of long-lived gluino models	88
5.2. Uncertainties on signal model simulation	89
5.3. Statistical model	92
5.4. Comparison of expected background and observed data	95
5.5. Procedure for setting limits on signal models	96
5.6. Limits on supersymmetry with prompt decays	101
5.7. Limits on long-lived supersymmetry	103
6. Conclusion	110
A. Appendix: Search strategy	112
A.1. Uncertainties on transfer factors derived from variations in simulation	112
B. Appendix: Results and interpretation	122
B.1. Comparison of expected background and observed data	122
B.2. Results under likelihood fit to signal and control regions	130
B.3. Nuisance parameters	133
Bibliography	139
List of figures	146
List of tables	155

Chapter 1.

Introduction

Particle physics seeks to understand the nature of the universe at a fundamental level. The Standard Model (SM) is a theory developed throughout the 20th century that provides the current best description of particles and their interactions. It has been remarkably successful in accurately describing and predicting the results of many experiments. Despite its success, the standard model has been found to be incomplete, as it is not able to explain dark matter and gravity, among other things. One of the main goals in particle physics is therefore to develop a more complete theory that is able to solve the problems of the standard model.

The theory of supersymmetry (SUSY) is a popular extension of the standard model that attempts to do this, by introducing a new set of ‘supersymmetric’ particles. Certain versions of supersymmetry such as ‘Split SUSY’, as well as other theories beyond the standard model, additionally predict the existence of massive long-lived particles.

The Large Hadron Collider (LHC) at the European Organisation for Nuclear Research (CERN) was built with one of the primary purposes to search for new physics such as supersymmetry. The Compact Muon Solenoid (CMS) is one of the particle detectors at the LHC.

The analysis described in this thesis is an inclusive search for supersymmetry in collision events in the CMS detector containing jets and missing energy, a common signature of new physics. Although the search is designed specifically for scenarios involving SUSY particles that decay promptly, the results are also interpreted within the context of split supersymmetry. This is the first-ever long-lived particle interpretation of a search for ‘prompt’ new physics. Such a search is complementary

to dedicated searches for long-lived particles in the cases of relatively short lifetimes (less than 10 ps). The results have been made public in Ref. [1].

This thesis is organised as follows. Chapter 2 provides an overview of the standard model, supersymmetry and exotic long-lived particles, as well as the current status of searches for new physics. Chapter 3 describes the experimental apparatus of the LHC and CMS, as well as the particle reconstruction techniques. Chapter 4 describes the analysis of this search, including the event selection and the background rejection and estimation. Chapter 5 presents the results obtained and the interpretations. Finally, the content of the thesis is summarised in Chapter 6.

Chapter 2.

Theory and motivation

This chapter begins by providing an overview of the standard model of particle physics. The outstanding problems are outlined, and supersymmetry is introduced as a viable extension of the standard model. The motivation for exotic massive long-lived particles is also discussed. The current status of searches for supersymmetry and long-lived particles is presented as a segue into the analysis that forms part of this thesis.

2.1. The standard model of particle physics

The standard model of particle physics is a quantum field theory which describes the fundamental particles of the universe and their interactions. It includes three of the four fundamental forces, namely the electromagnetic, weak nuclear and strong nuclear forces, although it does not incorporate gravity, which at the quantum level only becomes strong at the Planck scale ($\Lambda_{\text{Planck}} \sim 10^{19}$ GeV). The elementary particles in the standard model can be broadly divided into fermions, with half-integer spin, and (gauge and scalar) bosons, with integer spin. The elementary fermions are the constituents of matter in the universe, while the gauge bosons are the force carriers. Every fermion has an antiparticle that has identical properties except for an opposite charge. The standard model particles and their properties are described further in this section and summarised in Tab. 2.1.

Quarks (spin $s = \frac{1}{2}$)			
	1 st gen.	2 nd gen.	3 rd gen.
particle	up (u)	charm (c)	top (t)
charge	$+\frac{2}{3}$	$+\frac{2}{3}$	$+\frac{2}{3}$
mass	2.3 MeV	1.28 GeV	173 GeV
particle	down (d)	strange (s)	bottom (b)
charge	$-\frac{1}{3}$	$-\frac{1}{3}$	$-\frac{1}{3}$
mass	4.8 MeV	95 MeV	4.18 GeV

Leptons (spin $s = \frac{1}{2}$)			
	1 st gen.	2 nd gen.	3 rd gen.
particle	e neutrino (ν_e)	μ neutrino (ν_μ)	τ neutrino (ν_τ)
charge	0	0	0
mass	< 2 eV	< 0.19 MeV	< 18.2 MeV
particle	electron (e)	muon (μ)	tau (τ)
charge	-1	-1	-1
mass	0.511 MeV	106 MeV	1.78 GeV

Gauge bosons (spin $s = 1$)			
Particle	Force	Charge	Mass (GeV)
Photon (γ)	EM	0	0
W^\pm	Weak	± 1	80.4
Z	Weak	0	91.2
Gluon (g)	Strong	0	0

Scalar bosons (spin $s = 0$)			
Particle	Charge	Mass (GeV)	
Higgs (H)	0	125	

Table 2.1.: Fundamental particles of the standard model of particles physics and some of their properties [2].

2.1.1. Fundamental fermions

The elementary fermions are subdivided into quarks and leptons. In each case there are six fermions arranged into three generations of increasing mass, each generation consisting of a doublet of particles.

Quark generations consist of a particle with electric charge¹ $+\frac{2}{3}$ (the up, charm and top quarks) and another with charge $-\frac{1}{3}$ (the down, strange and bottom quarks). Quarks interact via the electromagnetic, weak and strong forces. They are subject to colour confinement and therefore form bound states called hadrons containing either a quark and an antiquark (mesons) or three quarks (baryons).

Lepton generations consist of a particle with electric charge -1 (the electron, muon and tau leptons) and a neutral particle (the electron, muon and tau neutrinos). The neutrinos only interact via the weak force, while the other three leptons can interact both weakly and electromagnetically.

2.1.2. Fundamental bosons

The elementary bosons can be subdivided into gauge bosons and the scalar Higgs boson. The gauge bosons mediate the three fundamental forces, while the Higgs boson provides a mechanism by which the other standard model particles acquire mass.

The photon is the mediator of the electromagnetic interaction. It is neutral and massless. The latter property means that the electromagnetic force has an infinite range. The neutral Z boson and the charged W^+ and W^- bosons are the mediators of the weak nuclear interaction. These particles are massive and hence the weak force is very short-ranged. The gluons (of which there are eight) are the mediators of the strong nuclear interaction. They are massless and electrically neutral. They also carry colour charge and can therefore interact with themselves. This leads to the strong force also being very short-ranged.

The electromagnetic and weak forces can be unified to form the electroweak interaction. The corresponding gauge bosons are the massless W_1 , W_2 , W_3 and B bosons. With the addition of the Higgs field and through spontaneous symmetry

¹Electric charges are quoted in units of the electron charge $e = 1.602 \times 10^{-19} \text{ C}$

breaking [3–5], the W_3 and B bosons mix to form the photon and the Z boson, while the W^\pm bosons are formed through a superposition of the W_1 and W_2 . This process leads to the generation of masses for the W^\pm and Z gauge bosons, which would otherwise be massless. The Higgs field is also able to explain the masses of the quarks and leptons. Until recently, the Higgs boson, the quantum of the Higgs field, was the only remaining undiscovered particle of the standard model. A boson with properties that are consistent with the Higgs boson was discovered by the CMS and ATLAS experiments at the LHC in 2012 [6, 7].

2.2. Beyond the standard model

The standard model has been well tested experimentally and has been found to describe very accurately a wide range of physical phenomena. However, there are a number of inconsistencies with certain experimental observations, as well as various theoretical concerns such as the fact that the SM does not incorporate the gravitational force. Some of the shortcomings of the standard model are described in this section.

One of the experimental inconsistencies is that no particle in the standard model is a viable candidate for *dark matter*. Dark matter is a hypothetical form of matter that constitutes about 27% of the total energy content of the universe [8]. Its nature is unknown and its presence has so far only been inferred indirectly through its gravitational effects. Evidence for the existence of dark matter comes from observations of the rotation curves of galaxies [9], gravitational lensing [10], the cosmic microwave background (CMB) [8, 11], and the Bullet Cluster [12], among others. The most favoured dark matter candidate is a non-baryonic, weakly interacting massive particle (WIMP) which is stable and electrically neutral [13]. Assuming WIMPs interact via the weak force and have a mass of $O(100)$ GeV, one obtains the correct relic abundance at the time of thermal freeze-out in the early universe required to explain the present dark matter content of the universe. This is referred to as the “WIMP miracle”.

According to the standard model, neutrinos are massless. However, neutrinos have been found to oscillate between different flavours, which requires at least two of the neutrinos to have a non-zero mass [14, 15].

The standard model is also not able to explain the predominance of matter over antimatter in the universe. Although charge-parity (CP) violation occurs within the weak sector, it is not sufficiently significant to result in the observed baryon asymmetry.

A theoretical concern with the standard model is a hierarchy problem relating to the relatively small mass of the Higgs boson. The observable mass of the Higgs boson is given by its bare mass plus higher order corrections from fermion loops. These corrections diverge quadratically with the cutoff scale, the energy scale up to which the standard model is assumed to be valid, which is of order of the Planck scale. As the Higgs mass is observed to be around 125 GeV, a high degree of fine-tuning of its bare mass is required to cancel the large corrections, something which is deemed to be unnatural.

A theoretically appealing aspect of a particle physics theory would be the unification of not only the electromagnetic and weak interactions, but also the strong interaction. This would occur at a very high energy scale known as the *Grand Unified Theory* (GUT) scale ($\Lambda_{\text{GUT}} \sim 10^{16}$ GeV). In the framework of the standard model, the three gauge couplings do not intersect at the same energy scale and therefore a unification is not possible.

For these reasons, it is clear that there must exist physics beyond the standard model (BSM). In particular, there may be particles beyond the TeV scale. A more complete theory that is able to address the aforementioned problems is required.

2.3. Supersymmetry

Supersymmetry is a well motivated extension of the standard model that could solve many of its issues [16]. It introduces a new symmetry between fermions and bosons. For every standard model particle, there exists a supersymmetric partner that has identical quantum numbers except for a spin differing by $\frac{1}{2}$. As no supersymmetric particles have yet been observed, supersymmetry must be a broken symmetry, with the masses of SUSY particles being larger than those of their SM counterparts. The names of the superpartners of fermions (sfermions) are prefixed with an “s”, while those of the gauge bosons (gauginos) are suffixed with

Particle	Symbol	Spin
Squarks (up-type)	$\tilde{u}, \tilde{c}, \tilde{t}$	0
Squarks (down-type)	$\tilde{d}, \tilde{s}, \tilde{b}$	0
Charged sleptons	$\tilde{e}, \tilde{\mu}, \tilde{\tau}$	0
Sneutrinos	$\tilde{\nu}_e, \tilde{\nu}_\mu, \tilde{\nu}_\tau$	0
Gluino	\tilde{g}	$\frac{1}{2}$
Neutralinos	$\tilde{\chi}_1^0, \tilde{\chi}_2^0, \tilde{\chi}_3^0, \tilde{\chi}_4^0$	$\frac{1}{2}$
Charginos	$\tilde{\chi}_1^\pm, \tilde{\chi}_2^\pm$	$\frac{1}{2}$
Higgs bosons	h^0, H^0, A^0, H^\pm	0

Table 2.2.: Supersymmetric particles (observable mass eigenstates) within the MSSM and their spin quantum numbers. The first and second groups are the sfermions and (superpositions of) gauginos, respectively. The Higgs bosons are superpositions of higgsinos.

“ino”. Supersymmetric particles are given the same symbol as their SM partner with an added tilde.

The minimal extension of the standard model is known as the Minimal Supersymmetric Standard Model (MSSM) [17]. It contains over 100 free parameters, compared to 19 in the standard model. The new set of supersymmetric particles introduced by the MSSM is summarised in Tab. 2.2. The squarks and sleptons are the scalar superpartners of the standard model fermions, and have a spin quantum number of 0. The standard model gauge bosons have supersymmetric partners with a spin value of $\frac{1}{2}$. The physical mass eigenstates consist of the gluino, the neutralinos, which are superpositions of the neutral gauginos and neutral higgsinos, and the charginos, which are superpositions of the charged gauginos and charged higgsinos. Five scalar Higgs bosons are formed by the mixing of the spin- $\frac{1}{2}$ higgsinos, of which one is the standard model Higgs.

Unlike in the standard model, baryon and lepton number are not necessarily conserved in the MSSM. As this contradicts stringent experimental constraints on the lifetime of the proton [18], this is remedied by introducing a conserved quantity referred to as R-parity:

$$P_R = (-1)^{3B+L+2s}, \quad (2.1)$$

where B is the baryon number, L is the lepton number, and s is the spin quantum number of the given particle. By this definition, all standard model particles have R-parity values of $P_R = +1$ and SUSY particles have $P_R = -1$. A consequence of R-parity conservation is that supersymmetric particles from standard model interactions must be produced in pairs. Another consequence is that a supersymmetric particle can only decay to an odd number of SUSY particles. This implies that the lightest supersymmetric particle (LSP) cannot decay and is therefore stable.

If the LSP is neutral and weakly interacting, it is therefore a viable candidate for dark matter. The LSP is usually assumed to be the lightest neutralino $\tilde{\chi}_1^0$. Supersymmetry is also able to alleviate the hierarchy problem in the standard model. As the higher order correction of the Higgs mass receives contributions of opposite sign from fermions and scalars, the quadratic divergence is cancelled out by the supersymmetric scalar partners of the standard model fermions. Due to supersymmetry being a broken symmetry, there is still a residual logarithmic divergence in the Higgs mass. Naturalness is achieved if the masses of supersymmetric particles are of the order $O(1)$ TeV. Finally, supersymmetry offers a solution to the unification problem. The additional supersymmetric particles enable the gauge couplings of the electromagnetic, weak and strong interactions to be unified at the GUT energy scale.

As the LHC is a hadron collider, the dominant SUSY production cross section is that for coloured particles, namely squarks and gluinos. These are produced in pairs and undergo cascade decays, producing standard model particles and terminating at the LSP. The typical experimental signature would be a large number of energetic jets and an imbalance in momentum due to the invisible LSPs.

2.4. Exotic long-lived particles

There are many theories beyond the standard model that predict the existence of long-lived particles (LLPs). These exotic LLPs have sufficiently large lifetimes that their decays occur at a displaced location from the collision point, which could be within the detector or even outside of it.

There are various ways in which a long-lived particle may arise within a BSM model. This can happen within SUSY if the next-to-lightest supersymmetric par-

ticle (NLSP) is close in mass to the LSP, in which case the NSLP would be long-lived [19]. Long-lived particles also arise in SUSY models with small R-parity violating couplings [20]. A SUSY particle may also be long-lived if its decay occurs via a highly virtual intermediate state, as is the case in *split supersymmetry*, which will be discussed in Sec. 2.4.1. As a final example, exotic LLPs can also arise in Hidden Valley models, in which a large potential barrier between the standard model and the hidden sector suppresses the rate of decay of these particles [21].

A particle with a lifetime τ travels a certain distance before decaying. Its decay time t and decay length d follow an exponential distribution, defined as:

$$p(t) = \frac{1}{\tau} e^{-\frac{t}{\tau}} \quad (2.2)$$

$$p(d) = \frac{1}{\beta c \tau} e^{-\frac{d}{\beta c \tau}} \quad (2.3)$$

where c is the speed of light and $\beta = \frac{v}{c}$ is the particle's velocity.

Long-lived particles can have a wide range of experimental signatures. If they decay inside the detector, this can result in final states containing displaced vertices, leptons, photons or jets, or if the LLP is charged, ‘kinked’ or ‘disappearing’ tracks. If a massive particle is electrically charged and sufficiently long-lived that it traverses the entire detector without decaying, it would appear similar to a muon but would be identifiable by its longer time of flight and unusual rate of energy loss. A long-lived particle may also come to a complete stop inside the detector if it is sufficiently massive and slow-moving. The energy loss would occur through ionisation if it is charged, and through nuclear interactions if it is coloured. A stopped particle could be identified by detecting its decay products during times when there is a large gap between proton bunch crossings or when the proton beam is not in operation.

2.4.1. Split supersymmetry

Split SUSY [22, 23] is a model in which the supersymmetry is broken at an energy scale much higher than the weak scale. This results in the sfermions having masses much larger than the TeV scale (beyond the kinematic reach of the LHC), while the gauginos remain relatively light. Split supersymmetry retains the appealing

aspects of gauge coupling unification and a dark matter candidate, but abandons the hierarchy problem. This is motivated by the recent constraints set by the LHC on natural SUSY (see Sec. 2.6).

Within split SUSY, the decays of gluinos occur via highly virtual squarks and are therefore suppressed, meaning that gluinos are long-lived. The gluino lifetime can be of order picoseconds or longer, which is beyond the hadronisation time scale. The gluino therefore hadronises and forms a bound state containing quarks or gluons known as an R-hadron [24].

The gluino eventually decays to a quark-antiquark pair and an LSP, leading to an experimental signature of displaced jets and an imbalance in momentum. If sufficiently long-lived, the gluino could also decay outside of the detector, in which case the displaced jets would not be observed.

2.5. Simplified models

A wide range of phenomenologies are possible within theories of supersymmetry due to the large number of free parameters. Experimental searches for SUSY are therefore benchmarked and interpreted in a model-independent way using *simplified models* [25, 26]. A simplified model considers only one production and decay mode, and a minimal set of particles. This usually involves the pair production of an initial particle, followed by a decay (or a cascade of decays via an intermediate particle) to standard model particles and the LSP (neutralino).

The results of this search are interpreted using a total of nine families of simplified models, as summarised in Tab. 2.3. The model parameters are the masses of the parent particle (gluino or squark) and the LSP. The so-called T2 models (T2qq, T2bb, T2tt, T2cc) involve the production of a pair of squarks (bottom, top or light-flavour squarks) with the subsequent decay to standard model quarks. Two versions of T2qq are considered, one in which all first and second generation squark masses are degenerate (T2qq_8fold), and one in which only the up squark is light enough to be produced directly (T2qq_1fold). The T1 models (T1qqqq, T1bbbb, T1tttt) involve the pair production of gluinos with subsequent three-body decays to quarks via a virtual squark. Finally, a long-lived version of T1qqqq (T1qqqqLL) is used to interpret the results in the context of split supersymmetry. This consists of the

Model family	Production and decay	Additional assumptions
Production and prompt decay of squark pairs		
T2bb	$pp \rightarrow \tilde{b}\bar{\tilde{b}}, \tilde{b} \rightarrow b\tilde{\chi}_1^0$	—
T2tt	$pp \rightarrow \tilde{t}\bar{\tilde{t}}, \tilde{t} \rightarrow t\tilde{\chi}_1^0$	—
T2cc	$pp \rightarrow \tilde{t}\bar{\tilde{t}}, \tilde{t} \rightarrow c\tilde{\chi}_1^0$	$m_{\tilde{t}} - m_{\tilde{\chi}_1^0} < m_W$
T2qq_8fold	$pp \rightarrow \tilde{q}\bar{\tilde{q}}, \tilde{q} \rightarrow q\tilde{\chi}_1^0$	$m_{\tilde{q}} = m_{\tilde{q}'}, \tilde{q} = \{\tilde{u}, \tilde{d}, \tilde{s}, \tilde{c}\}$
T2qq_1fold	$pp \rightarrow \tilde{q}\bar{\tilde{q}}, \tilde{q} \rightarrow q\tilde{\chi}_1^0$	$m_{\tilde{q}(\tilde{q} \neq \tilde{u})} \gg m_{\tilde{u}}$
Production and prompt decay of gluino pairs		
T1bbbb	$pp \rightarrow \tilde{g}\tilde{g}, \tilde{g} \rightarrow \tilde{b}\tilde{b}^* \rightarrow b\bar{b}\tilde{\chi}_1^0$	$m_{\tilde{b}} \gg m_{\tilde{g}}$
T1tttt	$pp \rightarrow \tilde{g}\tilde{g}, \tilde{g} \rightarrow \tilde{t}\tilde{t}^* \rightarrow t\bar{t}\tilde{\chi}_1^0$	$m_{\tilde{t}} \gg m_{\tilde{g}}$
T1qqqq	$pp \rightarrow \tilde{g}\tilde{g}, \tilde{g} \rightarrow \tilde{q}\tilde{q}^* \rightarrow q\bar{q}\tilde{\chi}_1^0$	$m_{\tilde{q}} \gg m_{\tilde{g}}$
Production and decay of long-lived gluino pairs		
T1qqqqLL	$pp \rightarrow \tilde{g}\tilde{g}, \tilde{g} \rightarrow \tilde{q}\tilde{q}^* \rightarrow q\bar{q}\tilde{\chi}_1^0$	$m_{\tilde{q}} \gg m_{\tilde{g}}, \tilde{g}$ long-lived

Table 2.3.: Summary of the simplified SUSY models used to interpret the result of this search.

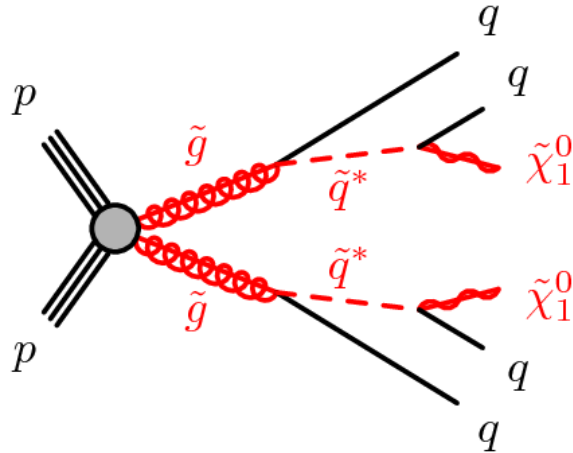


Figure 2.1.: Feynman diagram of long-lived gluino pair production, with each gluino decaying as $\tilde{g} \rightarrow q\bar{q}\tilde{\chi}_1^0$ via a virtual squark \tilde{q}^* .

production of a pair of long-lived gluinos, with each gluino decaying (via a virtual light squark) to a pair of light quarks and the LSP. A Feynman diagram of this process is illustrated in Fig. 2.1. This simplified model contains three parameters, namely the masses of the gluino and the LSP, and the lifetime (expressed as $c\tau$) of the gluino.

2.6. Status of searches for supersymmetry and long-lived particles

Strong constraints have been placed by searches at the LHC on SUSY models with promptly decaying particles. Gluino and stop squark masses have been excluded up to approximately 2 TeV and 1 TeV, respectively [27–31]. This constrains the possibility of natural supersymmetry rather significantly.

However, there is also the possibility that supersymmetric particles may be long-lived, as is the case of the gluino in the scenario of split supersymmetry discussed in Sec. 2.4.1. Dedicated searches for exotic long-lived particles have therefore become more prominent at the LHC. Gluino lifetimes between 10 ps ($c\tau = 1$ cm) and 100 ns ($c\tau = 100$ m) have been excluded up to gluino masses in the range 1800–2400 GeV by a search in events with displaced vertices and missing energy in the ATLAS experiment [32]. A search for jets from stopped gluinos in the CMS experiment has excluded the range of lifetimes between 100 ns ($c\tau = 100$ m) and 100 hours ($c\tau = 0.01$ light-years) for gluino masses up to 1385 GeV [33]. Finally, the results of a CMS search for metastable gluinos (in the form of charged R-hadrons), that have lifetimes larger than the scale of the detector ($\tau \gtrsim 10$ ns, or $c\tau \gtrsim 10$ m), exclude gluino masses up to 1850 GeV [34].

The search presented in this thesis has been optimised for prompt decay signatures and does not employ specialised reconstruction techniques for long-lived particles. Nevertheless, it remains sensitive to events with LLPs and provides a complementary coverage to dedicated LLP searches, in particular for short lifetimes, as will be discussed in Chap. 5.

Chapter 3.

Experimental setup

This chapter provides a description of the various components of the Large Hadron Collider and the CMS detector. The techniques employed to reconstruct the particles that are produced in the proton collisions are discussed, as well as the event simulation method.

3.1. The Large Hadron Collider

The LHC at CERN is a circular accelerator and collider of protons (and lead ions). It is 27 kilometres in circumference, and is situated on the border between France and Switzerland near Geneva, approximately 100 metres underground. It was designed to investigate the standard model and search for new physics.

The accelerator complex at CERN is illustrated in Fig. 3.1. The particle acceleration occurs in various stages. First, hydrogen atoms from a gas bottle are stripped of their electrons and the resulting protons are accelerated to 50 MeV in the Linear Accelerator 2 (LINAC 2). These protons are then injected into the Proton Synchrotron Booster (PSB) to increase their energy to 1.4 GeV. This is followed by the Proton Synchrotron (PS), where the protons reach 25 GeV, and the Super Proton Synchrotron (SPS), which further accelerates them to 450 GeV. The protons then finally arrive at the LHC, where they are accelerated by radio frequency cavities up to an energy of 6.5 TeV, and are steered and focussed by superconducting magnets. During this process, the protons are also collected into bunches of approximately 115 billion protons each that are 25 ns apart. The total number of proton bunches circulating within a given fill of the LHC is 2808.

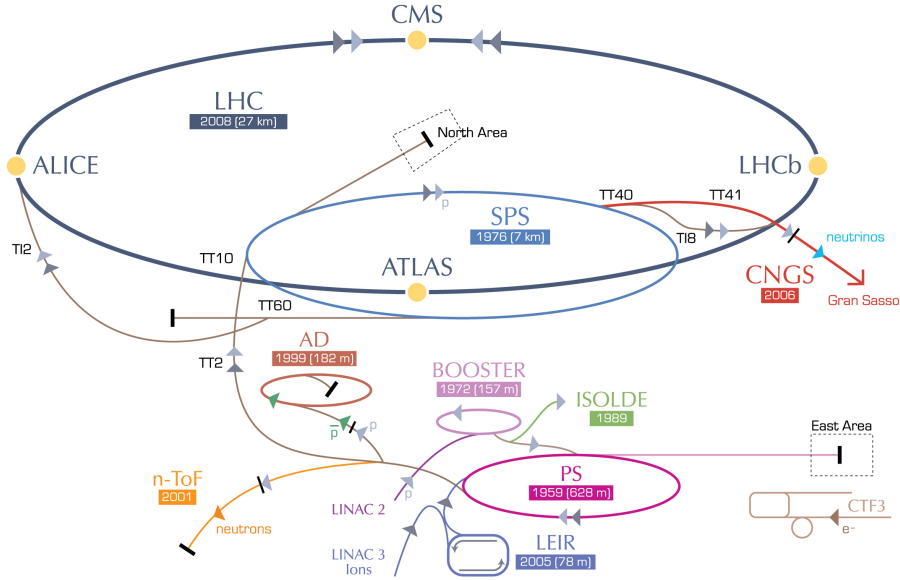


Figure 3.1.: The accelerator complex at CERN leading to the LHC [35]. The various accelerators (LINAC 2, PSB, PS, SPS, LHC) and detectors (CMS, ATLAS, LHCb, ALICE) are described in the text.

The LHC consists of two beam pipes in which the protons are circulated in opposite directions. The protons are made to collide at a centre of mass energy of 13 TeV at four points on the ring, where the CMS [36], ATLAS [37], LHCb [38] and ALICE [39] detectors are situated. CMS and ATLAS are both general purpose detectors, while LHCb and ALICE are focussed on b-physics and heavy ion physics, respectively.

For a process with a production cross section σ , the expected number of events per unit time is related to the instantaneous luminosity L by the relation:

$$\frac{dN}{dt} = \sigma L. \quad (3.1)$$

The instantaneous luminosity is proportional to the number of proton bunches, the number of protons per bunch and the revolution frequency, and is inversely proportional to the transverse size of the beam [2]. For the 2016 running conditions, the average instantaneous luminosity of the LHC was approximately $10^{34} \text{ cm}^{-2} \text{ s}^{-1}$, which resulted in an average number of interactions per bunch crossing (referred to as pileup) of ~ 20 . The total expected number of events of a process in a certain

time T is given by:

$$N = \sigma \int_0^T L \, dt = \sigma L_{\text{int}}, \quad (3.2)$$

where the integral of the instantaneous luminosity over this time is called the integrated luminosity L_{int} , and is a measure of the amount of data collected.

3.2. The Compact Muon Solenoid

The CMS detector is one of the two general purpose detectors at the LHC along with ATLAS, and was designed with the main goal of searching for the Higgs boson as well as for new physics beyond the standard model. The detector is cylindrical and consists of several layers of subdetectors and a solenoid magnet that are used to track, identify and measure the energy of particles such as electrons, photons, muons and hadrons. It extends up to a pseudorapidity of $|\eta| \approx 5$, providing an almost complete coverage in solid angle. This is important when reconstructing the momentum of a weakly interacting particle via the ‘missing momentum’ in an event. The detector is approximately 22 m in length and 15 m in diameter, and weighs about 14,000 tonnes. The layout of the CMS detector is shown in Fig. 3.2, and a cross-sectional view is given in Fig. 3.3, illustrating the various components of the detector, which will be described in this section.

The tracker forms the first layer of the detector closest to the collision point. It is used to reconstruct the trajectories of charged particles within the magnetic field and measure their momenta. Following this is the electromagnetic calorimeter (ECAL), which is used to absorb and measure the energies of electrons and photons. The next layer is comprised of the hadronic calorimeter (HCAL), which detects the more penetrating hadrons. The 3.8 T superconducting solenoid surrounds the tracker and calorimeters. Muons are able to penetrate the magnet and calorimeters and are detected by the muon chambers, which are interspersed with the steel return yoke of the magnet in the outermost layer of the CMS enclosure. Finally, collision events of interest are read out by a trigger system.

A right-handed coordinate system is defined with the origin at the centre of the detector (which is approximately the interaction point). The x -axis lies horizontally towards the centre of the LHC ring, the y -axis points vertically upwards, and

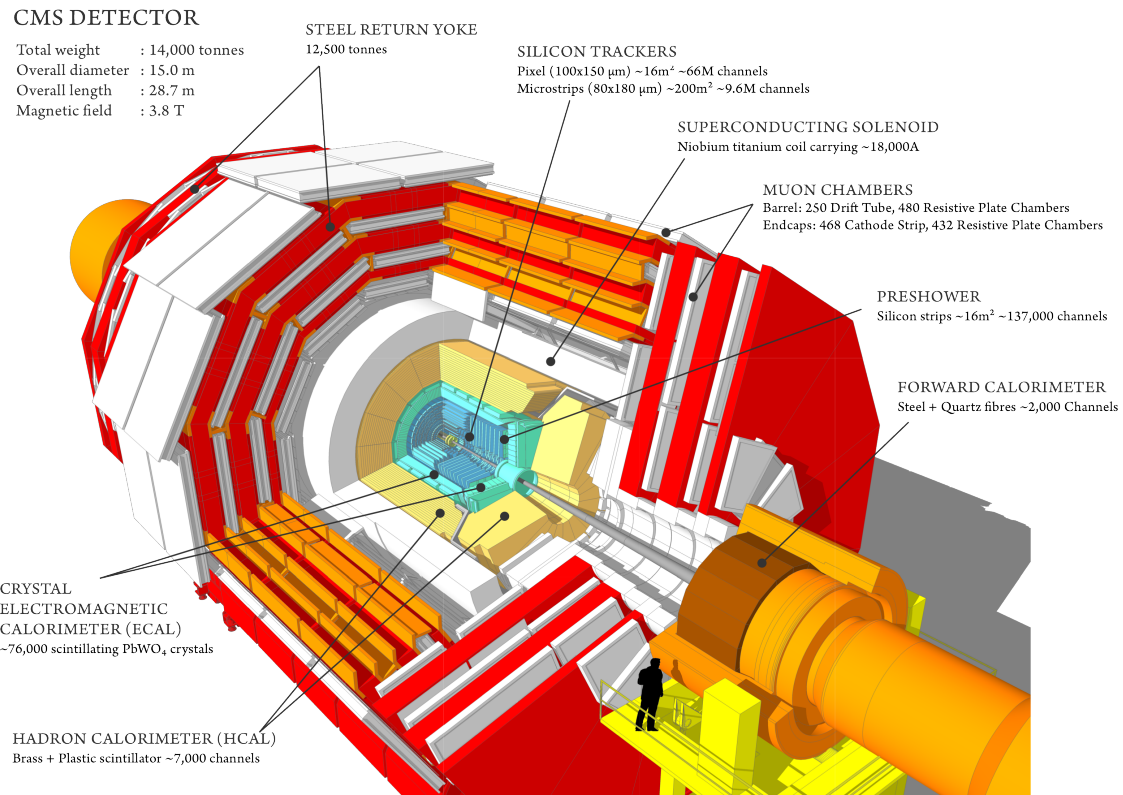


Figure 3.2.: Layout of the major components within the CMS detector. These are described in the text.

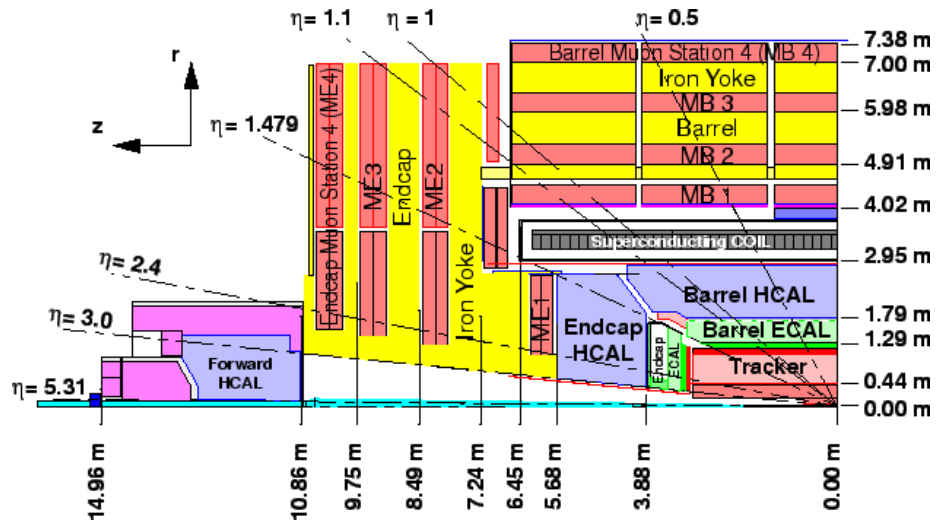


Figure 3.3.: One quarter cross-sectional view (in the r - z plane) of the CMS detector, indicating lines of constant pseudorapidity and the dimensions of various components.

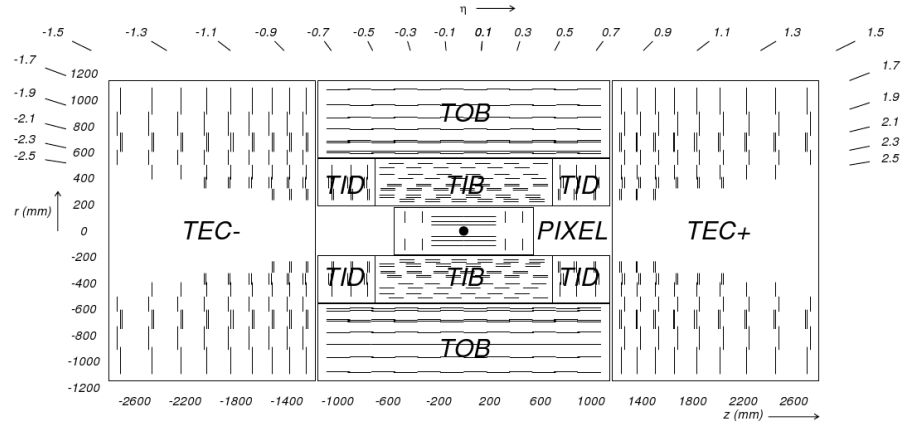


Figure 3.4.: Schematic cross-sectional view (in the r - z plane) of the CMS tracker [36]. The tracker modules are indicated by the black line segments.

the z -axis points along the beam direction. An azimuthal angle ϕ is defined that lies in the transverse x - y plane. The cylindrical radial coordinate is labelled r . A polar angle θ is measured from the z -axis and is related to pseudorapidity by $\eta = -\ln \left[\tan \left(\frac{\theta}{2} \right) \right]$.

3.2.1. Tracker

The CMS tracker consists of a silicon pixel detector located closest to the interaction point ($r < 20$ cm) and silicon strip detectors surrounding this. The more granular pixels are used to cope with the higher particle fluxes that are present near the interaction point, as well as to provide a precise vertex reconstruction, including secondary vertices from the decays of long-lived particles such as b-hadrons. At larger radii the particle flux is lower such that strip detectors can be used instead. There are a total of 66 million silicon pixels and 9.6 million silicon strips covering an area of about 200 m². The arrangement of tracker modules is illustrated in Fig. 3.4.

The pixel detector comprises 3 barrel layers and 2 endcap layers. Each pixel is 100 μm × 150 μm in size. The spatial resolution is approximately 10 μm in the r - ϕ plane and 20 μm in the z direction.

The barrel section of the strip detector comprises the Tracker Inner Barrel (TIB) consisting of 4 layers, and the Tracker Outer Barrel (TOB) consisting of 6 layers. The strips range in size from 10 cm × 80 μm in the TIB to 25 cm × 180 μm in the TOB. The endcap region of the strip detector is made up of the Tracker End Cap

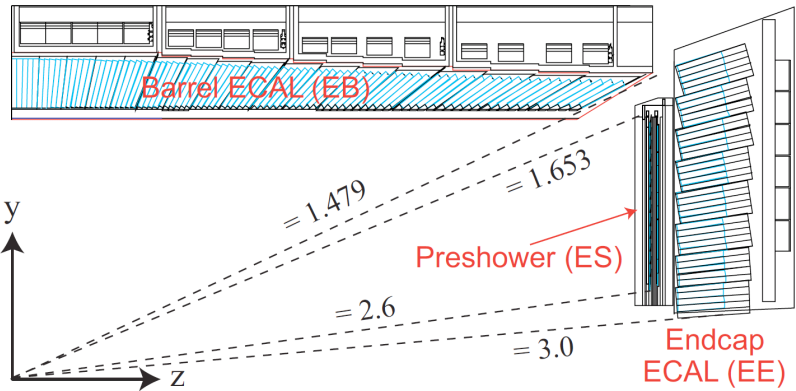


Figure 3.5.: Schematic cross-sectional view (in the r - z plane) of the CMS electromagnetic calorimeter, showing the arrangement of crystals in the barrel, endcap and preshower [36].

(TEC) consisting of 9 disks, and the 3 Tracker Inner Disks (TID) that lie between the TIB and the TEC.

The tracker is able to record a hit of a charged particle with $p_T > 1$ GeV with an efficiency of over 99%. The transverse momentum resolution $\frac{\Delta p_T}{p_T}$ is approximately 2% for particles with $p_T = 100$ GeV.

3.2.2. Electromagnetic calorimeter

The CMS ECAL consists of over 75,000 lead tungstate (PbWO_4) crystals. These are distributed in the ECAL Barrel (EB) and ECAL Endcap (EC), which cover the pseudorapidity ranges of $|\eta| < 1.48$ and $1.48 < |\eta| < 3$, respectively. The ECAL is illustrated in Fig. 3.5. The energy resolution $\frac{\Delta E}{E}$ of the ECAL is approximately 0.3% for high energy electrons.

The crystals in the barrel have a front-face size of $22 \text{ mm} \times 22 \text{ mm}$ and a length of 23 cm. The scintillation light produced by the electromagnetic showers is collected by silicon avalanche photodiodes in the barrel and vacuum phototriodes in the endcaps that are glued to the ends of the crystals.

The ECAL Preshower (ES) detector is placed in front of the endcaps. It is composed of two alternating layers of lead radiator and silicon strip sensors and helps to distinguish between prompt photons and photons produced in the decays of neutral pions.



Figure 3.6.: One quarter cross-sectional view (in the r - z plane) of the CMS detector, showing the location of the hadronic calorimeter barrel (HB), endcap (HE), outer (HO), and forward (HF) regions [36].

3.2.3. Hadronic calorimeter

The CMS HCAL is a sampling calorimeter consisting of alternating layers of brass absorber and plastic scintillator. The scintillation light is collected by hybrid photodiodes. The HCAL is divided into the HCAL Barrel (HB), which covers the central region of $|\eta| < 1.4$, the HCAL Endcap (HE), covering the pseudorapidity range $1.3 < |\eta| < 3$, the Outer HCAL (HO), which is located in the barrel region behind the solenoid magnet, and the Forward HCAL (HF) which covers the forward region $3 < |\eta| < 5$ and is placed at a distance in z from the interaction point of about 11 m.

The calorimeter cells in the HB have dimensions of $\Delta\eta\Delta\phi = 0.087 \times 0.087$. The purpose of the HO is to capture hadronic showers that leak past the HB, increasing its effective thickness to over 10 interaction lengths. The HF is designed to capture very forward particles and, due to the increased particle fluxes in this region, is instead made of steel absorber and quartz fibers. In this case hadronic showers produce Cerenkov radiation that is detected by photomultiplier tubes.

The energy resolution of the ECAL and HCAL combined has been measured in a test beam and can be parameterised as [40]:

$$\left(\frac{\Delta E}{E}\right)^2 = \left(\frac{84.7\%}{\sqrt{E}}\right)^2 + (7.4\%)^2, \quad (3.3)$$

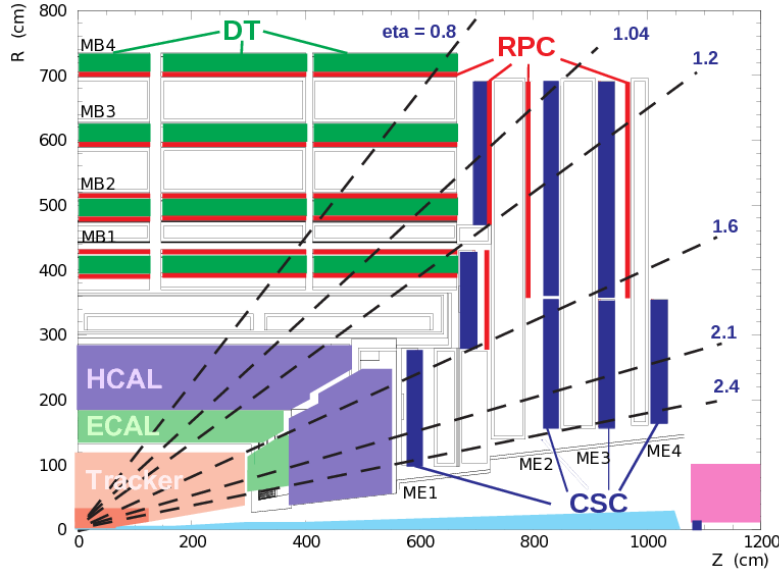


Figure 3.7.: One quarter cross-sectional view (in the r - z plane) of the CMS muon system, showing the location of the drift tube (DT), cathode strip chamber (CSC) and resistive plate chamber (RPC) subsystems [36].

where E is the energy of the incident particle in units of GeV.

3.2.4. Magnet

The CMS magnet is a superconducting solenoid magnet producing a 3.8 T magnetic field. It is made of niobium-titanium and has a length of 12.9 m and a diameter of 6 m. A high magnetic field strength was chosen to provide a good charge identification and transverse momentum resolution even for very energetic charged particles. The return yoke of the magnet is made of steel and is interleaved with the muon chambers.

3.2.5. Muon system

The CMS muon system employs three types of gaseous ionisation detectors, that are placed in layers interleaved with the magnet return yoke. It consists of the Muon Barrel (MB), covering the pseudorapidity range $|\eta| < 1.2$, and the Muon Endcap (ME), covering the range $0.9 < |\eta| < 2.4$. The layout of the muon system is illustrated in Fig. 3.7.

The barrel region is made up of drift tubes (DT). Cathode strip chambers (CSC) instrument the endcaps where particle fluxes are higher. Resistive plate chambers (RPC) are used in both the barrel and endcap regions for redundancy. These have a coarser spatial resolution than DTs and CSCs but provide a faster temporal resolution, which is beneficial for triggering purposes and for a precise bunch crossing determination.

The transverse momentum of muons is measured via a combination of the muon system and the tracker. The momentum resolution $\frac{\Delta p_T}{p_T}$ of the combined measurement is approximately 1% (4%) in the region $|\eta| < 0.8$ for muons with a transverse momentum of 10 (1000) GeV.

3.2.6. Trigger and data acquisition

The crossing of proton bunches at the LHC occurs at a rate of 40 MHz. This results in a potentially large amount of data that is not computationally feasible to process and store. In any case, the majority of collisions consist of QCD soft scattering processes rather than electroweak or BSM processes and can largely be discarded. A two-level triggering system is employed in the CMS experiment, consisting of a hardware-based Level 1 (L1) trigger (L1T) and a software-based High Level (HL) Trigger (HLT), to select events of interest such as those containing a large amount of missing energy or particles with large transverse momentum, and reduce the data rate to a more manageable ~ 1 kHz.

The Level 1 trigger is based on custom electronic systems and reduces the event rate to 100 kHz. To meet the latency budget of $3.2 \mu\text{s}$, it employs coarse information from the calorimeters and muon detectors and simplified reconstruction algorithms. The L1T consists of an L1 calorimeter trigger which reconstructs electrons, photons, jets and missing transverse energy, and an L1 muon trigger which reconstructs muons. These objects are passed to the L1 Global Trigger which makes a decision to pass the event to the HLT based on whether the objects satisfy certain requirements on quantities such as the transverse momentum.

Events that are accepted by the L1T are passed to the high level trigger, which reduces the data rate down to ~ 1 kHz. The HLT consists of a large farm of processors located at ground level. It uses full-granularity data from all subdetectors,

including the tracker, to reconstruct objects with a performance that is close to that offline. The HLT is discussed further in Sec. 4.7.

Events that are accepted by the HLT are reconstructed and stored using the Worldwide LHC Computing Grid (WLCG), a distributed computing system making use of a tier hierarchy [41]. This allows the data (and simulation samples) to be processed, stored and analysed at multiple sites across the world.

3.3. Event reconstruction

The hits and energy deposits in the CMS subdetectors need to be combined in order to reconstruct and identify all physics objects in an event such as electrons, muons, photons, hadrons, jets and missing energy. The event content can then be analysed further for the purpose of, for example, a search for BSM physics, as will be discussed in Chap. 4. The various reconstruction and identification algorithms are described in this section.

3.3.1. Particle flow algorithm

Electrons, photons, muons, charged hadrons and neutral hadrons are all reconstructed by the Particle Flow (PF) algorithm by combining information from all subdetectors [42].

First, tracks in the inner tracker and in the muon system are reconstructed, and energy deposits in the calorimeter cells are grouped into clusters. Muons are identified by matching tracks in the inner tracker and in the muon system. Electrons are then identified by matching inner tracks with compatible energy clusters in the ECAL. Charged hadrons are similarly identified through the matching of tracks with HCAL clusters. Finally, photons are identified by energy deposits in the ECAL that are not matched to any tracks, and neutral hadrons are similarly identified by unmatched HCAL clusters.

More details on the reconstruction of each of these objects are provided in the following sections. These *PF particles* then form the basis for the reconstruction of jets and missing energy.

3.3.2. Tracks and vertices

The trajectories of charged particles in the tracker are reconstructed using the Combinatorial Track Finder (CTF) algorithm [43]. A similar procedure is followed to reconstruct tracks in the muon system. The algorithm starts by forming initial track candidates, or *seeds*, based on combinations of two or three hits in the inner layers of the tracker. A seed defines an initial estimate of a particle’s helical trajectory and is required to be compatible with originating from the collision region. Using a Kalman filter, compatible hits from successive tracker layers are added to the track and the trajectory parameters are updated at each layer. Another Kalman filter is then used to fit the final sequence of hits and smooth the estimated trajectory. Finally, various quality criteria are imposed on the reconstructed tracks, such as a minimum on the number of layers that have hits and the χ^2 value of the fit, to discard fake and duplicate tracks. The whole process is repeated six times, with the hits associated with reconstructed tracks removed in subsequent iterations. The track finding efficiency of the CFT algorithm is approximately 95% for pions with $p_T > 100$ GeV travelling through the barrel region, and almost 100% for muons.

The reconstructed tracks are then clustered to identify the locations of the various proton-proton interactions, known as interaction vertices [43]. The location of the *hard scatter*, referred to as the *primary vertex*, is defined by the vertex with the largest sum of the squared transverse momenta of the associated tracks. The other vertices are attributed to pileup. Secondary vertices from the decays of long-lived particles such as b-hadrons may be identified in further reconstruction steps.

3.3.3. Muons

Two different approaches are followed to reconstruct muons. The first is an outside-in algorithm that begins with a track in the muon system and attempts to match it with a compatible track in the inner tracker. If a match is found, a fit to the hits in both detectors is performed using a Kalman filter to determine the muon’s trajectory. Muons that are reconstructed in this way are called *global muons*. The second approach is an inside-out algorithm that begins with a track in the tracker and extrapolates it and attempts to find at least one compatible hit in the muon system. These tracks are referred to as *tracker muons*.

The tracker muon algorithm is particularly useful for reconstructing muons with low transverse momentum ($p_T \lesssim 5$ GeV) as these often do not leave enough hits in the muon system to be reconstructed as muon tracks. The global muon algorithm, on the other hand, provides an improved momentum resolution for high p_T muons as hits over a larger range are employed and the full bending power of the CMS magnetic field is taken advantage of.

3.3.4. Electrons and photons

Interactions with the tracker material cause electrons to lose energy via bremsstrahlung radiation and photons to convert into electron-positron pairs. This leads to electromagnetic showers in the ECAL that tend to be spread out (in the case of electrons, the energy deposits are narrow in η and wide in ϕ). The energy deposits in the ECAL crystals that are within a certain window in η and ϕ of a local maximum seed crystal are aggregated to form *superclusters*. Instead of using a Kalman filter, the electron trajectories in the tracker are reconstructed using a Gaussian Sum Filter (GSF) algorithm, which is able to account for large energy losses due to bremsstrahlung radiation [44]. Electrons are then identified by an ECAL supercluster that is compatible with a GSF track, whereas photons are identified via unmatched superclusters.

3.3.5. Jets

Due to the nature of the strong force, when a quark or gluon is produced it immediately fragments and hadronises, leading to a collimated spray of hadrons known as a *jet*. In this search, jets are reconstructed by clustering Particle Flow particles using the anti- k_T sequential recombination algorithm [45]. This algorithm is both infrared safe and collinear safe, meaning that the set of reconstructed jets remains unchanged in the case of a soft gluon emission or a splitting of a gluon into two collinear gluons.

A sequential recombination algorithm is based on a distance between pairs of particles d_{ij} and between particles and the beamline d_{iB} . These are defined for the

anti- k_{T} algorithm as:

$$d_{ij} = \min \left(\frac{1}{p_{\text{T}i}^2}, \frac{1}{p_{\text{T}j}^2} \right) \frac{\Delta R_{ij}^2}{R^2} \quad (3.4)$$

$$d_{iB} = \frac{1}{p_{\text{T}i}^2} \quad (3.5)$$

where $p_{\text{T}i}$ is the transverse momentum of particle i , $\Delta R_{ij} = \sqrt{(\eta_i - \eta_j)^2 + (\phi_i - \phi_j)^2}$ is the distance between particles i and j in the η - ϕ plane, and $R = 0.4$ defines the radius of the jet in η - ϕ space.

The algorithm begins by computing all distances d_{ij} and d_{iB} . If one of the d_{ij} is the smallest distance of all, particles i and j are combined into a new particle (or pseudo-jet) by taking the vector sum of their momenta. If instead one of the d_{iB} is the smallest distance, particle i is classified as a jet and removed from subsequent steps. The process is then repeated (starting again by recomputing all distances) until no particles remain.

As the jet reconstruction algorithm clusters all PF particles, isolated leptons and photons may be classified as jets. To avoid this, a *cross-cleaning* procedure is performed in which reconstructed jets that are within $\Delta R < 0.4$ of an isolated muon, electron or photon (isolation will be defined in Sec. 3.3.6) are excluded from the event.

Jet energy corrections

The energies of reconstructed jets typically differ from the true energy of the original quark or gluon due to a non-uniform and imperfect resolution of the detector. The measured transverse momentum of a jet $p_{\text{T}}^{\text{raw}}$ is corrected to account for this via a sequence of multiplicative correction factors (the output of each step is the input to the next) according to [46]:

$$p_{\text{T}}^{\text{corr}} = p_{\text{T}}^{\text{raw}} C_{\text{offset}} C_{\text{sim}} C_{\text{rel}} C_{\text{abs}} \quad (3.6)$$

The first correction is an offset correction C_{offset} that subtracts the energy contributions from electronics noise and particles originating from pileup vertices. The

second is a correction derived from simulation C_{sim} and is given by the ratio of reconstructed and generator-level jet p_{T} . It is derived as a function of p_{T} and η . The third and fourth components are the relative and absolute corrections, C_{rel} and C_{abs} , that are used to correct for remaining small discrepancies in the jet energies measured in data as a function of η and p_{T} , respectively. The overall correction factor (given by the product of the four correction terms) is found to be in the range of 1-1.1 (depending on η) for jets with transverse momentum $p_{\text{T}} = 100 \text{ GeV}$.

b-tagging

A number of BSM models include the associated production of, or decays to, top and bottom quarks. It is therefore advantageous to be able to identify jets that originate from a bottom quark, a process known as *b-tagging*.

Hadrons containing bottom quarks have a lifetime of about 1.5 ps, and therefore travel a few millimetres before decaying. This can be observed experimentally as a jet containing several tracks that originate from a *secondary vertex* that is displaced from the primary vertex.

The Combined Secondary Vertex (CSV) algorithm is employed to perform b-tagging [47]. It consists of an artificial neural network taking a number of input variables related to the secondary vertex (such as the displacement and invariant mass) and the displaced tracks (such as the impact parameters). The output discriminator of the neural network is a value between 0 and 1 which can be thought of as the probability that the given jet originates from a bottom quark. Figure 3.8 demonstrates the ability of the algorithm to discriminate between jets originating from b quarks and jets originating from gluons or u, d, s or c quarks. A threshold for the discriminator value may be chosen according to the desired b-tagging efficiency and fake rate.

3.3.6. Isolation

It is often important to identify *prompt* leptons and photons, which are produced in the hard process, as opposed to non-prompt particles that are the products of in-flight decays within jets. This is accomplished by measuring the *isolation*, which is a measure of the activity around a particle. The isolation of a particle is defined

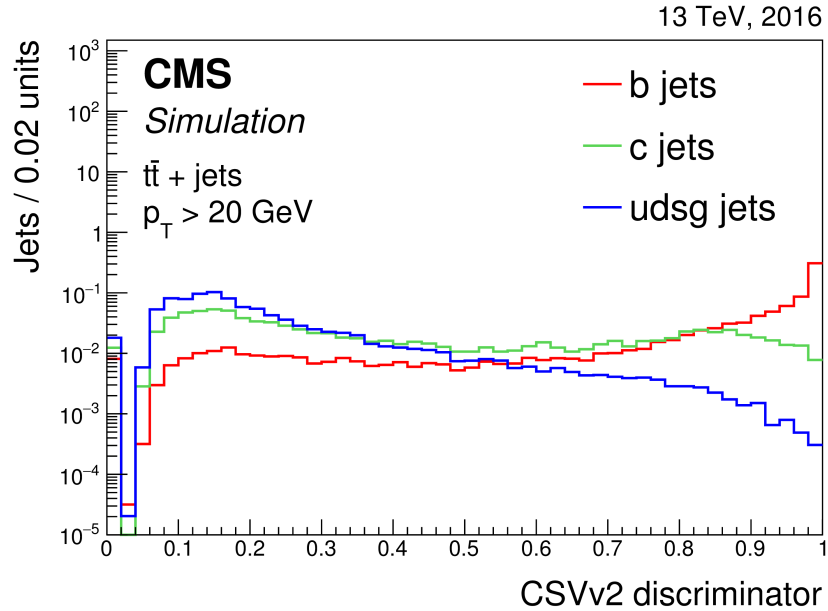


Figure 3.8.: Distribution of the discriminator value of the CSV b-tagging algorithm for jets of different flavours in simulated $t\bar{t}$ events [47]. Jets without at least two tracks are assigned a default value of -1 and are included in the first bin, which contains the underflow entries.

as the ratio of the total transverse momentum of other particles within a certain distance ΔR , and the transverse momentum of the particle itself. A particle is considered to be isolated if its isolation value is below a defined threshold.

In this search, two types of isolation are utilised, which differ in the size of the isolation cone ΔR . One is referred to as *relative isolation* I_{rel} , in which a fixed cone size of $\Delta R = 0.3$ is used. The other is *mini-isolation* I_{mini} , in which the cone size depends on the momentum of the particle, varying from $\Delta R = 0.2$ for $p_{\text{T}} < 50 \text{ GeV}$ to $\Delta R = 0.05$ for $p_{\text{T}} > 200 \text{ GeV}$. This improves the efficiency of identifying energetic leptons from the decays of highly boosted particles such as top quarks.

The total energy contained within the isolation cone (the numerator of the isolation variable) must be corrected to account for pileup, which would otherwise falsely increase the isolation value and lead to a loss in identification efficiency. This is done by ignoring charged particles that don't originate from the primary vertex, and subtracting the neutral pileup contribution, which is estimated as $\rho\Delta R$, where ρ is the average transverse energy density of all neutral particles in the event measured across the entire detector.

3.3.7. Energy sums

The production of massive supersymmetric particles results in a large transfer of energy to final state particles. In addition, weakly interacting particles such as the LSP cannot be detected directly, but their presence can be inferred by the transverse momentum imbalance of the observed particles. The total energy and missing energy in an event are therefore useful variables in characterising BSM processes.

A measure of the transverse momentum of the invisible system in an event is provided by the negative vector sum of the transverse momenta of all Particle Flow particles in the event, known as the *missing transverse momentum* or *missing transverse energy*:

$$\cancel{E}_T = - \sum_{\text{particles}} \cancel{p}_T. \quad (3.7)$$

This is calculated after the application of the jet energy corrections described in Sec. 3.3.5.

A similar quantity that is based only on the jets in the event can be defined as:

$$\cancel{H}_T = - \sum_{\text{jets}} \cancel{p}_T. \quad (3.8)$$

The scale of hadronic energy in an event is measured by the scalar sum of the jets' transverse momenta:

$$H_T = \sum_{\text{jets}} |\cancel{p}_T|. \quad (3.9)$$

3.4. Simulation

The simulation of background and signal processes is an important aspect of a search for new physics. The Monte Carlo (MC) method forms the basis of the simulation process.

The first step is the generation of the hard scattering, in which constituents of the colliding protons interact and produce the outgoing particles. This is accomplished with MC event generators such as MADGRAPH [48] and POWHEG [49]. The mo-

menta of the colliding partons are sampled from a parton distribution function (PDF). The generator also calculates, based on the Feynman diagrams of the desired process up to a certain perturbation order, the corresponding matrix elements and differential cross section. The final state particles are then generated according to the incoming parton momenta and the differential cross section.

The next step is the simulation of parton showers, that is additional QCD radiation emitted by the involved quarks and gluons, and the subsequent hadronisation in which colourless hadrons are formed according to the Lund string model. Any unstable particles in the event are then decayed. The showering, hadronisation and decay processes are performed with PYTHIA8 [50].

Additional soft interactions are overlayed in each generated event to account for pileup. The effects from up to 12 preceding and subsequent bunch crossings (out-of-time pileup) are also included.

Finally, the interactions of the resulting particles with the CMS detector (such as through ionisation and scattering) are simulated with GEANT4 [51]. The response of each subdetector, the electronics and the trigger are also emulated. The reconstruction methods described in Sec. 3.3 can then be applied as with real data.

Chapter 4.

Search strategy

This chapter describes the analysis strategy of a search for physics beyond the standard model in proton-proton collisions at a centre of mass energy of 13 TeV. The search is performed in final states containing missing transverse momentum and at least one jet.

The search is designed to have sensitivity to a wide range of new physics models that involve the production of a weakly interacting particle (WIMP), such as dark matter or the lightest supersymmetric particle. The search has been optimised for signatures in which the WIMP is produced from prompt decays at the primary collision vertex. However, as will be discussed in Chap. 5, the search is also sensitive to signatures in which the WIMP is produced at a displaced vertex following the decay of a long-lived particle.

In the proton-proton collisions, the net momentum of the colliding partons in the plane transverse to the beam direction is effectively zero (this is not necessarily the case in the longitudinal direction). In order to conserve momentum, the outgoing particles produced in the collision must therefore have an overall transverse momentum of zero. As WIMPs do not interact with the detector material, the measured net transverse momentum in the event will be non-zero. This non-zero “missing transverse momentum” is the key signature of such particles. In addition, at a hadron collider such as the LHC, the dominant production is via the strong interaction, and hence jets are readily produced either in association with the WIMP, or as initial or final state radiation (ISR, FSR). For these two reasons the search is performed in final states containing jets and missing energy. The requirement of at least one jet is needed for the missing momentum to be defined and for the event to

be triggered. A hadronic final state is ensured by vetoing events containing leptons or photons.

A missing energy signature is not unique to WIMPs, however, and is also present in certain standard model processes. Neutrinos (produced in the decays of Z and W bosons, for example) are also weakly interacting and undetectable at CMS. It is also possible for particles to be over or under-measured, thereby introducing a “fake” momentum imbalance. This type of background arising from energy mis-measurements is suppressed as much as possible (to < 1% of the total background) using dedicated variables. The remaining standard model background (that involving neutrinos) must be estimated as precisely as possible, using a combination of theory calculations, simulation, and calibrations in data. One can then look for a statistically significant excess in the data above the expected amount of standard model background that would be an indication of physics beyond the standard model.

In order to maximise the sensitivity to a wide range of BSM physics scenarios, all of which may manifest themselves in topologically slightly different ways in the detector, the candidate signal events (which form part of the *signal region*) are categorised according to four variables: the total jet energy, the missing jet energy, the number of jets, and the number of b-tagged jets. Two *control regions* are defined, labelled $\mu + \text{jets}$ and $\mu\mu + \text{jets}$, that are analogous to the signal region but are enriched by selection of muons in the W and Z background processes, respectively, and are employed in the background estimation.

Similar searches for supersymmetry have previously been performed at the LHC, at centre of mass energies of 7, 8 and 13 TeV, and for a range of integrated luminosities. These can be found in Refs. [52–56]. These searches are used as a basis for the analysis described in this thesis, which uses 35.9 fb^{-1} of data at $\sqrt{s} = 13 \text{ TeV}$. A series of developments and optimisations have been made in order to adapt the analysis for the higher centre of mass energy and larger amount of data collected. In addition, the interpretation in the context of long-lived particles is a novelty for this search.

4.1. Physics objects

This section provides the definitions of the various physics objects employed in the search. Each object is reconstructed using the algorithms described in Sec. 3.3, and each algorithm has parameters that can be tuned in order to provide a desired balance between identification efficiency and fake rate. Jets and energy sums form a key component in the search and are required in both the signal and control regions. Electrons, photons and isolated tracks are vetoed in both the signal and control regions. Muons are vetoed in the signal region and are required in the control regions. A summary of the kinematic requirements discussed in this section on these physics objects is provided in Tab. 4.1.

Object	Selection or veto	p_T (> GeV)	$ \eta (<)$
Jet	Selection (signal and control regions)	40	2.4
Muon	Selection (control region)	30	2.1
	Veto (signal region)	10	2.4
Electron	Veto (signal and control regions)	10	2.4
Photon	Veto (signal and control regions)	25	2.4
Isolated track	Veto (signal and control regions)	10	2.4

Table 4.1.: The p_T and η thresholds for physics objects that are used to either select events or veto them.

Jets

Jets are reconstructed by clustering Particle Flow particles using the anti- k_T algorithm with a distance parameter of 0.4. The four-momentum of a jet is defined to be the vector sum of the four-momenta of all clustered constituents. Corrections to the energies of the resulting jets are applied as described in Sec. 3.3.5.

Several loose requirements on the jet constituents are imposed in order to avoid spurious jets originating from noise in the calorimeters. These requirements include a minimum number of charged constituents and a minimum fraction of the jet energy attributed to charged hadrons, as well as an upper bound on neutral hadron, photon, and electron contributions. The requirements are summarised in Tab. 4.2.

Variable	Requirement	
$ \eta < 3$		
Number of constituents	> 1	
Number of charged constituents	> 0	(only for $ \eta < 2.4$)
Charged hadron energy fraction	> 0	(only for $ \eta < 2.4$)
Neutral hadron energy fraction	< 0.99	
Charged electromagnetic energy fraction	< 0.99	(only for $ \eta < 2.4$)
Neutral electromagnetic energy fraction	< 0.99	
$ \eta > 3$		
Number of neutral constituents	> 10	
Neutral electromagnetic energy fraction	< 0.90	

Table 4.2.: Quality requirements imposed on the constituents of jets.

Jets in the event are assigned a probability of having originated from a bottom quark by the b-tagging algorithm described in Sec. 3.3.5. A jet in the analysis is considered to be b-tagged if its probability is larger than 0.848. This value results in a b-tagging efficiency of $\sim 60\%$, as well as a mis-tagging rate of $\sim 10\%$ for charm quarks and $\sim 1\%$ for up, down, strange, and gluon quarks.

The jets employed in the analysis have transverse momenta and pseudorapidities satisfying $p_T > 40$ GeV and $|\eta| < 2.4$. The p_T threshold is chosen to avoid jets originating from pileup vertices.

Muons

The muons considered for event vetoing in the signal region are required to be reconstructed as either global or tracker muons. The efficiency for this is $\sim 98\%$. A mini-isolation requirement of $I_{\text{mini}} < 0.2$ is imposed that aids in identifying muons from the decays of boosted top quarks.

In the control regions, global muons are selected. Additional quality criteria are required in order to enhance the purity of prompt W and Z boson decays. These include a minimum goodness of fit of the corresponding track, and a minimum number of hits in the muon chambers – this helps to suppress fake muons resulting from *hadron punch-through*, that is high energy hadron shower remnants that penetrate the calorimeters and reach the muon chambers. A minimum number of hits

in the tracker is required to provide an accurate measurement of the momentum. The muon track is also required to be compatible with having originated from the primary vertex – this suppresses the potential background from cosmic muons and muons produced at a pileup vertex. The relative isolation quantity is required to be $I_{\text{rel}} < 0.15$.

Muons in the control regions are required to satisfy $p_T > 30 \text{ GeV}$ and $|\eta| < 2.1$, while events in the signal region are vetoed if they contain any muons with $p_T > 10 \text{ GeV}$ and $|\eta| < 2.4$.

Photons

Events containing photons are vetoed in both the signal and control regions. The isolation of a photon is measured with respect to charged hadrons, neutral hadrons, and other photons within a $\Delta\eta$ - $\Delta\phi$ cone of size 0.3. These three isolation variables are required to be below certain thresholds. An upper bound is also imposed on the ratio of the photon's energy deposited in the HCAL and the ECAL, which can be non-zero in the case of leakage of the electromagnetic shower. The shape of the shower as measured by the distribution of energy deposits in the ECAL crystals is used as a further discriminator. The photon identification efficiency following these requirements is $\sim 71\%$.

Photons in the signal region satisfying $p_T > 25 \text{ GeV}$ and $|\eta| < 2.5$ are used to veto such events.

Electrons

The electrons considered for vetoing in the signal region are identified according to requirements on the shape of the electromagnetic shower, the ratio of energy deposits in the HCAL and ECAL, the number of hits in the tracker, and the track's impact parameter. These requirements provide an identification efficiency of $\sim 90\%$, and are effective at avoiding spurious electrons (such as jets misidentified as electrons) and electrons produced from photon conversions. A mini-isolation requirement of $I_{\text{mini}} < 0.1$ is applied.

Events in the signal region are vetoed if they contain electrons with $p_T > 10 \text{ GeV}$ and $|\eta| < 2.4$.

Isolated tracks

Events containing isolated tracks are vetoed in the signal and control regions as discussed in Sec. 4.5. An isolated track is defined to be a charged PF particle that originates from the primary vertex and has a relative isolation (computed with respect to other charged particles within a cone of size $\Delta R = 0.3$) of $I_{\text{rel}} < 0.1$.

Events in the signal region are vetoed if they contain an isolated track with $p_T > 10 \text{ GeV}$ and $|\eta| < 2.4$.

Energy sums

The missing energy and jet energy sums are defined in Sec. 3.3.7. The H_T and \cancel{H}_T variables are computed using all jets in the event satisfying $p_T > 40 \text{ GeV}$ and $|\eta| < 2.4$. The missing transverse energy \cancel{E}_T is used in the definition of the M_T and $\cancel{H}_T/\cancel{E}_T$ variables as described in Secs. 4.4 and 4.5.

4.2. Baseline selection

This section describes a set of baseline selections and filters that are used to ensure a final state with significant hadronic activity and genuine missing energy that is typical of the SUSY processes being searched for. These are summarised, along with the full set of selections described in Sec. 4.5, in Tab. 4.3.

Events in the signal region containing muons or electrons are vetoed. This mainly suppresses the $W + \text{jets}$ background process in which the W boson decays semileptonically, resulting in missing energy and a lepton in the final state. In case the lepton is not identified as such but its track is reconstructed, events are vetoed if they contain an isolated track. This veto also helps to reject single prong decays of tau leptons. As a final requirement to ensure an all-jet final state, events containing photons are also vetoed.

At least one jet in the event is required to have a transverse momentum $p_T > 100 \text{ GeV}$. The jet energy sums must satisfy $H_T > 200 \text{ GeV}$ and $\cancel{H}_T > 200$. These two thresholds are chosen to be as low as possible in order to maximise the acceptance of the search across a wide range of the SUSY mass parameter space, while simultaneously maintaining a reasonable trigger rate and efficiency. The trigger strategy will be discussed further in Sec. 4.7.

At least one good quality vertex is required to be reconstructed in the event. This is defined by a vertex with a minimum number of associated tracks and with tracks that have a high probability of belonging to that vertex. The vertex is also required to be within a longitudinal and radial distance from the centre of the detector of 24 cm and 2 cm, respectively.

Missing energy is not only caused by undetectable or misreconstructed particles produced in the proton-proton collisions. Spurious \cancel{E}_T can also be induced by effects related to detector malfunctions and beam dynamics. These effects include spurious energy in the HCAL due to electronics noise and particle interactions with the instrumentation, missed energy in the ECAL due to dead cells, anomalous high amplitude pulses in certain ECAL endcap supercrystals, and beam halo particles. Beam halo refers to the showers of particles, including pions, neutrons and muons, that are produced when beam protons collide with residual gas particles in the LHC vacuum chambers or with the beam collimators. These beam halo particles can deposit energy in the calorimeters and CSCs of the muon system along lines parallel to the beam direction. Events affected by these spurious \cancel{E}_T sources are identified and vetoed using dedicated algorithms as described in Ref. [57]. These algorithms take advantage of various features related to geometrical patterns, pulse shapes and timing information. The impact of these filters on signal acceptance is negligible.

The beam halo filter, however, only targets halo muons, and is ineffective against calorimeter deposits from halo hadrons. These types of events are straightforwardly recognised, as shown in Fig. 4.1. The highest p_T jet in the event usually appears at ϕ values of 0 and π as this corresponds to the plane of the LHC ring in which the proton beams are steered, and will have a contribution from charged hadrons close to zero because of the lack of tracker hits. To suppress these beam halo events, events are rejected if the leading jet has a charged hadron energy fraction $f_{\text{CH}} < 0.1$.

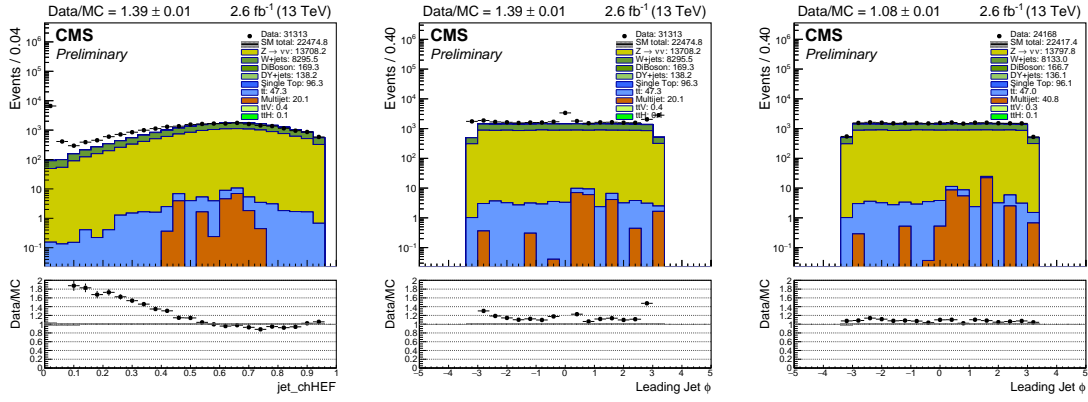


Figure 4.1.: The leading jet’s charged hadron energy fraction (left) and ϕ direction before (centre) and after (right) applying a requirement of $f_{\text{CH}} > 0.1$. The large excess in data at f_{CH} values close to zero and $\phi = 0$ and π is consistent with beam halo effects, and is effectively suppressed by the f_{CH} requirement.

As a further safeguard against noise and misreconstruction issues, events that contain a jet that fails the identification requirements outlined in Sec. 4.1 are not considered.

Finally within the set of baseline selections, events are vetoed if there are any jets with a pseudorapidity of $|\eta| > 2.4$. This threshold corresponds to the extent of the tracker and hence ensures well reconstructed jets and a better resolution of the energy sums. This requirement also has the added benefit of rejecting a larger proportion of background, particularly QCD processes, compared to signal processes, which tend to have more central jets.

4.3. Standard model backgrounds

The baseline selections described in the previous section select events with significant hadronic activity and missing energy, as desired. However, a large number of standard model events still remain. These include processes (labelled electroweak background processes) with ‘genuine’ missing energy in the final state due to neutrinos, as well as QCD multijet processes with ‘fake’ missing energy in the final state due to jet energy mismeasurements.

4.3.1. Electroweak processes

The dominant electroweak background process (comprising $\sim 50\%$ of the signal region background events) is the production of a Z boson in association with jets, with the Z boson decaying to two neutrinos. This background is irreducible as the final state consists of only jets and missing energy, just like the SUSY processes being searched for.

The second largest background process (making up $\sim 40\%$ of the total background) is the production of a W boson in association with jets, with the W boson decaying semi-leptonically to a lepton and a neutrino. Such an event may not be vetoed if the lepton is not reconstructed or travels in a direction that is outside the acceptance of the detector, or is a muon or electron that fails the kinematic, identification, or isolation criteria listed in Sec. 4.1. If the lepton is a tau, it may decay semi-leptonically to a muon or electron that is not vetoed for the aforementioned reasons, or it may decay hadronically resulting in a jets plus E_T final state. In the case of a single-prong hadronic decay, the tau background is suppressed with a veto on events containing an isolated track, as mentioned in Sec. 4.2. The veto on isolated tracks cannot capture three-prong decays, however, as the tracks are usually not isolated and are instead reconstructed as a jet.

The third largest background process (constituting $\sim 5\%$ of the signal region background) is the production of top quark-antiquark pairs ($t\bar{t} + \text{jets}$). This background is characterised by b-jets and a larger number of jets in the final state compared to the other two dominant backgrounds. Each top quark decays to a bottom quark and W boson, and each W boson can decay hadronically or semi-leptonically. The dominant decay mode in the signal region is the one in which one of the W bosons decays hadronically and the other decays semi-leptonically, resulting in a lepton that is then ‘lost’ in the same way as for the $W(\rightarrow \ell\nu) + \text{jets}$ background described previously. The decay mode in which both W bosons decay hadronically is negligible because there is no significant amount of missing energy in the final state. The decay mode in which both W bosons decay semi-leptonically is also negligible because of the low probability of losing both leptons.

Additional, residual standard model background processes include the production of a single top quark (in association with a b quark, light quark, or W boson), the production of vector boson pairs (WW, WZ, ZZ), $t\bar{t}$ production in association with a vector boson, $Z(\rightarrow \ell\ell) + \text{jets}$ production, and $\gamma + \text{jets}$ production.

4.3.2. QCD processes

At a hadron collider such as the LHC, the most abundant process is that of QCD multijet production, having a cross section that is several orders of magnitude larger than other standard model processes. The final state consists of two or more jets, and there is no intrinsic missing energy (except in the case of heavy flavour QCD, as discussed below). However, issues with the detector or inaccuracies in the reconstruction can cause the event to appear unbalanced in transverse momentum, thereby introducing fake E_T . Although these effects are not very common, when coupled with the large QCD production cross section, the result is that QCD multijet production remains as the largest background even when requiring a reasonable amount of E_T such as 200 GeV. The following is a comprehensive list of the various mechanisms by which QCD processes can have a large amount of missing energy. The next section will describe a set of variables that are used to identify and suppress this type of background.

- Soft jets with transverse momentum $p_T < 40$ GeV are not included in the computation of the jet energy sums, and therefore result in an apparently unbalanced event. The resulting missing jet energy is particularly significant when there are several jets below the p_T threshold. A similar problem can occur when the jets are outside the acceptance of the detector.
- Significant over or under-measurements of jets' energies due to the tails of the resolution distribution. This includes the mismeasurement of a single jet in the event, in which case the missing transverse momentum vector is collinear (if the jet's energy is under-measured; or anti-collinear if it is over-measured) to the jet's direction, as well as the mismeasurement of two or more jets, in which case the missing momentum is not aligned with any jet. A third effect is when a jet is severely under-measured such that its measured transverse momentum is below the 40 GeV threshold.
- Detector effects, such as dead cells and hot cells in the calorimeters, can result in a large amount of fake missing energy. These effects are dealt with by the dedicated E_T filters described in Sec. 4.2.
- The production of bottom quarks with a subsequent semi-leptonic decay leads to genuine missing energy in the final state due to the resulting neutrino. The lepton and neutrino are typically contained within the jet cone. This means

that the lepton is not isolated and so such events are not rejected by the lepton veto. It also means that the missing transverse momentum vector is roughly collinear with the jet.

The dominant mechanism by which QCD processes can pass the baseline selections is that due to jet energy mismeasurements ($\sim 70\%$), followed by jets below threshold ($\sim 30\%$). The heavy flavour and detector effects are comparatively much smaller ($\sim 1\%$).

4.4. QCD background rejection

It is important to suppress the overwhelming QCD background so that it does not swamp any potential signal. This section describes three key variables (α_T , $\Delta\phi_{\min}^*$, and H_T/E_T) that effectively distinguish QCD events from events with genuine missing energy. Each variable exploits certain topological or kinematical features, and each one targets different sources of missing energy of those described in the previous section.

Events in the signal region need to satisfy certain requirements on these variables, as will be outlined in Sec. 4.5. These thresholds are chosen such that the QCD background forms no more than $\sim 1\%$ of the total standard model background in the signal region. This choice is motivated by the difficulty in estimating this type of background accurately and precisely. The difficulty arises from the lack of precise high-order theoretical calculations on the production cross section and kinematic properties. In addition, because of the large cross section and computing limitations, the number of simulated events is much smaller than that expected by the integrated luminosity of 35.9 fb^{-1} , and so the simulated events have large weights and hence large statistical uncertainties. Therefore, if QCD processes were to form a large part of the total expected background this would significantly reduce the sensitivity of the search. A small contribution of $\sim 1\%$, even with a large uncertainty, has a negligible impact on the sensitivity.

4.4.1. The α_T variable

The α_T variable is designed to discriminate between balanced events that may contain mismeasurements and unbalanced events containing invisible particles [58]. For a dijet event it is defined as:

$$\alpha_T = \frac{E_T^{j_2}}{M_T}, \quad (4.1)$$

where $E_T^{j_2}$ is the transverse energy of the least energetic jet, and M_T is the transverse mass of the dijet system, which is given in general for a number of jets by:

$$M_T = \sqrt{\left(\sum_i E_T^{j_i}\right)^2 - \left|\sum_i \mathbf{p}_T^{j_i}\right|^2}, \quad (4.2)$$

where $E_T^{j_i}$ is the transverse energy of the i^{th} most energetic jet, and $\mathbf{p}_T^{j_i} = (p_x^{j_i}, p_y^{j_i})$ is its transverse momentum vector, $p_x^{j_i}$ and $p_y^{j_i}$ being the x and y components, respectively.

To illustrate how the α_T variable works, one can assume the mass of the jets to be much smaller than their momenta (so that $E_T \approx p_T$, which is a good approximation for jets produced at the LHC), and rewrite M_T in terms of the azimuthal angle $\Delta\phi(j_1, j_2)$ between the two jets such that:

$$\alpha_T \approx \frac{E_T^{j_2}}{\sqrt{2E_T^{j_1}E_T^{j_2}(1 - \cos\Delta\phi(j_1, j_2))}}. \quad (4.3)$$

If the jets have equal and opposite transverse momenta such as in a QCD dijet event, then the azimuthal angle between them is π , their transverse energies are the same, and the value of α_T is exactly 0.5. If one of the jets' energies is mismeasured, then $E_T^{j_2} < E_T^{j_1}$ and α_T takes values less than 0.5. In an event where the jets are recoiling against a system of invisible particles, the angle between them is smaller than π and the value of α_T is generally larger than 0.5.

For events with more than two jets in the final state, the jets can be grouped into two *pseudo jets* such that the difference in transverse energy ΔE_T between the two pseudo jets is minimised, where the transverse energy of a pseudo jet is computed via the vector sum of the transverse energies of the constituent jets. This is done so

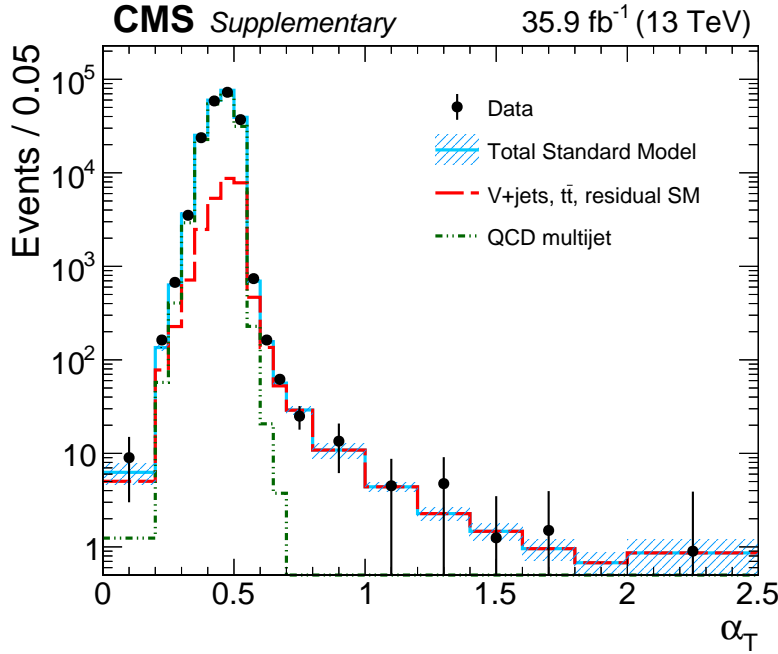


Figure 4.2.: The distribution of the α_T variable in data and simulation for events satisfying the signal region selections (Sec. 4.5) except the α_T requirement, plus the additional requirements $n_{\text{jet}} \geq 2$, $p_T^{j_2} > 100$ GeV, and $H_T > 900$ GeV. The ability of the variable to effectively discriminate between QCD processes and processes with genuine missing energy is evidenced by the sharp edge at 0.5.

that the resulting pseudo dijet system is as close to a balanced event as possible. Since $\Delta E_T = E_T^{j_1} - E_T^{j_2}$ and $|\sum_i \mathbf{p}_T^{j_i}| = H_T$, the general form of the α_T variable can be defined as:

$$\alpha_T = \frac{\sum_i E_T^{j_i} - \Delta E_T}{2\sqrt{(\sum_i E_T^{j_i})^2 - H_T^2}}. \quad (4.4)$$

For balanced QCD events with no missing energy, $\Delta E_T = H_T = 0$ and $\alpha_T = 0.5$. If a jet in such an event is mismeasured, then $\Delta E_T \approx H_T$ and $\alpha_T < 0.5$. For events with genuine missing energy, $H_T > 0$ and $\Delta E_T = 0$, resulting in $\alpha_T > 0.5$.

The discriminating power of the α_T variable is shown in Fig. 4.2. Multijet QCD events are the dominant process in the region of $\alpha_T \leq 0.5$, while processes with genuine missing energy occupy the region of $\alpha_T > 0.5$. It is possible for QCD events to have values of α_T slightly larger than 0.5 if there is a severe mismeasurement or there are several jets below the p_T threshold.

4.4.2. The $\Delta\phi_{\min}^*$ variable

The $\Delta\phi_{\min}^*$ variable also provides powerful discrimination between events with fake missing energy and events with genuine missing energy. First it is instructive to consider the $\Delta\phi_{\min}$ variable, which is the minimum (over all jets in the event above the p_T threshold) azimuthal angle between a jet and the missing transverse jet energy vector:

$$\Delta\phi_{\min} = \min \Delta\phi \left(\mathbf{p}_T^{j_i}, \mathbf{H}_T \right). \quad (4.5)$$

If a jet's energy in the final state is under-measured, the missing energy vector is collinear with the jet direction, and so $\Delta\phi_{\min}$ is zero, whereas for processes in which the jets are recoiling against genuine missing energy, the value of $\Delta\phi_{\min}$ is non-zero.

However, if a jet's energy is over-measured, the missing energy vector points in the opposite direction to the jet and so $\Delta\phi_{\min}$ is not necessarily zero. This limitation can be overcome by comparing the jet's direction with the missing energy vector that does not consider the jet in the vector sum, $\mathbf{H}_T^{j_i} = \mathbf{H}_T + \mathbf{p}_T^{j_i}$. This is the definition of the $\Delta\phi_{\min}^*$ variable:

$$\Delta\phi_{\min}^* = \min \Delta\phi \left(\mathbf{p}_T^{j_i}, \mathbf{H}_T^{j_i} \right). \quad (4.6)$$

The discriminating power of the $\Delta\phi_{\min}^*$ variable is shown in Fig. 4.3. Multijet QCD events have values of $\Delta\phi_{\min}^*$ close to 0, with the distribution falling sharply beyond this, whereas processes containing genuine missing energy exhibit a longer tail up to values of π radians.

The $\Delta\phi_{\min}^*$ variable is effective at capturing QCD events that contain a single mismeasurement or a neutrino produced by a heavy quark decay that is collinear with a jet. It is less effective if a jet is severely mismeasured such that its p_T is below threshold, or if there are two or more mismeasured jets. Both of these cases result in missing momentum vector that is not necessarily collinear with any jet.

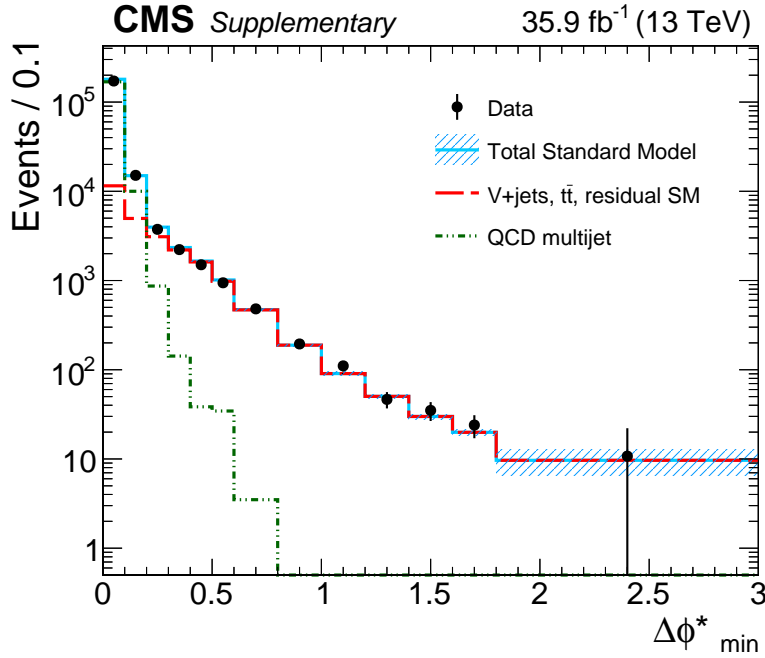


Figure 4.3.: The distribution of the $\Delta\phi_{\min}^*$ variable in data and simulation for events satisfying the signal region selections (Sec. 4.5) except the $\Delta\phi_{\min}^*$ requirement, plus the additional requirements $n_{\text{jet}} \geq 2$, $p_T^{j_2} > 100$ GeV, and $H_T > 900$ GeV. The ability of the variable to effectively discriminate between QCD processes and processes with genuine missing energy is evidenced by the cluster of QCD events close to 0, while processes with genuine E_T take on larger values up to π radians.

4.4.3. The H_T/E_T variable

As mentioned previously, the α_T and $\Delta\phi_{\min}^*$ variables are not as effective at identifying QCD events in which there are several jets with transverse momentum below the 40 GeV threshold. In such events, the value of H_T is biased to larger values. The E_T variable, however, is computed using all PF objects in the event satisfying a much lower threshold (10 GeV for jets) and so is less susceptible to this bias and remains closer to zero. One can compare the values of H_T and E_T to identify these events – the ratio of H_T/E_T tends to be significantly larger than 1 for such events.

For processes with genuine missing energy, on the other hand, the ratio generally remains close to unity as the increase in missing energy due to threshold effects is proportionally smaller with respect to the true missing energy which is already relatively large. The distribution of the H_T/E_T ratio is shown in Fig. 4.4 and

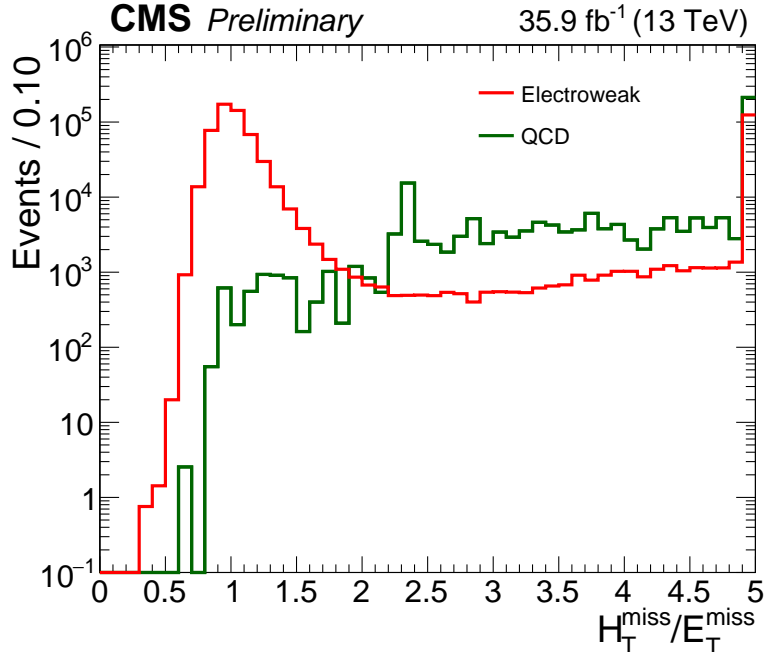


Figure 4.4.: The distribution of the H_T^{miss}/E_T ratio in simulation for events satisfying the signal region selections (Sec. 4.5) except the H_T^{miss}/E_T requirement. The ability of the variable to effectively discriminate between QCD processes and processes with genuine missing energy is evidenced by the population of QCD events above 1.25, while processes with genuine E_T have values more consistent with unity.

demonstrates the difference between the two types of backgrounds. Multijet QCD processes tend to populate the region of $H_T^{\text{miss}}/E_T > 1.25$.

4.5. Event selection

After the baseline selections outlined in Sec. 4.2, additional selections are applied in order to suppress the QCD background in the signal region and enrich the control regions in the relevant standard model processes that need to be estimated. These are described in this section and are summarised, along with the baseline selections described in Sec. 4.2, in Tab. 4.3.

Baseline selection	
All-jet final state	At least one jet; no muons, electrons, photons or isolated tracks
\cancel{E}_T quality	No spurious \cancel{E}_T due to instrumental effects or beam halo
Jet energy and sums	$p_T^{j_1} > 100 \text{ GeV}$, $H_T > 200 \text{ GeV}$, $\cancel{H}_T > 200 \text{ GeV}$
Jets outside acceptance	$\cancel{H}_T/\cancel{E}_T < 1.25$; no jets with $ \eta > 2.4$
Jet quality	No jets that fail identification criteria
Signal region	Baseline selection +
$\alpha_T (>) (H_T \text{ GeV range})$	0.65 (200-250), 0.60 (250-300), 0.55 (300-350), 0.53 (350-400), 0.52 (400-900)
$\Delta\phi_{\min}^*$	$\Delta\phi_{\min}^* > 0.5$
Control regions	Baseline selection +
$\mu + \text{jets}$	One muon; $\min \Delta R(\mu, j_i) > 0.5$; $30 < M_T(\mu, \cancel{E}_T) < 125 \text{ GeV}$
$\mu\mu + \text{jets}$	Two muons opp. charge; $\min \Delta R(\mu_{1,2}, j_i) > 0.5$; $ M(\mu_1, \mu_2) - m_Z < 25 \text{ GeV}$
Hadronic	Signal region sidebands $1.25 < \cancel{H}_T/\cancel{E}_T < 3.0$ and/or $0.2 < \Delta\phi_{\min}^* < 0.5$

Table 4.3.: Summary of selections as part of the definition of the signal and control regions.

4.5.1. Signal region

The baseline selections in the signal region are chosen to ensure a hadronic final state with significant energy and missing momentum that is characteristic of supersymmetry models. As a reminder, these include minimum requirements on H_T and \cancel{H}_T , and event vetoes on non-hadronic objects and forward jets as well as spurious \cancel{E}_T sources. However, a large number of QCD events remain that contain fake missing energy (or missing energy from heavy quark decays). This background is suppressed to a very small level ($\lesssim 1\%$ of the total standard model background) by imposing certain requirements on the QCD-discriminating variables α_T , $\Delta\phi_{\min}^*$, and $\cancel{H}_T/\cancel{E}_T$ described in the previous section.

An H_T -dependent α_T requirement is used for multijet events, as summarised in Tab. 4.4. For events containing only one jet above 40 GeV, α_T is undefined and no requirement is imposed. The α_T threshold is as high as 0.65 for events with $200 < H_T < 250 \text{ GeV}$, and is reduced with increasing H_T down to 0.52 for events with $400 < H_T < 900 \text{ GeV}$, while no requirement at all is made for $H_T > 900 \text{ GeV}$. The thresholds are a decreasing function of H_T because the expected number of QCD events falls quickly with increasing H_T . The thresholds are also chosen to ensure that events are triggered with full efficiency, as the α_T trigger thresholds

have been chosen to provide a reasonable trigger rate. The trigger strategy will be discussed in Sec. 4.7.

H_T (GeV)	200-250	250-300	300-350	350-400	400-900	>900
α_T requirement (>)	0.65	0.60	0.55	0.53	0.52	0

Table 4.4.: The α_T thresholds as a function of H_T for events containing at least two jets. No requirement is made on events containing only one jet.

Any QCD background events not captured by the α_T selection, in particular events with $H_T > 900$ GeV or with only one jet for which there is no α_T requirement, are suppressed by a requirement on $\Delta\phi_{\min}^*$. The threshold is chosen to be $\Delta\phi_{\min}^* > 0.5$ radians for all events, regardless of H_T and the number of jets. For monojet events, $\Delta\phi_{\min}^*$ is undefined when using only jets with $p_T > 40$ GeV, and is instead computed using jets that satisfy a lower threshold of $p_T > 25$ GeV. If there are no jets with $25 < p_T < 40$ GeV, $\Delta\phi_{\min}^*$ remains undefined and no requirement is made on monojet events. The α_T variable could also be defined similarly using jets of lower p_T , but QCD events are produced with at least two jets, so QCD monojet events (which must result from a severe mismeasurement) form a relatively smaller background and these are effectively suppressed by the $\Delta\phi_{\min}^*$ requirement alone.

Finally, in order to suppress the fake E_T QCD background due to several jets with a transverse momentum below the 40 GeV threshold, a requirement is made on the H_T/E_T ratio of $H_T/E_T < 1.25$.

4.5.2. Control regions

Each control region is used to estimate a particular standard model background process. The estimation methods will be discussed in Secs. 4.10 and 4.11. The selections in the control regions are chosen so that they are enriched in the background processes that each is designed to estimate, while remaining kinematically as similar as possible to the signal region. For this reason, the selections are the same as in the signal region except for the inversion of certain requirements and additional purity criteria, as described in the following subsections.

In the case of the two muon control regions, the muons are not included in the computation of E_T (and similarly all jet-based variables) in order to mimic the

missing energy due to the neutrinos or lost lepton. The control regions are also orthogonal to the signal region (an event cannot occupy both regions, by construction) and are expected to contain very little signal. In any case, any potential signal contamination in the control regions is accounted for in the statistical model (Sec. 5.3).

$\mu + \text{jets}$ control region

The $\mu + \text{jets}$ control region is used to estimate the $W(\rightarrow \ell\nu) + \text{jets}$ and $t\bar{t}$ backgrounds (plus the residual backgrounds). The selections are chosen to identify W bosons, originating from such processes, decaying to a muon and a neutrino.

The muon veto of the signal region is inverted and instead exactly one muon (as defined in Sec. 4.1) is required. The muon is required to be separated from the closest jet by $\Delta R(\mu, \text{jet}) > 0.5$ in order to select isolated muons from prompt W decays rather than from QCD decays.

To improve the purity in W bosons, the transverse mass of the muon and missing transverse energy (which is a proxy for the neutrino) is required to be compatible with the W mass with $30 < M_T(\mu, E_T) < 125$ GeV. The transverse mass must be used rather than the invariant mass as the z-component of the missing momentum is unknown.

All of these criteria are effective at selecting a pure sample of $W(\rightarrow \ell\nu) + \text{jets}$ and $t\bar{t}$ events with minimal QCD contamination, and hence no requirements on α_T or $\Delta\phi_{\min}^*$ are made in this control region. This has the benefit of significantly increasing the number of events in the control region, which decreases the statistical uncertainties associated with the corresponding background estimations. Any potential issues in the background estimation arising from different α_T and $\Delta\phi_{\min}^*$ selections are accounted for as a systematic uncertainty (see Sec. 4.12.2).

$\mu\mu + \text{jets}$ control region

The $\mu\mu + \text{jets}$ control region is used to estimate the main irreducible $Z(\rightarrow \nu\nu) + \text{jets}$ background. The selections are chosen to identify Z bosons decaying to two muons. The muon veto of the signal region is again inverted and instead exactly two muons, of opposite charge, are required. Each muon is required to be separated in ΔR

from jets by the same amount as in the $\mu + \text{jets}$ control region. In order to improve the purity in Z bosons, the invariant mass of the dimuon system is required to be compatible with the mass of the Z boson, with $|M(\mu_1, \mu_2) - m_Z| < 25 \text{ GeV}$. Similarly to the $\mu + \text{jets}$ control region, no requirements on α_T and $\Delta\phi_{\min}^*$ are needed.

Hadronic control regions

Three hadronic control regions are used in the estimation of the small QCD background remaining after the full set of selections have been applied. These control regions consist of the exact same selections as the signal region, except that the $\Delta\phi_{\min}^*$ and \cancel{H}_T / E_T requirements are inverted, both individually and in conjunction, providing three control regions or “sidebands” that are enriched in QCD processes. The sidebands are capped such that $0.2 < \Delta\phi_{\min}^* < 0.5 \text{ rad}$ and $1.25 < \cancel{H}_T / E_T < 3.0$. Table 4.5 shows a summary of the selections that define these sidebands.

Table 4.5.: The definitions of the sideband regions employed in the estimation of the QCD background.

	$0.2 < \Delta\phi_{\min}^* < 0.5$	$\Delta\phi_{\min}^* > 0.5$
$1.25 < \cancel{H}_T / E_T < 3.0$	$\cancel{H}_T / E_T - \Delta\phi_{\min}^*$ sideband	\cancel{H}_T / E_T sideband
$\cancel{H}_T / E_T < 1.25$	$\Delta\phi_{\min}^*$ sideband	Signal region

4.6. Event categorisation

Events are categorised, or binned, according to four variables. This is done to improve the discrimination between signal and background processes, which tend to populate different regions of this four-parameter space. Moreover, different SUSY processes occupy different regions depending on the particular production mode and final state considered. The four variables are the number of jets n_{jet} , the number of b-tagged jets n_b , the total jet energy H_T , and the missing transverse jet energy \cancel{H}_T . The binning scheme and motivation for each discriminating variable are described in this section.

The control regions are binned identically to the signal region, with some exceptions in the \mathcal{H}_T and n_b dimensions that will be explained in this section. This is done to ensure that the backgrounds are estimated (as described in Sec. 4.10) using events in the control regions of similar kinematic and topological properties. Any estimations that are not made between equivalent bins, or are made directly according to simulation, are assigned an additional systematic uncertainty.

A summary of the bins used in the signal region is provided in Tab. 4.6. In total there are 574 bins, with 254 in the signal region, 198 in the $\mu + \text{jets}$ control region, and 122 in the $\mu\mu + \text{jets}$ control region.

The hadronic control regions are categorised slightly differently, with coarser bins. These regions do not form part of the overall statistical model used to derive limits or significances, and instead are used to estimate the QCD background separately. This will be discussed in Sec. 4.11.

Categorisation by n_{jet}

First, it is convenient to define the topology of a final state in terms of the momenta of the two most energetic jets. As mentioned in Sec. 4.2, the leading jet is required to have a transverse momentum larger than 100 GeV. If the sub-leading jet also has $p_T > 100$ GeV, the event is categorised as *symmetric*. If it has $40 < p_T < 100$ GeV, the event is labelled *asymmetric*. If it has $p_T < 40$ GeV or if there are no additional jets in the final state, it is categorised as a *monojet* event.

The symmetric category captures many of the SUSY production scenarios in which the mass difference with respect to the LSP is large and the final state contains several highly energetic jets. In the case of a small mass difference, little kinetic energy is available for the decay products and so the acceptance for these models, which relies more on jets from ISR, is provided by the asymmetric and monojet categories. These categories are also useful at capturing models of long-lived supersymmetry in which the decays occur outside of the detector, as the identification of these events relies on the initial state radiation.

Events are categorised according to the number of jets in the final state and the jet topology. The seven categories employed are $n_{\text{jet}} = 1, \geq 2a, 3, 4, 5, \geq 6$, where the a denotes an asymmetric topology.

n_{jet}	n_b	H_T (GeV)				
		200-250, 250-300, 300-350, 350-400	400-500, 500-600	600-750, 750-900	900-1050, 1050-1200	>1200
1	0	200	200	200	200	–
	1	200	200	200	–	–
$\geq 2a$	0	200	200,400	200,400,600	200,900	–
	1	200	200,400	200,400,600	200,900	–
	2	200	200,400	200,400,600	200,900	–
	≥ 3	200	200,400	200,400,600	–	–
2	0	200	200,400	200,400,600	200,400,600,900	200,400,600,900
	1	200	200,400	200,400,600	200,400,600,900	200,400,600,900
	2	200	200,400	200,400,600	–	–
3	0	200	200,400	200,400,600	200,400,600,900	200,400,600,900
	1	200	200,400	200,400,600	200,400,600,900	200,400,600,900
	2	200	200,400	200,400,600	200,400,600,900	200,400,600,900
	3	200	200,400	200,400,600	–	–
4	0	–	200,400	200,400,600	200,400,600,900	200,400,600,900
	1	–	200,400	200,400,600	200,400,600,900	200,400,600,900
	2	–	200,400	200,400,600	200,400,600,900	200,400,600,900
	≥ 3	–	200,400	200,400,600	200,400,600,900	–
5	0	–	200,400	200,400,600	200,400,600	200,400,600,900
	1	–	200,400	200,400,600	200,400,600	200,400,600,900
	2	–	200,400	200,400,600	200,400,600	200,400,600,900
	3	–	200,400	200,400,600	200,400,600	–
	≥ 4	–	200,400	–	–	–
≥ 6	0	–	200	200,400	200,400,600	200,400,600,900
	1	–	200	200,400	200,400,600	200,400,600,900
	2	–	200	200,400	200,400,600	200,400,600,900
	3	–	200	200,400	200,400,600	200,400,600,900
	≥ 4	–	200	–	–	–

Table 4.6.: Summary of all bins in the signal region. The listed numbers correspond to the lower boundaries of the H_T bins in each $(n_{\text{jet}}, n_b, H_T)$ bin; the final number in the list is always an open bin. A single-element list is equivalent to no binning in H_T . A dash means a particular $(n_{\text{jet}}, n_b, H_T)$ bin is not used, and so the previous H_T bin (if applicable) is an open bin. The muon control regions are binned identically, except that they are not binned in H_T , and the largest n_b category in the $\mu\mu + \text{jets}$ control region is ≥ 1 .

Categorisation by H_T

The H_T variable provides a measure of the mass scale of a BSM physics process and the corresponding hadronic activity in the event. Events are categorised by H_T as follows: four bins of width 50 GeV in the range 200-400 GeV, two bins of

width 100 GeV in the range 400-600 GeV, four bins of width 150 GeV in the range 600-1200 GeV, and a final open bin $H_T > 1200$ GeV. To maintain a manageable number of bins, these 11 bins are aggregated in the signal region to just five: 200-400, 400-600, 600-900, 900-1200, and ≥ 1200 GeV.

The exact H_T binning scheme depends on n_{jet} and is included in Tab. 4.6. Because of the $p_T > 40$ GeV threshold on jets, certain low H_T bins at high n_{jet} are kinematically restricted or non-physical and are therefore not considered. High H_T bins at high n_{jet} can be statistically limited and are merged from above so that the corresponding bin in the control region is well populated and the statistical uncertainty on the estimated background is not too large.

Categorisation by n_b

The number of b-tagged jets is an effective discriminator for SUSY models that involve the production of heavy quarks. The standard model background containing b-tagged jets is relatively smaller, and mainly comes from $t\bar{t}$ production, as well as some contribution from $W + \text{jets}$ and $Z + \text{jets}$ in which a jet is mistagged. Additional sensitivity is also found for long-lived particles with lifetimes similar to that of b quarks, as their hadronic decay products can be reconstructed as b-tagged jets.

Events are categorised according to $n_b = 0, 1, 2, 3, \geq 4$. Again, the exact binning scheme depends on n_{jet} and is included in Tab. 4.6. The largest n_b bin can be at most equal to n_{jet} . Bins are also merged from above according to the number of data counts in the $\mu + \text{jets}$ control region to ensure that the background estimations do not suffer from large statistical uncertainties. As the $\mu\mu + \text{jets}$ control region is somewhat statistically limited, especially at high n_b , the largest n_b bin employed in this control region is $n_b \geq 1$.

Categorisation by H_T

The signal region is additionally categorised according to H_T . This helps to further separate the background and signal, as signal processes tend to have values of H_T closer to H_T .

Events are categorised in \mathcal{H}_T using up to four bins, that are aligned with the boundaries of the H_T bins: 200-400, 400-600, 600-900, ≥ 1200 GeV. In this case, the value of \mathcal{H}_T (which is a vector sum) is bounded above by H_T (which is a scalar sum) by construction. Bins are again merged from above to ensure each bin is well populated by simulated events. For events with $n_{\text{jet}} = 1$, for which $\mathcal{H}_T = H_T$, or with $200 < H_T < 400$ GeV, no binning in \mathcal{H}_T is employed.

Unlike with the n_{jet} , n_b and H_T variables, events in the control regions are not binned in the \mathcal{H}_T dimension. The background estimations in each \mathcal{H}_T bin are taken directly from simulation instead of being derived from the control regions. This is done to avoid binning the control regions too finely, which would greatly reduce their statistical power. A validation of this method will be discussed in Sec. 4.10.2.

4.7. Trigger

As discussed previously, the aim of the search is to be as inclusive as possible to a wide range of new physics processes by having low thresholds on the amount of hadronic activity and missing energy. This is particularly important for models with a compressed mass spectrum, as well as models with long-lived particles, as these contain relatively fewer and/or softer jets in the final state. The acceptance of the search towards these BSM physics processes is therefore largely dependent on the ability of the trigger to effectively select such events.

The HL trigger thresholds are optimised to provide a maximal acceptance subject to constraints on the readout rate and the processing time. As there is often an overlap between events selected by different triggers, and the same physics objects are used by various triggers, the quantities of importance for a particular trigger are the *effective* or *exclusive* rate and processing time. These are, respectively, the rate and processing time added by that trigger to the overall HLT menu. The total available rate and processing time of the HLT are ≈ 1 kHz and ≈ 200 ms, respectively, while individual triggers are typically constrained to have an effective rate and processing time of at most a few Hz and a few milliseconds.

The triggers for this search make use of QCD-discriminating variables such as α_T to control the readout rate, and the thresholds are essentially chosen to be as low as possible while satisfying the rate constraint and ensuring a good selection efficiency

for events in the signal region. The triggers make use of Particle Flow reconstruction, which is a computationally intensive task as it involves the combination of information from various sub-detectors. A prefilter is utilised to help satisfy the timing constraint, whereby loose requirements are first made using simpler objects, such as jets reconstructed using only the calorimeters, before proceeding with the PF reconstruction and final trigger selections.

In order to reduce the readout rate, triggers may be assigned a *prescale factor* f_{ps} , which is defined such that the probability that an event which satisfies the trigger requirements is read out is $1/f_{\text{ps}}$. This means that a trigger with, say, $f_{\text{ps}} = 10$ only records approximately one in every ten events that satisfy its requirements.

Several versions of the same trigger are usually included in the HLT menu, each with slightly different thresholds that are suited for different LHC running conditions. As the instantaneous luminosity of the LHC is increased throughout the year, the lower threshold versions become prescaled or disabled. Similarly, the lower thresholds become unprescaled as the luminosity falls throughout an LHC fill. To avoid large statistical uncertainties, only events collected by unprescaled triggers are considered in the search.

4.7.1. Signal and control region triggers

Various triggers are utilised to collect data in the signal and control regions. These are described in the following and summarised in Tab. 4.7, which shows the thresholds employed by each trigger and the amount of data collected by each one. All HL triggers employ Particle Flow reconstruction.

Three groups or families of triggers, which will be described in this section, are used to collect events in the signal region and hadronic control regions. An event that satisfies any of these triggers is selected.

The first group consists of five triggers with requirements on both H_T and α_T . These are designed to map onto the the selections employed in the analysis (described in Sec. 4.5). Their thresholds on (H_T, α_T) are $(200, 0.57)$, $(250, 0.55)$, $(300, 0.53)$, $(350, 0.52)$, $(400, 0.51)$. This set of triggers collected data for approximately the first half of the 2016 run, and were substituted by slightly higher α_T thresholds in the second half when the instantaneous luminosity reached $10^{34} \text{ cm}^{-2} \text{ s}^{-1}$. These triggers

HLT requirements	L1 seed requirements	HLT unprescaled fraction
$H_T > 200 \wedge \alpha_T > (0.57, 0.63)$	$H_T > (240, 300) \vee E_T > (60, 100)$	(0.53, 0.47)
$H_T > 250 \wedge \alpha_T > (0.55, 0.58)$	$H_T > (240, 300) \vee E_T > (60, 100)$	(0.53, 0.47)
$H_T > 300 \wedge \alpha_T > (0.53, 0.54)$	$H_T > (240, 300) \vee E_T > (60, 100)$	(0.53, 0.47)
$H_T > 350 \wedge \alpha_T > (0.52, 0.53)$	$H_T > (240, 300) \vee E_T > (60, 100)$	(0.53, 0.47)
$H_T > 400 \wedge \alpha_T > (0.51, 0.52)$	$H_T > (240, 300) \vee E_T > (60, 100)$	(0.53, 0.47)
$E_T, H_T > (90, 100, 110, 120)$	$E_T > (60, 100)$	(0.39, 0.10, 0.49, 0.02)
$H_T > (800, 900)$	$H_T > (240, 300)$	(0.76, 0.24)
$p_T^\mu > (22, 24)$	$p_T^\mu > (18, 22)$	(0.80, 0.20)

Table 4.7.: List of L1 and HL triggers utilised in this search, grouped by family, indicating in parentheses their varying thresholds throughout the 2016 LHC run. All quantities related to energy and momentum are quoted in GeV units. The muon trigger is employed in the muon control regions, while all other triggers listed are employed in the signal region and hadronic control regions. The H_T - α_T triggers also have a minimum requirement of 90 GeV on the average p_T of the two leading jets, which did not change throughout run. Also provided is the fraction of the 2016 run for which a given trigger version was the lowest-threshold unprescaled trigger.

are most effective at selecting multijet events with a symmetric topology. The requirement on α_T helps to suppress QCD events and maintain significantly lower thresholds on H_T than would be possible with a pure H_T trigger. These triggers also have a threshold of 90 GeV on the average p_T of the two most energetic jets in the event, which is necessary to maintain reasonable trigger rates. This reduces their efficiency for selecting events with an asymmetric jet topology.

The second type of trigger is one with requirements on both E_T and H_T . These are used to collect events with a monojet or asymmetric topology more effectively than the H_T - α_T triggers. The initial threshold on E_T and H_T was 90 GeV, and was raised throughout the 2016 run up to 120 GeV.

The third type of trigger is one with a requirement only on H_T . In this case the threshold was either 800 or 900 GeV. This trigger is used to collect events in the $H_T > 900$ GeV region in which there is no α_T requirement.

For both the $\mu +$ jets and $\mu\mu +$ jets control regions, events are collected using a trigger that requires at least one isolated muon with a transverse momentum larger than 22 GeV (24 GeV later in the run).

Prior to the HLT, events are filtered by the Level 1 trigger. Each HL trigger is preceded, or *seeded*, by a particular L1 trigger. The L1 seeds for the HL triggers

employed in this search consist of requirements on H_T , E_T and muon p_T , as summarised in Tab. 4.7.

4.7.2. Trigger efficiency

Accurately measuring the efficiency of the triggers is important as these affect the background estimations. Due to imperfect or a lack of trigger emulation in the simulation, the efficiencies need to be measured in data and used to correct the simulation. More details on this will be provided in Sec. 4.9.

The efficiency of a trigger is defined to be the fraction of events satisfying a set of *offline* requirements, such as those of the signal region, that are selected by that trigger. The efficiency should be ideally close to 100%. An inefficiency may arise close to the trigger threshold due to differences in the online and offline reconstruction. For instance, instead of Particle Flow reconstruction, jets in the HLT prefilter are reconstructed using solely calorimeter deposits, and jets in the L1 trigger are reconstructed using relatively coarse calorimeter information.

In order to estimate the efficiency of a trigger using data, one can measure the fraction of events collected by an alternative, *reference* trigger that satisfy the offline criteria. One possibility for a reference trigger is a pure H_T trigger with a relatively low threshold. However, pure H_T triggers are highly prescaled and result in a large statistical uncertainty on the measured efficiency. Unprescaled single electron and muon triggers are instead chosen as references. These provide a sample of events that are inclusive with respect to the variables employed in the signal region triggers.

When using lepton reference triggers to measure efficiencies, one must account for differences in the treatment of leptons in the L1T, the HLT, and offline. As muons deposit a negligible amount of energy in the calorimeters, they are not reconstructed as jets in the L1T and HLT prefilter, whereas electrons are. Offline, both electrons and muons are initially reconstructed as Particle Flow jets, but these ‘fake’ jets are then removed from the event by the cross-cleaning procedure described in Sec. 3.3.5. At the HLT, which also utilises PF reconstruction, cross-cleaning of muons is only employed by the E_T - H_T triggers. Cross-cleaning of electrons is not performed for any of the HL triggers. An inconsistency in the treatment of leptons and jets across the L1, HLT and offline reconstruction chain would introduce a bias in a trigger

efficiency estimate using a lepton trigger reference. For instance, a pure H_T trigger may falsely appear more efficient as the lepton would artificially enlarge the H_T of the event. In order to have a treatment that is as consistent as possible and avoid a bias in the measured trigger efficiency, cross-cleaning of offline electrons and muons is either enabled or disabled as appropriate for the particular trigger being measured. A completely unbiased estimate is not always possible, such as when measuring the H_T and $H_T\text{-}\alpha_T$ efficiencies via a muon sample. However, the triggers are almost fully efficient in the signal region phase space and any bias is covered with a conservative systematic uncertainty, as will be discussed further in Sec. 4.12.

The trigger efficiency is measured using both electron and muon reference triggers as a function of \cancel{H}_T in bins of H_T , both corresponding to quantities computed offline. The efficiency in the 2016 data taking period is shown in Fig. 4.5. The triggers have an efficiency of at least 90% for $\cancel{H}_T > 200$ GeV, and are practically fully efficient above 300 GeV. The discrepancy in the *turn-on* region of the efficiency curve between the muon and electron samples is attributed to differences in cross-cleaning methods, and motivates a selection of $\cancel{H}_T > 200$ GeV in the signal region. One could reduce this threshold to ~ 100 GeV to increase the acceptance of the search, but the lack of a precise knowledge of the trigger efficiency in this region would incur a bias and large uncertainty on the background expectation which would practically nullify the search's sensitivity in this region.

This section has focussed on the signal region triggers. The efficiency of the muon trigger is also measured in data and used to correct the trigger efficiency in the simulation. This will be discussed further in Sec. 4.9.

4.8. Data sets and simulation samples

This section describes the data sets in which the search for supersymmetry takes place, as well as the simulated data sets that aid in the estimation of the background and signal processes.

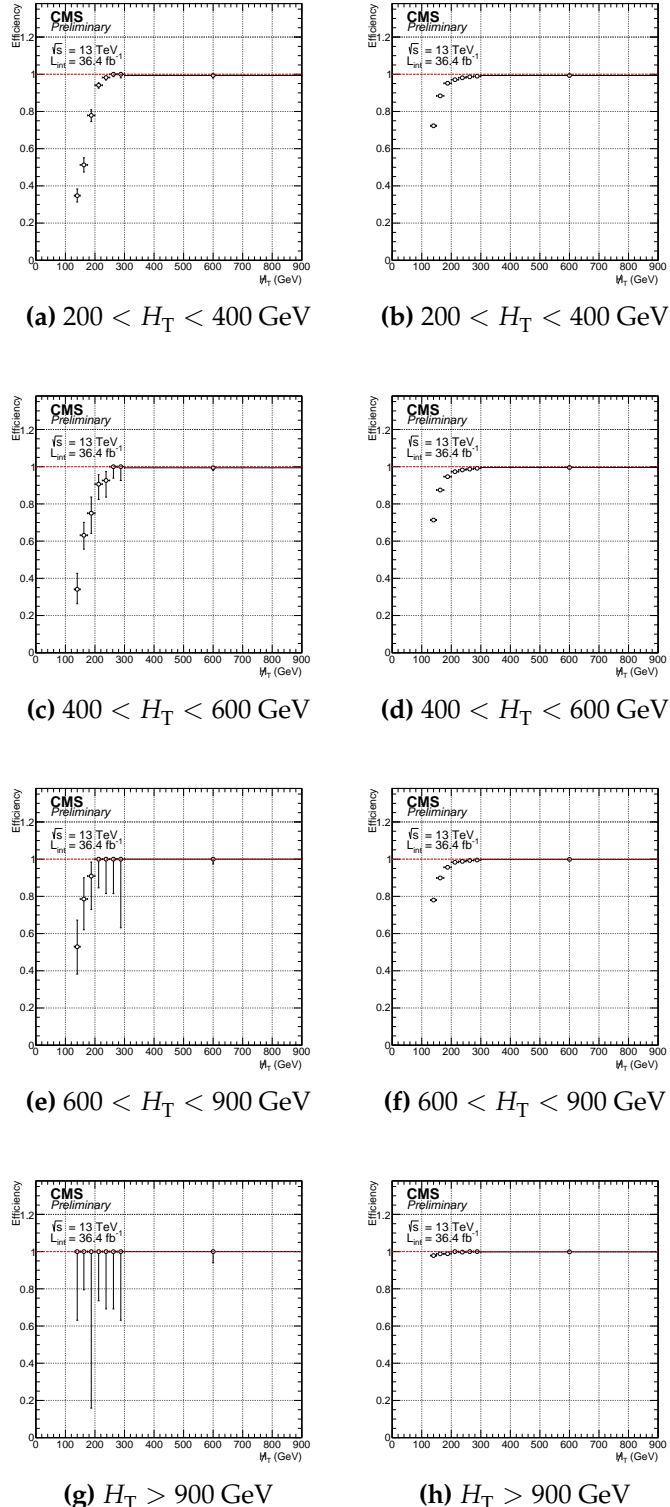


Figure 4.5.: Efficiency of the logical disjunction of the HL triggers in the signal region as a function of offline \mathcal{H}_T and H_T , measured in a data sample collected by a single electron (left) and single muon (right) trigger. Note that only events with $\mathcal{H}_T > 200$ GeV are selected for the signal region.

4.8.1. Data sets

Between 22nd April 2016 and 27th October 2016, the LHC delivered a total integrated luminosity of 40.8 fb^{-1} of proton-proton collisions at a centre of mass energy of $\sqrt{s} = 13 \text{ TeV}$ with a proton bunch spacing of 25 ns. Of this, 37.8 fb^{-1} (93%) was recorded by the CMS detector, and 35.9 fb^{-1} (88%) was certified as containing data of good quality, meaning there were no associated detector or reconstruction issues. The amount of data delivered, recorded and certified over the year is shown in Fig. 4.6. It is the certified 35.9 fb^{-1} of data that form the basis of the search. The data sets that are analysed correspond to those collected by the triggers described in Sec. 4.7.

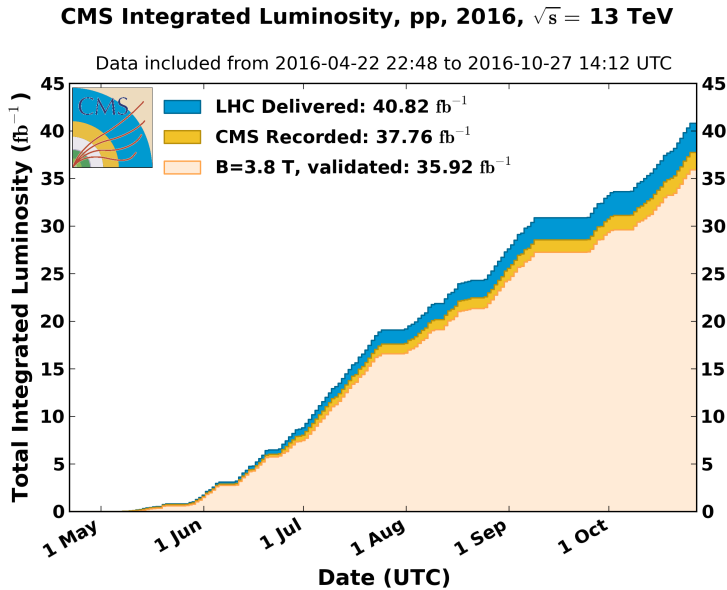


Figure 4.6.: Cumulative integrated luminosity of pp collisions at $\sqrt{s} = 13 \text{ TeV}$ delivered by the LHC, recorded by CMS, and certified as good for physics analysis per day during the year 2016 [59].

4.8.2. Simulation samples

The methods of Monte Carlo event generation, hadronisation and detector simulation were described in Sec. 3.4. The Monte Carlo generation of the main background processes (QCD, Z + jets, W + jets, t \bar{t}) is produced via the MADGRAPH5 [48, 60] generator framework at leading order (LO) precision. As the number of events falls exponentially with the energy scale of the event, and it is the most energetic

events that typically pass the signal region requirements, these samples are generated in various bins of \hat{H}_T , the total hadronic energy of the partons produced in the hard scattering. This improves the statistical precision of the simulation in the phase space region of interest. Single top quark production is generated at next-to-leading order (NLO) using both MADGRAPH5 and POWHEG [49] for the different production channels. The diboson background is generated with PYTHIA8 [50]. While events are generated at LO or NLO, the cross sections of most of the main background processes are computed at next-to-next-to-leading order (NNLO) precision.

The SUSY simplified models are generated with MADGRAPH5. A number of samples with varying masses and lifetimes of the relevant particles are generated. This allows the sensitivity of the search to be explored as a function of these variables. The models with promptly-decaying gluinos and squarks are simulated via a *fast simulation* framework which employs a simplified detector geometry and smearing of the particles' four-vectors, enabling it to perform ~ 100 times faster than a full simulation with GEANT but with comparable accuracy [61].

The formation of R-hadrons through the hadronisation of long-lived gluinos is described by PYTHIA8. The hadronisation process is assumed to yield predominantly meson-like ($\tilde{g}q\bar{q}$) and baryon-like ($\tilde{g}qqq$) states, as well as glueball-like ($\tilde{g}g$) states with probability 10%. Approximately one half of these R-hadrons are charged and half are uncharged. The interaction of R-hadrons with the detector material is simulated with GEANT4 using the model developed in Refs. [62, 63]. However, the results presented in Chap. 5 do not include the model-dependent interactions of R-hadrons. The effect of these interactions will be discussed in Sec. 5.7.

Based on simulation, the estimated number of events of a given process with cross-section σ is given by:

$$\hat{n}_{\text{sim}} = \sigma L_{\text{int}} \frac{N_{\text{pass}}}{N_{\text{gen}}} \quad (4.7)$$

where L_{int} is the integrated luminosity, N_{gen} is the number of events generated, and N_{pass} is the number of events that pass the analysis selections.

4.9. Corrections to simulation

This section describes various ways in which the potential mismodelling of the simulation is corrected for. This usually involves observing a distribution or measuring an efficiency both in data and simulation and applying the data-to-simulation ratio as a weighting factor to each simulated event. These corrections are applied to the simulation of both background and signal processes, as relevant. There are uncertainties associated with each set of correction factors, the treatment of which is detailed in Sec. 4.12.

4.9.1. Pileup

The average number of pileup interactions per bunch crossing during the 2016 run was ~ 20 . The pileup distribution depends on the instantaneous luminosity, which varies over time, and so is not reproduced very accurately by the simulation.

Reweighting factors to correct the pileup distribution in the simulation are derived as a function of the number of pileup interactions. The pileup in a given event in data is calculated from the average instantaneous luminosity measured in the corresponding luminosity section, together with the inelastic proton-proton cross section (63 mb [64]). The correction factors are given by the ratio of the pileup distributions in data and simulation. These range between $\sim 0.8\text{--}1.2$ in the core of the distribution. This is illustrated in Fig. 4.7.

4.9.2. Jet energy

The energies of jets are corrected as described in Sec. 3.3.5. In this case, the corrections are applied on a jet-by-jet basis and so this does not involve a reweighting of the simulated events.

4.9.3. b-tagging

The efficiency for identifying jets as originating from a bottom quark tends to be overestimated in the simulation. Similarly, the probability of incorrectly b-

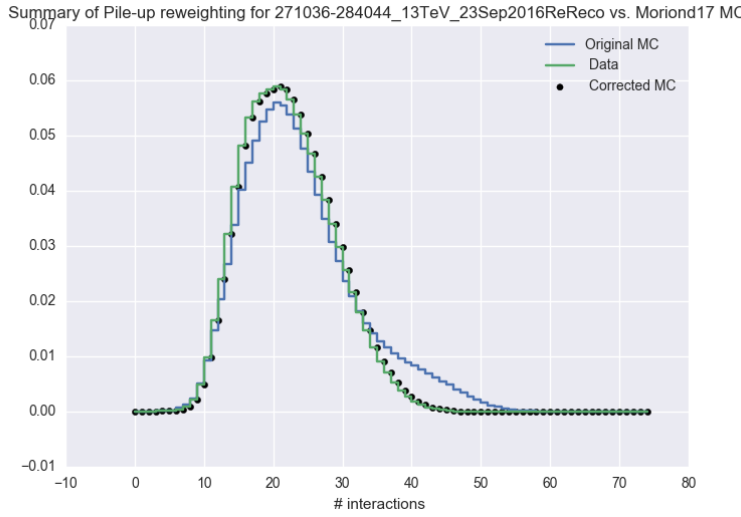


Figure 4.7.: Distribution of the number of pileup interactions in the Monte Carlo (MC) simulation and in data. The ratio of the two is used to derive correction factors that are used to weight the simulated events. The corrected simulated distribution is also shown.

tagging a jet that actually originated from a light flavour (u, d, s) quark or gluon is underestimated. Correction factors for the b-tagging efficiency and fake rate are therefore derived, in bins of jet p_T and η , and applied to the simulation.

The b-tagging probability for a jet originating from a quark (or gluon) of flavour q with transverse momentum p_T and pseudorapidity η is estimated as:

$$\varepsilon(p_T, \eta, q) = \frac{N_{\text{b-tagged}}(p_T, \eta, q)}{N_{\text{total}}(p_T, \eta, q)}, \quad (4.8)$$

where $N_{\text{total}}(p_T, \eta, q)$ is the total number of jets of true flavour q in bin (p_T, η) and $N_{\text{b-tagged}}(p_T, \eta, q)$ is the number of such jets that are b-tagged. The flavour q is labelled as one of three types — b, c, or light (u, d, s, or gluon).

In simulated events, the true flavour of a jet is determined according to whether there are any bottom or charmed hadrons contained within the jet's cone. In data, the b-tagging efficiency is measured in a sample of $t\bar{t}$ events or jets containing a muon, and the mistagging probability is measured using jets with a negative impact parameter or negative decay length [65]. The ratio of the b-tagging probability in data and simulation provides a correction factor $f(p_T, \eta, q)$ that is used to weight

the events from simulation. The correction factors are in the range $\sim 0.95\text{--}1$ and $\sim 1\text{--}1.2$ for bottom quarks and light partons, respectively.

While the correction factors derived in Ref. [65] are for an inclusive set of jets, the b-tagging probabilities are also measured in the signal and control regions of the search. Given these probabilities and the correction factors, for each simulated event the probability of observing the corresponding combination of tagged and non-tagged jets in data and simulation is computed as:

$$P_{\text{sim}} = \prod_{j \text{ b-tagged}} \varepsilon_j \prod_{j \text{ not b-tagged}} (1 - \varepsilon_j) \quad (4.9)$$

$$P_{\text{data}} = \prod_{j \text{ b-tagged}} f_j \varepsilon_j \prod_{j \text{ not b-tagged}} (1 - f_j \varepsilon_j) \quad (4.10)$$

where $\varepsilon_j \equiv \varepsilon(p_T(j), \eta(j), q(j))$ is the probability of jet j being b-tagged, as measured according to Eq. 4.8, and $f_j \equiv f(p_T(j), \eta(j), q(j))$ is the corresponding correction factor. The simulated event is then weighted by the ratio:

$$w = \frac{P_{\text{data}}}{P_{\text{sim}}} \quad (4.11)$$

Signal models that are simulated via a fast simulation procedure are weighted according to correction factors that are derived to match the b-tagging probability in full simulation, and are then weighted again using the above procedure to match the b-tagging probability in data.

4.9.4. Lepton identification, isolation and triggering

The efficiencies of the muon trigger and the muon identification and isolation requirements described in Sec. 4.1 are corrected for in the simulated events that enter the muon control regions. A similar correction is made for muons and electrons that form part of the ‘lost lepton’ background in the signal region. These efficiencies are measured in data and simulation using the *tag-and-probe method* [66] as explained in the following.

The tag-and-probe method takes advantage of a known mass resonance to identify particles of a desired type and evaluate various efficiency measures such as the ability to reconstruct or trigger such particles. In this case the particles of interest are muons (or electrons) and they are identified via the Z boson resonance. First, a muon that satisfies stringent quality criteria is selected and labelled as the *tag*. A second muon satisfying looser requirements, labelled the *probe*, is then paired with the tag if it is oppositely charged and the invariant mass of the pair is within a ~ 30 GeV window around the Z boson mass. These requirements on the tag and probe mean that they are almost certainly real muons. It is then checked whether the probe satisfies the selection whose efficiency is of interest. An estimate of the efficiency is given by the fraction of probes that pass the selection. Note that a tag satisfies the probe requirements by definition, and so a dimuon event in which both muons are tagged contains two tag and probe pairs. A tag is not considered if it is paired with more than one probe.

The tag-and-probe efficiency estimate is slightly biased to a lower value than the true efficiency. This is because in events in which there is a tag and a ‘passing’ probe that does not also satisfy the tag requirements, the tag is not counted towards the efficiency. However, the efficiency estimate is also biased higher because the method does not count events in which neither muon is a tag. Overall, the estimated efficiency is typically within $\sim 1\%$ of the true efficiency, and the bias is expected to be negligible in the data-to-simulation correction factors, as the bias largely cancels out in the ratio.

A muon is labelled as a tag if it satisfies the stringent quality criteria described in Sec. 4.1 and is also reconstructed at the trigger level and fires the muon trigger. The latter is determined by attempting to match the offline muon to an HLT muon within a cone of size $\Delta R = 0.3$ and checking whether the matched trigger object satisfies the trigger requirements. The requirements on the probe depend on the particular measurement being made. The three measurements of identification, isolation and trigger efficiency are performed sequentially such that the probe requirements for one measurement are the same as those for a passing probe in the previous measurement. This is done because the overall efficiency is given by the product of conditional probabilities:

$$\varepsilon_{\text{ID},\text{iso,trig}} = \varepsilon_{\text{ID}} \varepsilon_{\text{iso}|\text{ID}} \varepsilon_{\text{trig}|\text{ID},\text{iso}}. \quad (4.12)$$

When measuring the identification efficiency, the probe is taken as any reconstructed track, and the passing requirement is that it satisfies the muon quality criteria of Sec. 4.1 except for the isolation requirement. These are then the requirements for a probe in the isolation efficiency measurement, and the probe in this case is checked to satisfy the $I_{\text{rel}} < 0.1$ requirement. These are then the input probes for the trigger efficiency measurement, and it is checked whether they cause the muon trigger to fire.

A small amount of combinatoric and fake muon background is present when selecting tag and probe pairs. This background is subtracted and the efficiency extracted via an extended simultaneous maximum likelihood fit to the invariant mass distributions of the passing and failing probes. The two mass distributions are modelled, respectively, by the following probability densities:

$$p_{\text{pass}}(m) = \left(\frac{\varepsilon s}{\varepsilon s + b_{\text{pass}}} \right) p_{\text{pass}}^{\text{sig}}(m) + \left(\frac{b_{\text{pass}}}{\varepsilon s + b_{\text{pass}}} \right) p_{\text{pass}}^{\text{bkg}}(m) \quad (4.13)$$

$$p_{\text{fail}}(m) = \left(\frac{(1 - \varepsilon)s}{(1 - \varepsilon)s + b_{\text{fail}}} \right) p_{\text{fail}}^{\text{sig}}(m) + \left(\frac{b_{\text{fail}}}{(1 - \varepsilon)s + b_{\text{fail}}} \right) p_{\text{fail}}^{\text{bkg}}(m) \quad (4.14)$$

where ε is the efficiency parameter; s , b_{pass} and b_{fail} are the total number of events attributed to signal, background passing probes and background failing probes; and $p_{\text{pass}}^{\text{sig}}$, $p_{\text{pass}}^{\text{bkg}}$, $p_{\text{fail}}^{\text{sig}}$ and $p_{\text{fail}}^{\text{bkg}}$ are the signal and background probability densities for passing and failing probes. The signal is usually modelled by a Voigtian distribution, which is a Breit-Wigner distribution convoluted with a Gaussian distribution to account for smearing due to detector resolution, while the background is usually modelled by an exponential distribution. The extended likelihood function can then be written as:

$$\mathcal{L} = \mathcal{P}(es + b_{\text{pass}})\mathcal{P}((1 - \varepsilon)s + b_{\text{fail}}) \prod_{i \text{ pass}} p_{\text{pass}}(m_i) \prod_{i \text{ fail}} p_{\text{fail}}(m_i), \quad (4.15)$$

where the products are over all corresponding probes i , and the \mathcal{P} 's are Poisson distributions for the total number of passing and failing events observed. An example of the fitting result in data is shown in Fig. 4.8.

The efficiencies and corresponding data-to-simulation corrections are derived as a function of muon p_{T} and η . The identification efficiency is around 97-99% and the

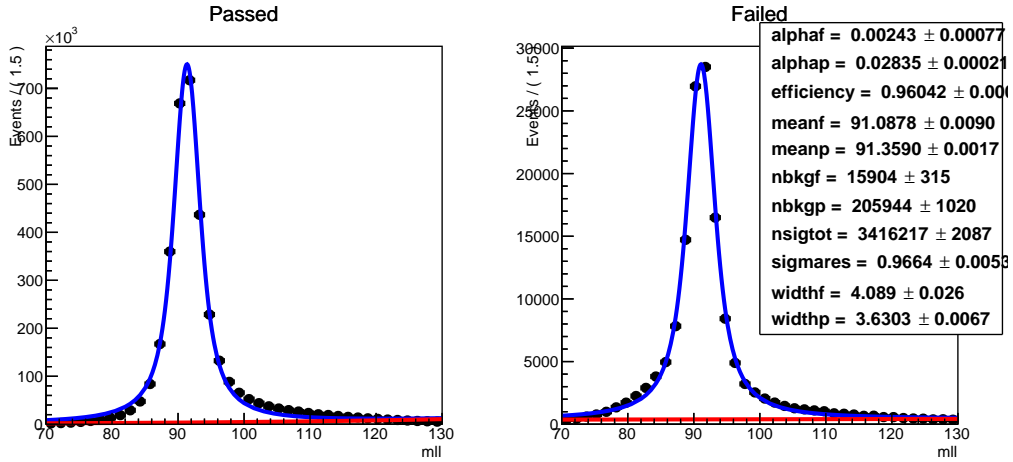


Figure 4.8.: Result of the tag-and-probe dimuon invariant mass fitting procedure to passing (left) and failing (right) probes for an example isolation efficiency measurement in data for muons with $50 < p_T < 60$ GeV. The blue (red) curves are the fitted signal (background) distributions. The fitted efficiency in this example is 96.0%.

corresponding correction factors are in the range 0.97-0.99. The efficiency of the isolation requirement varies between 90-99% and the correction factors are around 0.99-1. The trigger efficiency is measured to be approximately 90%, with correction factors of about 0.98. In the $\mu\mu + \text{jets}$ control region, the trigger efficiency is higher, as the probability to trigger on at least one muon is $1 - (1 - 0.9)(1 - 0.9) = 99\%$.

The efficiencies and correction factors are then propagated to the simulated events as follows. The expected number of events in the $\mu + \text{jets}$ control region according to the simulation, ignoring the normalisation due to the integrated luminosity and cross section, is given by:

$$N_{\mu+\text{jets}} = \sum a_\mu \varepsilon_{\text{ID}}^\mu \varepsilon_{\text{iso}}^\mu \varepsilon_{\text{trig}}^\mu, \quad (4.16)$$

where the sum runs over all simulated $W(\rightarrow \ell\nu) + \text{jets}$ and $t\bar{t}$ events that contain one generator-level muon satisfying the $\mu + \text{jets}$ control region selections except those relating to the muon acceptance, identification, isolation and trigger. The acceptance term a_μ is either 1 if the muon satisfies the p_T and η acceptance requirements, or 0 if it does not. The efficiency terms are conditional on one another as defined in Eq. 4.12, and their values depend on the muon's p_T and η . Similarly, the expected number of events in the $\mu\mu + \text{jets}$ control region is given by:

$$N_{\mu\mu+\text{jets}} = \sum (a_{\mu_1} a_{\mu_2}) (\varepsilon_{\text{ID}}^{\mu_1} \varepsilon_{\text{ID}}^{\mu_2}) (\varepsilon_{\text{iso}}^{\mu_1} \varepsilon_{\text{iso}}^{\mu_2}) [1 - (1 - \varepsilon_{\text{trig}}^{\mu_1})(1 - \varepsilon_{\text{trig}}^{\mu_2})], \quad (4.17)$$

where the sum is now over all simulated $Z(\rightarrow \mu\mu) + \text{jets}$ and $t\bar{t}$ events that have two generator-level muons and satisfy the $\mu\mu + \text{jets}$ control region selections except those relating to the muon acceptance, identification, isolation and trigger. The expected number of lost lepton background events in the signal region is given by:

$$N_{\text{signal}} = \sum \left[(1 - a_\ell) + a_\ell (1 - \varepsilon_{\text{ID}}^\ell) + a_\ell \varepsilon_{\text{ID}}^\ell (1 - \varepsilon_{\text{iso}}^\ell) + a_\ell \varepsilon_{\text{ID}}^\ell \varepsilon_{\text{iso}}^\ell (1 - \varepsilon_{\text{trig}}^\ell) \right], \quad (4.18)$$

where the sum runs over all simulated $W(\rightarrow \ell\nu) + \text{jets}$ and $t\bar{t}$ events that contain one generator-level muon or electron (labelled ℓ) and satisfy the signal region selections except those relating to the lepton acceptance, identification, isolation and trigger. The efficiencies in these three equations are scaled by the data-to-simulation correction factors derived from the tag-and-probe method to obtain the corrected number of leptonic standard model events in the signal and control regions.

4.9.5. Trigger

Unlike the muon triggers, the signal region triggers are not emulated in the simulation. Instead of determining data-to-simulation correction factors, the trigger efficiencies measured in data as a function of H_T and \cancel{H}_T using an electron reference sample (as described in Sec. 4.7) are themselves applied as corrections. As seen in Fig. 4.5, these can be as low as 90% at low \cancel{H}_T , but are close to unity for $\cancel{H}_T > 300 \text{ GeV}$.

4.9.6. Theoretical calculation of V+jets production

As mentioned in Sec. 4.8.2, the simulation samples for the vector boson production processes, namely $Z + \text{jets}$ and $W + \text{jets}$, are generated at leading order, as this allows a larger number of events to be simulated. The samples are corrected for missing higher order terms in the matrix element calculations as a function of the boson's transverse momentum. This is done by deriving NLO QCD correction factors using MADGRAPH5, and NLO electroweak correction factors from theoretical calculations [67]. The combined NLO QCD+EW corrections range from

approximately 1.4 at a boson p_T of 200 GeV to 0.9 at 800 GeV, for both the Z + jets and W + jets processes.

4.9.7. Initial state radiation in t̄t events

Simulated events of the t̄t background process are weighted to improve the agreement with data of the multiplicity of jets from initial state radiation. The data-to-simulation correction factors are derived as a function of the number of ISR jets in an event, and take on values between 0.92 and 0.51 for an ISR multiplicity of 1 and 6, respectively.

4.9.8. Cross-sections

Although the dominant standard model background processes are normalised using the most accurate cross section calculations available (using NLO or NNLO precision), the finite perturbative order combined with the high H_T and E_T selections means that the overall simulated yields of the SM processes in the search regions are not in agreement with those in data.

Corrections to the cross sections of the dominant background processes, namely Z + jets, W + jets and t̄t, that are appropriate for the phase space covered by the search, are derived in a sideband of the μ + jets and $\mu\mu$ + jets control regions defined by a selection of $100 < \cancel{H}_T < 200$ GeV. The two \cancel{H}_T sidebands are binned in n_{jet} , n_b and H_T identically to their control region counterparts. The procedure is done after all other corrections to the simulation samples have been applied.

As the background composition in the signal and control regions is similar, these cross section corrections have a very small effect on the background estimations as they cancel out in the simulation-based transfer factor ratios (explained in Sec. 4.10.1). However, this is not the case for some of the tests that are used to derive systematic uncertainties (which will be described in Sec. 4.12.2) and so the lack of corrections would unnecessarily inflate these uncertainties.

In order to extract the cross section correction factors, a simultaneous binned maximum likelihood fit is performed over both \cancel{H}_T sideband regions, in which the three correction parameters (one for each of the Z + jets, W + jets and t̄t processes)

are freely floating such that they modify the simulated yields to give the best agreement with those in data. The likelihood function is given by:

$$\mathcal{L} = \mathcal{U}(f_W)\mathcal{U}(f_Z)\mathcal{U}(f_{t\bar{t}}) \prod_b \mathcal{P}_{(\mu+\text{jets})} \left(f_W \lambda_W^b + f_{t\bar{t}} \lambda_{t\bar{t}}^b \right) \prod_b \mathcal{P}_{(\mu\mu+\text{jets})} \left(f_Z \lambda_Z^b + f_{t\bar{t}} \lambda_{t\bar{t}}^b \right) \quad (4.19)$$

where the λ^b 's are the number of background events in an (n_{jet} , n_b , H_T) bin b given by the simulation for a given standard model process, the f 's are the cross section correction factors, the \mathcal{U} 's define a uniform distribution (between 0 and an arbitrarily large value) for the correction parameters, and the \mathcal{P} 's define a Poisson distribution in each bin.

The cross section correction factors for the $Z + \text{jets}$, $W + \text{jets}$ and $t\bar{t}$ processes are mainly constrained, respectively, by the $\mu\mu + \text{jets}$ sideband, the $\mu + \text{jets}$ sideband, and a combination of the two sidebands. The values of the correction factors obtained from the fit are given in Tab. 4.8.

Table 4.8.: Cross section correction factors for the three dominant standard model background processes, along with an indication of the most constraining sideband region for each process.

SM process	Sideband region	Correction factor
$Z + \text{jets}$	$\mu\mu + \text{jets}$	$f_Z = 0.91$
$W + \text{jets}$	$\mu + \text{jets}$	$f_W = 1.06$
$t\bar{t}$	$\mu + \text{jets}, \mu\mu + \text{jets}$	$f_{t\bar{t}} = 0.93$

4.9.9. Statistical precision at large n_b

The following describes a method by which the statistical precision of the background simulation samples in the high n_b bins is improved. This is particularly useful for the $n_b \geq 3$ region, which is populated by standard model processes through the incorrect tagging of light flavour jets as b-jets, mainly $t\bar{t}$ events in which the two b-jets from the top quarks are correctly tagged and an additional jet is mistagged. As the mistagging probability is quite small, the number of such events in simulation is limited. Reducing the statistical uncertainty on the expected

standard model background in the high n_b region helps to improve the sensitivity of the search to SUSY processes involving the production of multiple heavy quarks, as well as processes containing displaced jets, as will be seen in Chap. 5.

First, the b-tagging probabilities for bottom, charm and light flavour jets (ε_b , ε_c , ε_l) are computed in simulation in bins of $(n_{\text{jet}}, H_T, \mathcal{H}_T)$, after applying the p_T and η dependent correction weights described in Sec. 4.9.3. For a given number of jets n_q^{gen} of underlying flavour q (as determined by generator-level information), the number of such jets that are b-tagged n_q^{tag} follows a binomial distribution with probability parameter ε_q , $P(n_q^{\text{tag}}|n_q^{\text{gen}}, \varepsilon_q)$. For an event containing a particular combination of underlying jet flavours $(n_b^{\text{gen}}, n_c^{\text{gen}}, n_l^{\text{gen}})$, the probability of observing a combination of b-tagged jets $(n_b^{\text{tag}}, n_c^{\text{tag}}, n_l^{\text{tag}})$ is given by the product:

$$\begin{aligned} P\left(n_b^{\text{tag}}, n_c^{\text{tag}}, n_l^{\text{tag}} | n_b^{\text{gen}}, n_c^{\text{gen}}, n_l^{\text{gen}}\right) \\ = P\left(n_b^{\text{tag}} | n_b^{\text{gen}}, \varepsilon_b\right) P\left(n_c^{\text{tag}} | n_c^{\text{gen}}, \varepsilon_c\right) P\left(n_l^{\text{tag}} | n_l^{\text{gen}}, \varepsilon_l\right). \end{aligned} \quad (4.20)$$

If there are $N(n_b^{\text{gen}}, n_c^{\text{gen}}, n_l^{\text{gen}})$ simulation events of a particular process with such combination of underlying jet flavour, the number of these events that result in a combination of b-tagged jets $(n_b^{\text{tag}}, n_c^{\text{tag}}, n_l^{\text{tag}})$ follows a binomial distribution with the above probability, with an expected value of:

$$\begin{aligned} E\left[N\left(n_b^{\text{tag}}, n_c^{\text{tag}}, n_l^{\text{tag}} | n_b^{\text{gen}}, n_c^{\text{gen}}, n_l^{\text{gen}}\right)\right] \\ = N(n_b^{\text{gen}}, n_c^{\text{gen}}, n_l^{\text{gen}}) P\left(n_b^{\text{tag}}, n_c^{\text{tag}}, n_l^{\text{tag}} | n_b^{\text{gen}}, n_c^{\text{gen}}, n_l^{\text{gen}}\right). \end{aligned} \quad (4.21)$$

The total expected number of events containing n_b b-tagged jets in a given $(n_{\text{jet}}, H_T, \mathcal{H}_T)$ bin is then the sum of this expected value over all combinations of underlying jet flavours that sum to n_{jet} and all combinations of b-tagged jets that sum to n_b :

$$N(n_b) = \sum_{n_b^{\text{gen}} + n_c^{\text{gen}} + n_l^{\text{gen}} = n_{\text{jet}}} \sum_{n_b^{\text{tag}} + n_c^{\text{tag}} + n_l^{\text{tag}} = n_b} E\left[N\left(n_b^{\text{tag}}, n_c^{\text{tag}}, n_l^{\text{tag}} | n_b^{\text{gen}}, n_c^{\text{gen}}, n_l^{\text{gen}}\right)\right]. \quad (4.22)$$

The strength of the method comes from a more effective utilisation of all simulated events. Each simulated event, rather than resulting in one particular $(n_b^{\text{tag}}, n_c^{\text{tag}}, n_l^{\text{tag}})$ realisation, contributes to the estimation of the yield in multiple n_b bins. The statistical uncertainties in the highest n_b bins are found to be approximately three

times smaller than those obtained directly from the simulated events. As a means of validation, it is checked that the yields estimated with this method are consistent with those obtained directly from simulation.

Throughout the remainder of the thesis, all simulation-based event yields are obtained via this method. Similarly, all references to simulated events assume the inclusion of all the corrections described in this section.

4.10. Estimation of electroweak background processes

An accurate knowledge of the expected number of standard model background events is very important when searching for new physics. Relying on simulation, even after applying the corrections discussed in the previous section, would introduce a bias in the background estimation due to imperfect modelling. A data-driven approach is therefore utilised which combines simulated events and control region data to perform a more accurate estimation.

This section describes the methods of background estimation for the processes with genuine E_T , which involves an estimation per $(n_{\text{jet}}, n_b, H_T)$ bin and another one for the \cancel{H}_T bins within each $(n_{\text{jet}}, n_b, H_T)$ bin. The estimation of the much smaller QCD background will be discussed in Sec. 4.11.

4.10.1. The n_{jet} , n_b and H_T dimensions

The number of background events in each $(n_{\text{jet}}, n_b, H_T)$ bin is estimated using the muon control regions. As mentioned in Sec. 4.5.2 and 4.6, these are chosen to be enriched in the background processes they are trying to estimate and are binned identically in $(n_{\text{jet}}, n_b, H_T)$ (with the exception of the n_b dimension in the $\mu\mu + \text{jets}$ sample). The $\mu\mu + \text{jets}$ control region is used to estimate the $Z(\rightarrow \nu\nu) + \text{jets}$ background, while the $\mu + \text{jets}$ control region is used to estimate the sum of the $W(\rightarrow \ell\nu) + \text{jets}$, $t\bar{t}$ and residual backgrounds, which will be collectively labelled as $W/t\bar{t}$.

The estimated number of events of a given background process in a particular $(n_{\text{jet}}, n_b, H_T)$ bin is related to the total number of events in the same bin of the corresponding control region in data $N_{\text{control}}^{\text{data}}(n_{\text{jet}}, n_b, H_T)$ and simulation $N_{\text{control}}^{\text{sim}}(n_{\text{jet}}, n_b, H_T)$

and the number of events of that background in the same bin of the signal region in simulation $N_{\text{signal}}^{\text{sim}}(n_{\text{jet}}, n_{\text{b}}, H_{\text{T}})$ by:

$$\hat{N}_{\text{signal}}(n_{\text{jet}}, n_{\text{b}}, H_{\text{T}}) = \frac{N_{\text{signal}}^{\text{sim}}(n_{\text{jet}}, n_{\text{b}}, H_{\text{T}})}{N_{\text{control}}^{\text{sim}}(n_{\text{jet}}, n_{\text{b}}, H_{\text{T}})} N_{\text{control}}^{\text{data}}(n_{\text{jet}}, n_{\text{b}}, H_{\text{T}}). \quad (4.23)$$

A special case of this formula applies to the $Z(\rightarrow \nu\nu) + \text{jets}$ process in the $n_{\text{b}} = 1, 2, 3$ and ≥ 4 bins, which is estimated in each of these bins using the $n_{\text{b}} \geq 1$ bin in the $\mu\mu + \text{jets}$ control region.

The extrapolation from the control region to the signal region is performed via the simulation-based ratio of yields in the above equation, referred to as a *transfer factor*:

$$T(n_{\text{jet}}, n_{\text{b}}, H_{\text{T}}) = \frac{N_{\text{signal}}^{\text{sim}}(n_{\text{jet}}, n_{\text{b}}, H_{\text{T}})}{N_{\text{control}}^{\text{sim}}(n_{\text{jet}}, n_{\text{b}}, H_{\text{T}})}. \quad (4.24)$$

The transfer factor can be viewed as a way of accounting for the different branching fraction, acceptance and identification efficiency of a given process between the signal and control region. For instance, the Z boson's branching ratio between neutrinos and muons is 9, and unlike the weakly interacting neutrinos, the muons are subject to acceptance and identification requirements. The transfer factor also accounts for the different kinematic selections, namely on α_{T} and $\Delta\phi_{\text{min}}^*$, which are not used in the control regions. The transfer factors used in the estimations of the $W/\text{t}\bar{t}$ background from the $\mu + \text{jets}$ control region and the $Z(\rightarrow \nu\nu) + \text{jets}$ background from the $\mu\mu + \text{jets}$ control region are denoted as $T(\mu \rightarrow W/\text{t}\bar{t})$ and $T(\mu\mu \rightarrow Z)$, respectively.

Equivalently, the estimation in Eq. 4.23 can also be viewed as a way of correcting the number of events obtained from the simulation according to the data-to-simulation discrepancy ratio in the control region bin:

$$\hat{N}_{\text{signal}}(n_{\text{jet}}, n_{\text{b}}, H_{\text{T}}) = \frac{N_{\text{control}}^{\text{data}}(n_{\text{jet}}, n_{\text{b}}, H_{\text{T}})}{N_{\text{control}}^{\text{sim}}(n_{\text{jet}}, n_{\text{b}}, H_{\text{T}})} N_{\text{signal}}^{\text{sim}}(n_{\text{jet}}, n_{\text{b}}, H_{\text{T}}). \quad (4.25)$$

This highlights the importance of having similar kinematic requirements and background compositions, as well as a similar binning scheme, in the control and signal regions, as the discrepancy between data and simulation in a given bin of the

control region is likely to be similar to that in the corresponding bin in the signal region.

Although the $\mu\mu + \text{jets}$ control region is binned more inclusively in the n_b variable than the signal region (which for $n_b \geq 1$ is equivalent to taking the shape of the n_b distribution directly from simulation), it is checked that this does not bias the background estimation in a similar way as the validation of the \cancel{H}_T dimension, which will be discussed in the next section.

The transfer factors, and therefore the background estimates, are robust against many sources of systematic effects relating to kinematic mismodelling and theoretical uncertainties, as these cancel out in the transfer factor ratio to a large extent. Several sources of systematic uncertainty are nevertheless accounted for in the estimated backgrounds, as will be discussed in Sec. 4.12.

4.10.2. The \cancel{H}_T dimension

The transfer factor method just described is used to estimate the expected number of background events in each $(n_{\text{jet}}, n_b, H_T)$ bin, inclusive with respect to \cancel{H}_T . The method could be applied to the estimation of each $(n_{\text{jet}}, n_b, H_T, \cancel{H}_T)$ bin; however, the additional binning in the \cancel{H}_T dimension that would be required in the control regions would greatly reduce the number of events in each control region bin (the ‘curse of dimensionality’). This would cause the statistical uncertainty in the estimated background to be too large and degrade the sensitivity of the search. Instead, the number of background events in each \cancel{H}_T bin within a given $(n_{\text{jet}}, n_b, H_T)$ bin is estimated according to the \cancel{H}_T distribution obtained directly from simulation. In other words, the *shape* of the \cancel{H}_T distribution in each $(n_{\text{jet}}, n_b, H_T)$ is taken from simulation, while the *normalisation* of the distribution is obtained via the transfer factor method.

It is important to assess whether there is a potential bias in the background estimation due to the direct use of simulated events. This is done by comparing the \cancel{H}_T distributions in every $(n_{\text{jet}}, n_b, H_T)$ bin between data and simulation in the two muon control regions. Only the shapes are compared, as the normalisation is determined using the data-driven transfer factor method. If the simulation’s modelling of the \cancel{H}_T shape is reasonable, the ratio of events between data and simulation in each \cancel{H}_T bin is expected to be unity.

A linear model is fit to the data-to-simulation ratio versus \mathcal{H}_T using a χ^2 minimisation procedure, and it is checked that the estimated value of the linear parameter is statistically compatible with zero. This is done for all $(n_{\text{jet}}, n_b, H_T)$ bins by computing the z-score, which is given by the value of the linear parameter divided by its uncertainty. The result of the fit for two example $(n_{\text{jet}}, n_b, H_T)$ bins is shown in Fig. 4.9. Figure 4.10 shows the distribution of the linear parameter's z-score over all $(n_{\text{jet}}, n_b, H_T)$ bins. It can be seen that the z-scores are approximately Gaussian distributed with a mean and standard deviation compatible with zero and one, respectively. Performing the background estimation in the \mathcal{H}_T dimension using the distributions obtained directly from simulation is therefore considered valid.

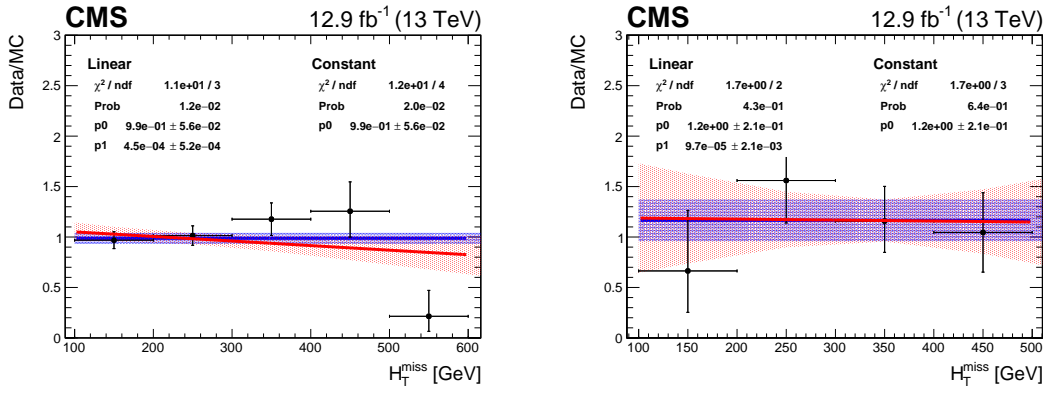


Figure 4.9.: The data-to-simulation ratio of event counts as a function of \mathcal{H}_T for two example $(n_{\text{jet}}, n_b, H_T)$ categories, along with the fit of a linear (and constant) function.

The uncertainties on the linear fits are used to assign systematic uncertainties on these simulated \mathcal{H}_T distributions, as will be discussed in Sec. 4.12.3.

4.11. Estimation of QCD background processes

As discussed in Sec. 4.4, the QCD background is very difficult to estimate accurately, and so a choice is made to reduce this background to a very small level by means of dedicated variables such as α_T and $\Delta\phi_{\min}^*$. In this way, a large uncertainty on a small QCD contribution does not have a large negative impact on the search's sensitivity to BSM physics.

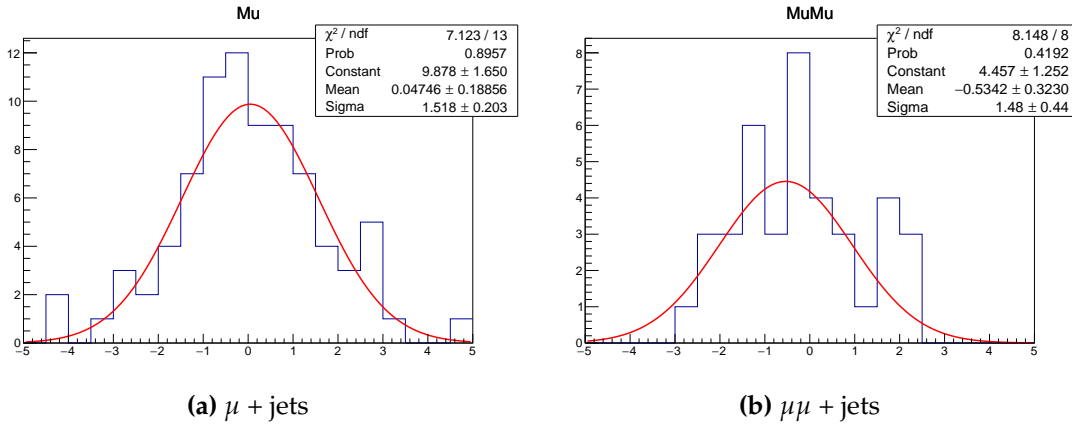


Figure 4.10.: The distribution of the z-scores of the linear parameter fitted to the H_T distributions for all $(n_{\text{jet}}, n_b, H_T)$ categories in both the $\mu + \text{jets}$ and $\mu\mu + \text{jets}$ control regions. A fitted Gaussian distribution is overlaid.

The residual QCD background is estimated in a data-driven way using the hadronic control regions, which are enriched in QCD events, in a similar way as the electroweak background processes. The three hadronic control regions consist of three signal region sidebands with respect to the \cancel{H}_T/E_T and $\Delta\phi_{\min}^*$ variables, as well as a ‘double sideband’ in which the requirements on both \cancel{H}_T/E_T and $\Delta\phi_{\min}^*$ are inverted. These were summarised in Sec. 4.5.2. The estimated QCD yields are checked to be consistent between the three sidebands, and the final estimate is taken as the average of all three weighted by their uncertainties.

The QCD background estimation is performed in a similar way as the electroweak background estimation, namely via the transfer factor method described in Sec. 4.10. In this case, because of the statistical limitation of the QCD simulation samples, only the normalisation per (n_{jet}, H_T) bin, rather than per $(n_{\text{jet}}, n_b, H_T)$ bin, is estimated from the control regions. The (n_b, H_T) dimension is treated differently, as will be discussed later in this section. Analogously to Eq. 4.23, the transfer factor equation is given by:

$$\hat{N}_{\text{signal}}(n_{\text{jet}}, H_{\text{T}}) = \frac{N_{\text{signal}}^{\text{sim}}(n_{\text{jet}}, H_{\text{T}})}{N_{\text{control}}^{\text{sim}}(n_{\text{jet}}, H_{\text{T}})} \hat{N}_{\text{control}}^{\text{data}}(n_{\text{jet}}, H_{\text{T}}). \quad (4.26)$$

where $N_{\text{signal}}^{\text{sim}}(n_{\text{jet}}, H_{\text{T}})$ and $N_{\text{control}}^{\text{sim}}(n_{\text{jet}}, H_{\text{T}})$ are the number of simulated QCD events in bin $(n_{\text{jet}}, H_{\text{T}})$ in the signal region and sideband, and $\hat{N}_{\text{control}}^{\text{data}}(n_{\text{jet}}, H_{\text{T}})$ is the estimated number of QCD events in the same sideband bin in data. There is a non-

negligible contribution from electroweak processes in the sideband, and so instead of using the total number of events in the hadronic control region (as in Eq. 4.23), only the number of events from QCD processes is used. This is done by estimating the electroweak background in the hadronic sideband via sidebands of the two muon control regions, in exactly the same way as the electroweak background estimation is performed in the signal region via the muon control regions (Sec. 4.10), accounting for the systematic uncertainties that will be discussed in Sec. 4.12. This is subtracted from the total number of events observed in the hadronic sideband to give an estimate of the number of QCD events $\hat{N}_{\text{control}}^{\text{data}}(n_{\text{jet}}, H_{\text{T}})$.

The results of the QCD background estimation procedure is shown in Fig. 4.11. It can be seen that the number of QCD events in each $(n_{\text{jet}}, H_{\text{T}})$ bin of the signal region is estimated to be very small, and the contribution is less than 1% of the total background composition in most bins of the signal region.

Within each $(n_{\text{jet}}, H_{\text{T}})$ bin, the shape of the distribution of events across n_b and H_{T} is taken directly from the simulation of the electroweak processes. This is chosen instead of the QCD simulation as the statistical power of the electroweak simulation is much larger. It is checked that the electroweak (n_b, H_{T}) distribution is consistent with the QCD distribution within uncertainties.

4.12. Uncertainties on background estimation

The electroweak background estimation procedure is subject to both statistical and systematic uncertainties. This section describes the various sources of systematic uncertainty and the methods used to estimate the size of these uncertainties and their effect on the background estimates. The uncertainties are then incorporated into the statistical model employed to determine the sensitivity of the search to BSM physics, as will be explained in Sec. 5.3.

The systematic uncertainties on the electroweak background estimates are broadly encoded in one of two ways – as uncertainties on the transfer factors which determine the number of events in each $(n_{\text{jet}}, n_b, H_{\text{T}})$ bin, and uncertainties on how these events are distributed across the corresponding H_{T} bins.

The systematic uncertainties on the transfer factors are determined in two ways. The first concerns theoretical and experimental sources of uncertainty on the correc-

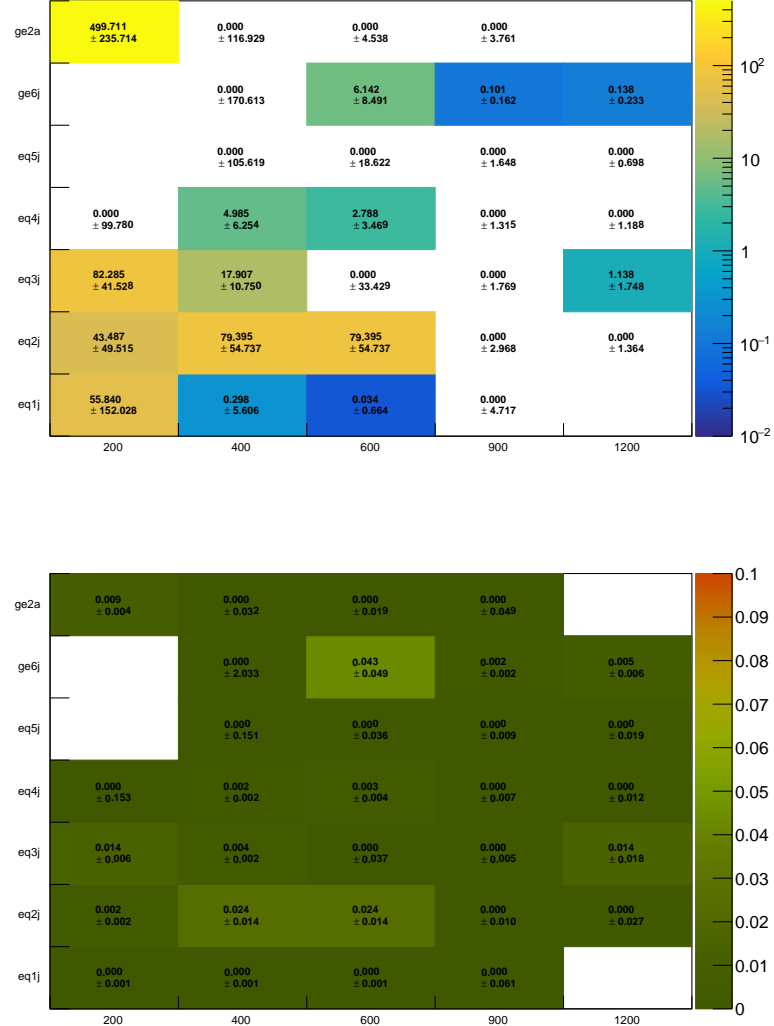


Figure 4.11.: The estimated number of QCD events in each (n_{jet} , H_T) bin of the signal region (top), and the corresponding ratio of expected QCD and electroweak events (bottom).

tions described in Sec. 4.9 that are applied to the simulation. The second concerns potential sources of bias that may arise in the background estimation due to different selections in the signal and control regions.

All of these uncertainties are discussed in the following sub-sections. They are summarised, along with representative sizes in Tab. 4.9.

Source of uncertainty	Uncertainty on transfer factor (%)	
	$T(\mu \rightarrow W/t\bar{t})$	$T(\mu\mu \rightarrow Z)$
Simulation variations		
Pileup	0.6-3.8	2.3-2.8
Jet energy	3.4-5.5	5.3-8.0
b-tagging (heavy quark)	0.4-0.6	0.3-0.6
b-tagging (light quark)	0.1-1.4	0.2-1.8
Lepton selection	5	2
Trigger	0.0-3.1	0.0-2.0
ISR	0.8-1.1	0.5-1.0
QCD+EW NLO	0.5-5.4	2.2-14.0
Cross section ($W + \text{jets}$)	0.2-1.4	—
Cross section ($t\bar{t}$)	0.0-1.0	0.0-0.8
Closure tests		
α_T extrapolation	2.7-7.6	3.3-9.4
$\Delta\phi_{\min}^*$ extrapolation	2.1-20.0	2.7-22.0
W^+/W^- extrapolation	1.2-6.6	—

Table 4.9.: Summary of systematic uncertainties on the $T(\mu \rightarrow W/t\bar{t})$ and $T(\mu\mu \rightarrow Z)$ transfer factors, derived from variations of the data-to-simulation correction factors (Sec. 4.12.1) and data-driven closure tests (Sec. 4.12.2). The quoted ranges correspond to the $\pm 1\sigma$ quantiles of the transfer factor changes across all $(n_{\text{jet}}, n_b, H_T)$ bins.

4.12.1. Uncertainties derived from variations in simulation

The corrections to the simulation described in Sec. 4.9 have uncertainties associated with them based on the procedures in which they are derived. The effect of these uncertainties is considered both on the transfer factors, which provide the expected normalisation of the backgrounds in each $(n_{\text{jet}}, n_b, H_T)$ bin, and the modelling of the H_T distribution within each of these bins. This section focusses on the transfer factors, while the effect on the H_T shape is discussed in Sec. 4.12.3.

In order to determine systematic uncertainties on the transfer factors, the correction factors are varied in turn from their nominal values by one standard deviation up and down, according to their associated uncertainties. The number of simulated events in the signal and control regions is then re-computed under both variations, and the resulting changes in the transfer factors are taken as systematic uncertainties

on the transfer factors. This is done for both the $T(\mu \rightarrow W/t\bar{t})$ and $T(\mu\mu \rightarrow Z)$ transfer factors, in every $(n_{\text{jet}}, n_b, H_T)$ bin.

An example of this procedure is shown in Fig. 4.12, which shows the relative change of the transfer factors under variations of the pileup corrections. The effect on the transfer factors due to the other sources of systematic uncertainty is shown in App. A.1. The uncertainties associated with each set of simulation corrections will be discussed further in this section.

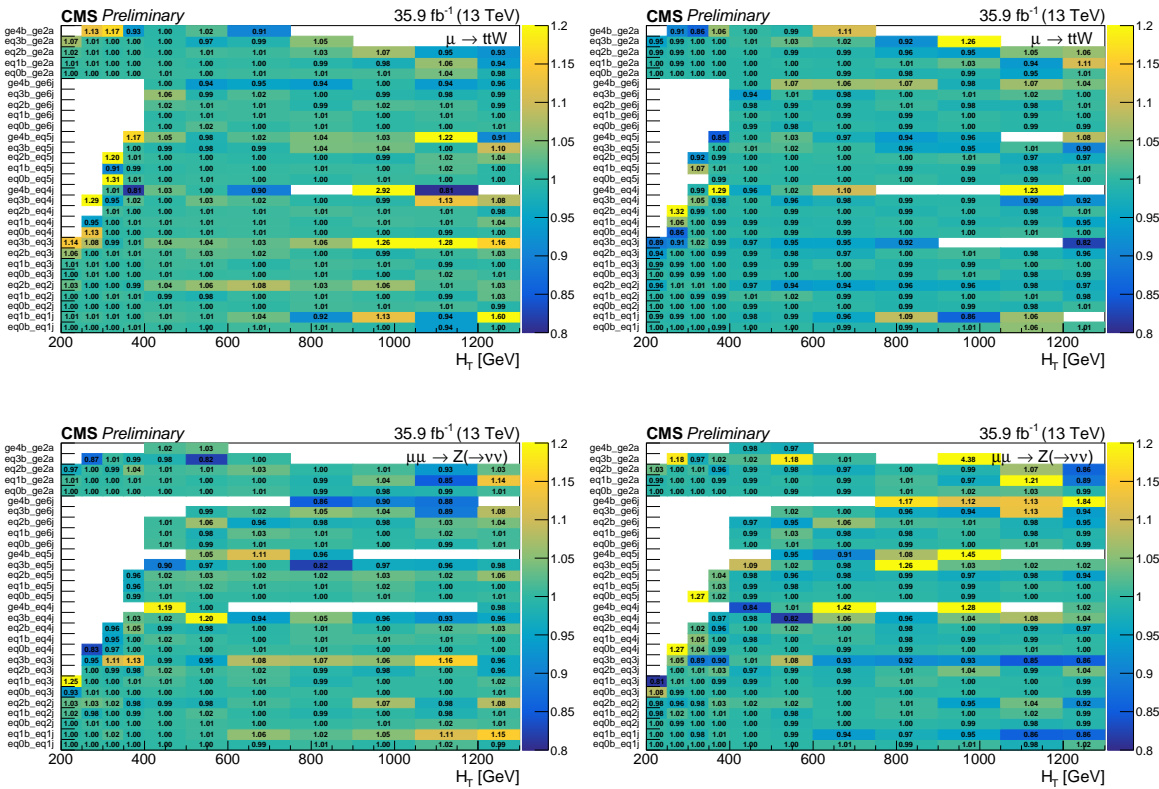


Figure 4.12.: The ratio of the $T(\mu \rightarrow W/t\bar{t})$ (top) and $T(\mu\mu \rightarrow Z)$ (bottom) transfer factors in each $(n_{\text{jet}}, n_b, H_T)$ bin when varying the pileup correction factors by $\pm 1\sigma$ (left) and $\pm 10\%$ (right) with respect to their nominal values.

The effect on the transfer factors is usually small, at the level of a few percent change in their value. This is because the kinematics and background composition in equivalent bins of the control and signal region are similar, and so the change of the simulation yields under each variation is also similar, which leads to an almost complete cancellation in the ratio of the transfer factor. The changes can be larger than 10% in certain bins of the search's parameter space that are statistically more limited.

Pileup

Events in the simulation are weighted to correct the pileup distribution as described in Sec. 4.9.1. The measured inelastic proton-proton cross section of 63 mb has an associated uncertainty of 5%. The pileup distribution in data is therefore also constructed using a cross section of 66.15 mb and 59.85 mb, and the pileup weights are re-derived for both variations.

The resulting changes in the transfer factors are typically in the range 0.5-4% across the $(n_{\text{jet}}, n_b, H_T)$ bins. This is shown in Fig. A.1

Jet energy

The energies of jets are corrected as a function of their transverse momentum and pseudorapidity as described in Secs. 3.3.5 and 4.9.2.

When varying the jet energy corrections in simulation by 1σ up and down, the values of the $T(\mu \rightarrow W/t\bar{t})$ and $T(\mu\mu \rightarrow Z)$ transfer factors are seen to change by approximately 3-8% across the $(n_{\text{jet}}, n_b, H_T)$ bins. This is shown in Fig. A.2.

b-tagging

Events in the simulation are weighted to correct for differences in the b-tagging efficiency and mistagging probability with respect to data, as described in Sec. 4.9.3. The measurements of the tagging probabilities for bottom and charm quarks are correlated, and so their uncertainties are varied in conjunction. The uncertainties on the correction factors for light flavour quarks are considered separately.

The changes in the values of the transfer factors under variations of the uncertainties on both the heavy and light flavour b-tagging probabilities are shown in Figs. A.3 and A.4. These are typically quite small, between 0-2%.

Lepton identification, isolation and triggering

The efficiencies of the identification, isolation and trigger requirements for muons and electrons are corrected using the tag-and-probe method discussed in Sec. 4.9.4.

The uncertainties associated with these correction factors are varied by $\pm 1\sigma$ in both the signal and control regions and the transfer factors are recomputed.

The changes of the transfer factors are found to be approximately 2% for $T(\mu\mu \rightarrow Z)$ and 5% for $T(\mu \rightarrow W/t\bar{t})$ across the (n_{jet} , n_b , H_T) parameter space. The change is larger in the latter case as the lepton efficiencies have an opposite effect in the signal region and the $\mu + \text{jets}$ control region. For instance, if the muon identification efficiency is increased, the number of events in the $\mu + \text{jets}$ control region increases while the number of $W/t\bar{t}$ events in the signal region decreases due to a more efficient vetoing of leptonic events. On the other hand, while the yields in the $\mu\mu + \text{jets}$ control region increase, the numerator of the $T(\mu\mu \rightarrow Z)$ transfer factor is unaffected as the lepton efficiency is irrelevant for the $Z(\rightarrow \nu\nu) + \text{jets}$ process.

Trigger

As mentioned in Sec. 4.9.5, simulated events in the signal region are corrected to account for the efficiency of the combined suite of $H_T\text{-}\alpha_T$, $E_T\text{-}\cancel{H}_T$, and pure H_T triggers. The nominal values of the correction factors are taken from the efficiencies measured with the electron reference sample. The differences with respect to the efficiencies measured with the muon reference sample are assigned as systematic uncertainties on the correction factors.

The differences are around 5% in the turn-on region ($\cancel{H}_T \approx 200$ GeV) and are practically zero in the efficiency plateau ($\cancel{H}_T > 300$ GeV). As these corrections are only relevant for events in the signal region and not in the control regions, the resulting changes of the transfer factors are also in this range, as shown in Fig. A.5.

Theoretical calculation of V+jets production

The $Z + \text{jets}$ and $W + \text{jets}$ simulation samples generated at leading order are corrected for NLO effects as a function of boson p_T , as discussed in Sec. 4.9.6. These correction factors are assigned a conservative uncertainty given by the difference of the correction from unity. This is defined such that a variation of -1σ is equivalent to not applying such corrections, and a $+1\sigma$ is equivalent to applying them twice.

The effect on the transfer factors is found to be small at low values of H_T . At high H_T , they can be smaller than the equivalent transfer factors without NLO

corrections by up to $\sim 10\%$, as seen in Fig. A.6. This is due to a larger Lorentz boost that is implicitly imposed on the bosons by the $\Delta\phi_{\min}^* > 0.5$ requirement in the signal region compared to the control regions in which such requirement is not made. Thus, because the NLO correction factors are decreasing with boson p_T , events in the signal region are typically subjected to slightly smaller corrections.

Initial state radiation in $t\bar{t}$ events

Uncertainties in the corrections derived to improve the distribution of the number of ISR jets, described in Sec. 4.9.7, are also considered. The correction factors are assigned an uncertainty given by half the difference of the correction from unity.

Although the uncertainties on the correction factors are relatively large, the effect on the transfer factors is small, at the level of 1%, as shown in Fig. A.7. This is expected as the signal and control regions are categorised identically in the number of jets, which leads to a cancellation in the transfer factors.

Cross sections

The cross sections of the main standard model background processes are corrected according to the H_T sideband method described in Sec. 4.9.8. Given a similar background composition between the signal and control regions, these are expected to have a small effect on the transfer factors. The $T(\mu \rightarrow W/t\bar{t})$ transfer factors are potentially most sensitive to uncertainties in the cross sections in bins in which there is a mixture of $W(\rightarrow \ell\nu) + \text{jets}$ and $t\bar{t}$ events, as the relative composition of each process may be different in the signal and control regions due to different kinematic selections on α_T , $\Delta\phi_{\min}^*$, and M_T . It is checked whether the transfer factors are indeed sensitive to this by varying the $W + \text{jets}$ and $t\bar{t}$ cross sections in turn by twice their uncertainties as measured by the CMS experiment. The changes in the transfer factors are then assigned as systematic uncertainties on their values.

The variations on the $T(\mu \rightarrow W/t\bar{t})$ transfer factors is shown in Figs. A.8 and A.9 as a function of $(n_{\text{jet}}, n_b, H_T)$. The changes are found to be relatively small, with values between 0-2%.

4.12.2. Uncertainties derived from data-driven closure tests

Further sources of systematic uncertainty on the transfer factors are considered in addition to those related to the data-to-simulation correction factors described in the previous section. The transfer factors may be biased as a result of different kinematic selections in the signal and control regions, as well as slightly different background compositions. The transfer factors are probed for potential bias via a series of *closure tests*, in which a control (sub-)region is used to estimate the number of events in another control (sub-)region rather than the signal region.

In an analogous way to the signal region background estimation (Eq. 4.23), the number of observed events in a control sub-sample A is used to estimate the number of events in a control sub-sample B via a transfer factor involving the corresponding event yields in simulation:

$$\hat{N}_B = \frac{N_B^{\text{sim}}}{N_A^{\text{sim}}} N_A^{\text{data}}. \quad (4.27)$$

The estimated number of events is then compared to the observed number of events in control sub-region B, and the level of closure (or rather, non-closure) is measured by the quantity:

$$C(A \rightarrow B) = \frac{N_B^{\text{data}} - \hat{N}_B}{\hat{N}_B}. \quad (4.28)$$

The deviation of this quantity from zero, with its uncertainty added in quadrature, is then assigned as a systematic uncertainty on the relevant transfer factor. The closure tests are performed, in turn, as a function of H_T and n_{jet} . The various closure tests employed to probe different sources of potential bias are discussed in this section.

To avoid double counting the uncertainties due to the simulation correction factors and thereby inflating the systematic uncertainties derived from the closure tests, the estimation in Eq. 4.27 is performed via a maximum likelihood fit, similar to the one that will be discussed in Sec. 5.3, in which the data-to-simulation correction factor uncertainties are included.

Extrapolation in the α_T and $\Delta\phi_{\min}^*$ requirements

Unlike in the signal region, no requirements are made on the α_T and $\Delta\phi_{\min}^*$ variables on events in the muon control regions. A mismodelling of these variables in the simulation may therefore introduce a bias in the transfer factors.

To test this, closure tests are performed in which events in the $\mu + \text{jets}$ control region with values of α_T ($\Delta\phi_{\min}^*$) below a certain threshold are used to estimate the number of events in the $\mu + \text{jets}$ control region with values of α_T ($\Delta\phi_{\min}^*$) larger than the same threshold. The thresholds are chosen according to the $\Delta\phi_{\min}^*$ and H_T -dependent α_T selections mentioned in Sec. 4.5. The test is performed in the $\mu + \text{jets}$ control region as it is statistically more powerful than the $\mu\mu + \text{jets}$ control region.

The results of these closure tests are shown in Fig. 4.13. The resulting systematic uncertainties are found to be in the range $\sim 3\text{-}10\%$. These uncertainties are assigned to both the $T(\mu \rightarrow W/\bar{t}\bar{t})$ and $T(\mu\mu \rightarrow Z)$ transfer factors.

Extrapolation in the W^+/W^- proportion

W bosons produced at a proton-proton collider are predominantly left-handed, with a polarisation fraction of up to 70% at large transverse momenta [68]. Owing to both the left-handed nature of the weak interaction and angular momentum conservation, this means that a leptonic W^+ decay results in a neutrino travelling in the same direction as the W boson and a lepton travelling in the opposite direction. In a W^- decay, the directions of the (anti-)neutrino and lepton are reversed. The neutrino (lepton) therefore has a larger Lorentz boost in a W^+ (W^-) decay than in a W^- (W^+) decay. As the acceptance of the $\mu + \text{jets}$ control region to W events relies more on the muon p_T , while the signal region relies more on the missing energy, this leads to a larger W^+/W^- fraction in the signal region than in the $\mu + \text{jets}$ control region.

To test whether this introduces a bias in the $T(\mu \rightarrow W/\bar{t}\bar{t})$ transfer factor, a closure test is performed within the $\mu + \text{jets}$ control region in which a sample of W^+ events is used to estimate the number of W^- events. The results of this closure test are shown in Fig. 4.13. The level of closure and the resulting systematic uncertainties assigned to the $T(\mu \rightarrow W/\bar{t}\bar{t})$ transfer factor are around $\sim 1\text{-}5\%$.

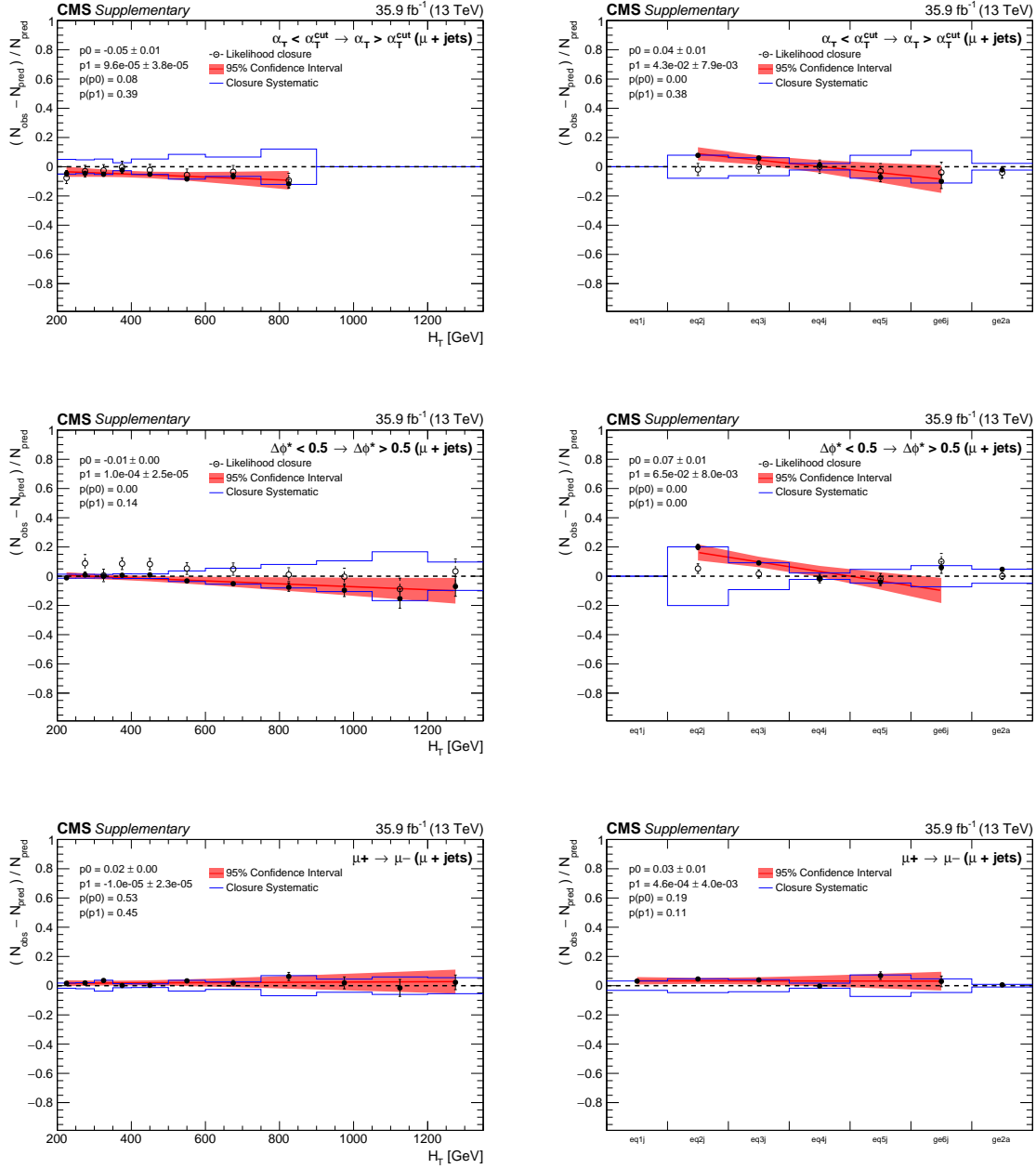


Figure 4.13.: Closure tests relating to extrapolations in α_T (top), $\Delta\phi^*$ (middle), and W boson polarisation (bottom), as a function of H_T (left) and n_{jet} (right). The level of closure obtained via a maximum likelihood method is indicated by the open circles. The blue lines represent the resulting systematic uncertainties that are assigned to the relevant transfer factors. A linear fit is also shown.

4.12.3. Uncertainties on the H_T distribution

The expected distribution of electroweak background events in the H_T variable is taken directly from the simulation, as described in Sec. 4.10.2. This was validated by checking that the ratio of the normalised distribution between data and simulation in the muon control regions is statistically compatible with unity. Specifically, the best-fit value of a linear parameter is checked to be consistent with zero across all $(n_{\text{jet}}, n_b, H_T)$ bins in each of the $\mu + \text{jets}$ and $\mu\mu + \text{jets}$ control regions.

A systematic uncertainty is assigned to the H_T distribution obtained from simulation, also referred to as the nominal H_T distribution or shape, to account for uncertainties in the simulation modelling. The value of the fitted linear parameter, together with its uncertainty added in quadrature, is used to vary the nominal H_T shape and derive two alternative distributions. These are then encoded in the statistical model of the search as $\pm 1\sigma$ systematic uncertainties, as will be described in Sec. 5.3. The uncertainties derived from the $\mu + \text{jets}$ control region are assigned to the H_T distribution of the $W/t\bar{t}$ background process, while those derived from the $\mu\mu + \text{jets}$ control region are assigned to the $Z(\rightarrow \nu\nu) + \text{jets}$ process.

The alternative H_T shapes typically result in an uncertainty on the number of background events in the final H_T bin within each $(n_{\text{jet}}, n_b, H_T)$ category that is in the range 5-20%.

In addition to the uncertainties derived from the linear fit to the data-to-simulation ratio, all of the sources of systematic uncertainty associated with the simulation correction factors described in Sec. 4.9 and applied to the transfer factors in Sec. 4.12.1 are also considered for the H_T modelling. This is done by varying each uncertainty in turn by $\pm 1\sigma$ and deriving further alternative H_T distributions (two for each source of uncertainty). In general, these uncertainties are sub-dominant compared to those derived from the linear fit.

Chapter 5.

Results and interpretation

In this chapter, the kinematic properties of the simplified models of long-lived gluino production with final states consisting of (displaced) jets and missing energy are presented. The statistical model used to perform the background estimation and analyse the observed 35.9 fb^{-1} of data is discussed. No significant discrepancy is found between the data and the standard model expectation. Upper limits are placed at a 95% confidence level on the cross sections of both the prompt and long-lived SUSY simplified models described in Sec. 2.5.

5.1. Characterisation of long-lived gluino models

The expected binned event yields for six representative simplified models of split supersymmetry are shown in Fig. 5.1, along with the expected standard model background (as determined using the method described in Sec. 5.4). An aggregated version of the nominal binning scheme (Sec. 4.6) is used for ease of presentation. The example models consist of a short ($c\tau = 1 \mu\text{m}$), medium ($c\tau = 1 \text{ mm}$) and long ($c\tau = 100 \text{ m}$) lifetime gluino, with both a compressed ($m_{\tilde{g}} - m_{\tilde{\chi}_1^0} = 100 \text{ GeV}$) and uncompressed mass spectrum.

For models with a compressed mass spectrum, the displaced jets originating from the decay of the gluino are produced with relatively low transverse momenta and tend to be below the 40 GeV threshold. The acceptance for these models relies on jets from initial state radiation. The events therefore populate the low n_{jet} and low H_{T} region of the parameter space of the search. This behaviour is independent of the lifetime of the gluino.

For models with an uncompressed mass spectrum, the displaced jets from the gluino decay are hard enough to be observed. Models with a promptly decaying gluino (given the detector’s resolution, a decay length of $1\text{ }\mu\text{m}$ is considered prompt-like) populate the higher n_{jet} and H_{T} categories. The jet reconstruction efficiency decreases as the decay length of the gluino increases. For decays occurring within the tracker ($10\text{ cm} \lesssim c\tau \lesssim 1\text{ m}$) fewer hits are available for the reconstruction. Decays occurring within the calorimeters ($1\text{ m} \lesssim c\tau \lesssim 10\text{ m}$) result in jets containing no charged tracks, and may therefore result in the event being vetoed by the jet quality criteria described in Sec. 4.2. Jets produced within the muon chambers and outside the detector ($c\tau \gtrsim 10\text{ m}$) cannot be reconstructed. With increasing lifetime, the behaviour of the uncompressed models therefore tends towards that of the compressed models. Finally, displaced jets in uncompressed models with $c\tau \sim 1\text{ mm}$ exhibit similar characteristics as bottom quark jets, and are often tagged by the b-tagging algorithm. These events therefore populate the high n_{b} categories, with potentially up to four b-tagged jets.

5.2. Uncertainties on signal model simulation

The expected number of signal events is estimated using simulation. The various data-to-simulation correction factors discussed in Sec. 4.9 are applied. The uncertainties in each $(n_{\text{jet}}, n_{\text{b}}, H_{\text{T}}, \cancel{H}_{\text{T}})$ bin are derived by varying the corrections within their uncertainties and recomputing the simulated yields, analogously to the uncertainties on the background processes (Sec. 4.12.3). This includes uncertainties due to the corrections on the jet energy, pileup distribution, b-tagging efficiency, trigger efficiency, and ISR distribution. The integrated luminosity of 35.9 fb^{-1} is measured with an uncertainty of 2.5% [69] which results in an additional uncertainty on the overall number of signal events. The statical uncertainties due to the limited number of simulated events are also considered. Additional sources of uncertainty related to displaced jets are discussed in the remainder of this section. A summary of all sources of uncertainty and their typical sizes is shown in Tab. 5.1 for various representative simplified models of long-lived gluino production.

The requirement of $f_{\text{CH}} < 0.1$ on the most energetic jet of the event, discussed in Sec. 4.2, reduces the selection efficiency for T1qqqqLL models with $1\text{ m} \lesssim c\tau \lesssim 10\text{ m}$ to $\sim 30\%$. This is because of the lack of reconstructed charged particle tracks

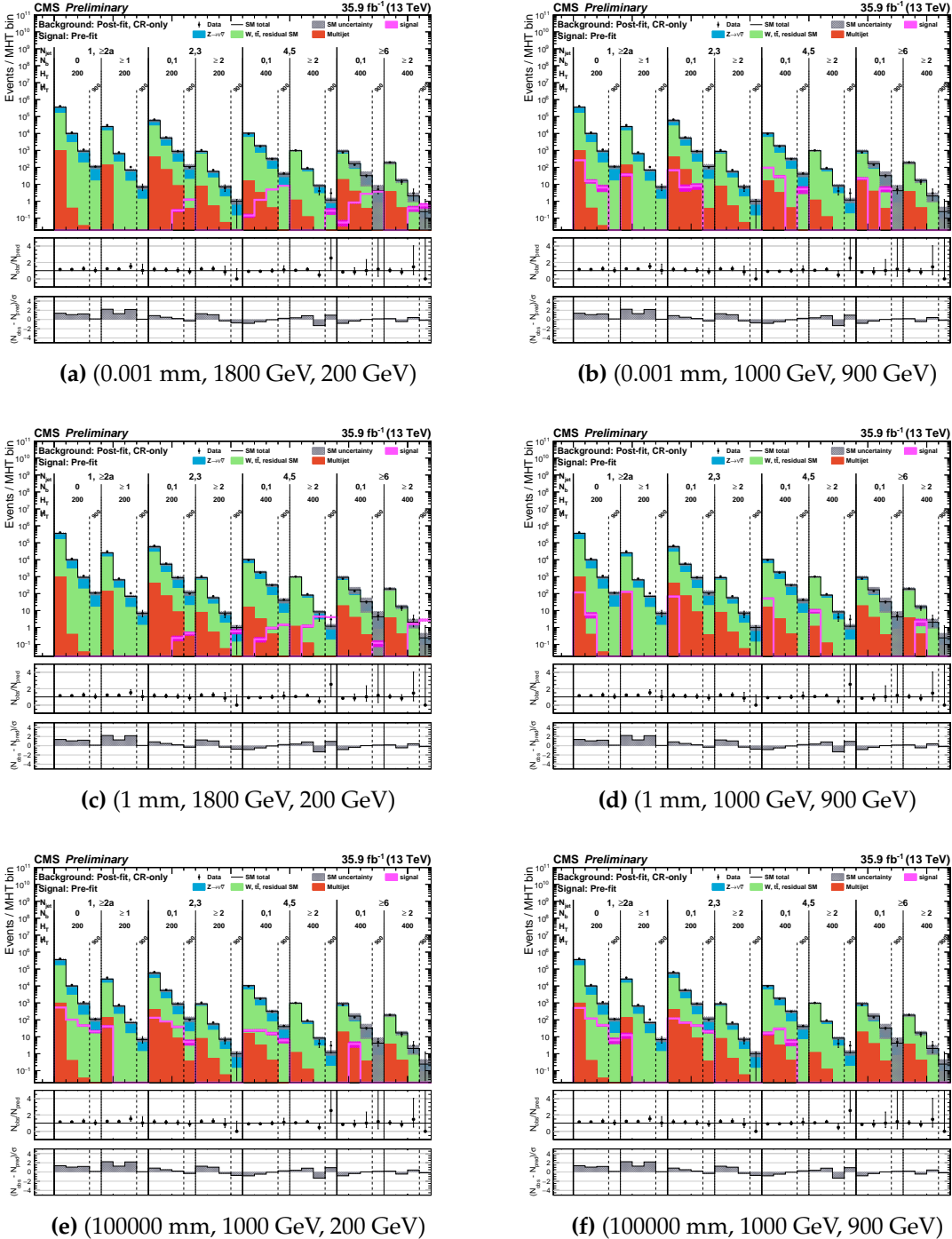


Figure 5.1.: Expected signal events for split SUSY simplified models with a range of values of $(c\tau, m_{\tilde{g}}, m_{\tilde{\chi}_1^0})$, overlaid on the expected standard model background counts, using an aggregated binning scheme.

in the displaced jets that are produced inside the calorimeters. For the same reason, the veto on events containing a jet that fails the identification requirements

Source of uncertainty	$c\tau = 1 \mu\text{m}$		$c\tau = 1 \text{ mm}$		$c\tau = 10 \text{ m}$	
	(1800,200)	(1000,900)	(1800,200)	(1000,900)	(1000,200)	(1000,900)
Pileup	1-3	1-3	2-4	1-4	1-5	1-5
Jet energy	3-9	4-14	3-9	4-17	4-9	2-12
b-tagging	0-1	0-1	17-59	10-41	0-1	0-1
Trigger	3-4	0-2	2-4	0-2	0-4	0-1
ISR	3-5	2-10	2-5	2-9	2-14	3-14
Luminosity	2.5	2.5	2.5	2.5	2.5	2.5
Stat.	8-20	15-21	11-20	17-26	16-22	14-26

Table 5.1.: Summary of uncertainties (%) on the simplified long-lived gluino models for various values of $(m_{\tilde{g}}, m_{\tilde{\chi}_1^0})$ [GeV]. The quoted ranges correspond to the $\pm 1\sigma$ quantiles of the yield changes across all $(n_{\text{jet}}, n_b, H_T, \mathcal{H}_T)$ bins.

(which includes a minimum requirement on the charged component of jets), has a selection efficiency of $\sim 10\%$ for these models. Below and above this range in $c\tau$ the efficiencies of the jet identification and f_{CH} requirements are close to 100%. To account for a potential mismodelling of the simulation in the variables used for jet identification, the efficiency of these event selections are computed as a function of the decay lengths and pseudorapidities of the long-lived gluinos, and the sizes of the inefficiencies are propagated as a systematic uncertainty on the expected signal counts.

Jet identification requirements are also present in the trigger logic. The inefficiency of the trigger is measured to be at most 2% for events with gluinos decaying within the calorimeter region. This is applied as a correction to the simulation, as a function of decay length and pseudorapidity, and an appropriate systematic uncertainty is assigned.

As seen in the previous section, jets with a displacement of $\sim 1 \text{ mm}$ can be tagged by the b-tagging algorithm. This is because they have similar displacements as b-quarks. The b-tagging efficiency for displaced jets is measured as a function of the displacement d with respect to the primary vertex, in bins of p_T and η , and compared to the efficiency for standard model quarks. An example of this is shown in Fig. 5.2. Three regions are identified as $d < 0.1 \text{ mm}$ (small displacements), $d > 10 \text{ mm}$ (large displacements), and $0.1 < d < 10 \text{ mm}$ (“b-like” displacements). In the $0.1 < d < 10 \text{ mm}$ region, the b-tagging efficiency for displaced jets is approximately 60%, almost comparable to that for b-quarks ($\sim 80\%$). The nominal b-tagging correction factors and uncertainties (described in Sec. 4.9.3) are applied in

the simulation to jets with this range of displacements, together with an additional uncertainty of size 20-50% to cover differences in the efficiencies with respect to jets originating from b-quarks. For displacements of $d < 0.1$ mm and $d > 10$ mm, the efficiency falls to 1-5%, similar to that of light quarks. A conservative 100% uncertainty on the efficiency is taken in these regions.

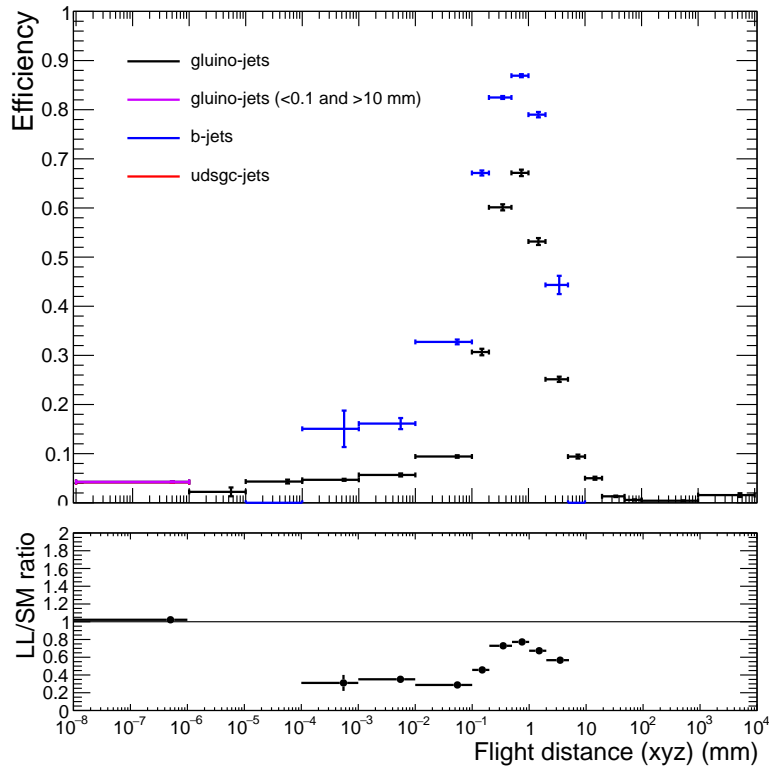


Figure 5.2.: Efficiency of the b-tagging algorithm for displaced jets originating from long-lived gluinos, compared to standard model bottom and light quarks, for jets with $100 < p_T < 140$ and $0 < |\eta| < 0.5$.

5.3. Statistical model

In order to perform a statistical analysis of the results obtained, a likelihood function is used to model the background and signal events across the (n_{jet} , n_b , H_T , \mathcal{H}_T) parameter space in the signal and control regions, accounting for all relevant uncertainties. The likelihood function is utilised to carry out the background estimation as well as to perform hypothesis tests to assess the sensitivity of the search to new physics.

The number of events in each bin of the $(n_{\text{jet}}, n_b, H_T, \mathcal{H}_T)$ parameter space is modelled as a Poisson distribution, with an expected value given by that obtained from simulation, multiplied by *modifier* terms that account for the transfer factors and relevant uncertainties. The uncertainties are encoded as *nuisance parameters* with probability densities and correlations that will be discussed in this section.

The component of the likelihood function related to the $(n_{\text{jet}}, n_b, H_T)$ bin k in the signal region is given by:

$$\mathcal{L}_{\text{sig}}^k = \prod_j \mathcal{P} \left(n_{\text{sig}}^{k,j} \middle| \sum_i (b_{Z,\text{sig}}^{i,j} r_Z^i \theta_{Z,\text{sig}}^{i,j} + b_{W,\text{sig}}^{i,j} r_W^i \theta_{W,\text{sig}}^{i,j} + b_{\text{QCD,sig}}^{i,j} \theta_{\text{QCD,sig}}^{i,j} + \mu_s s_{\text{sig}}^{i,j} \theta_{s,\text{sig}}^{i,j}) \right), \quad (5.1)$$

where the product is over all \mathcal{H}_T bins within the $(n_{\text{jet}}, n_b, H_T)$ bin, $n_{\text{sig}}^{k,j}$ is the number of events observed in data in a given $(n_{\text{jet}}, n_b, H_T, \mathcal{H}_T)$ bin, the summation is over all fine $(n_{\text{jet}}, n_b, H_T)$ bins i that form part of the given coarse H_T bin (Sec. 4.6), $b_{Z,\text{sig}}^{i,j}$ and $b_{W,\text{sig}}^{i,j}$ are the number of $Z(\rightarrow \nu\nu) + \text{jets}$ and $W/\bar{t}\bar{t}$ events expected based on simulation, r_Z^i and r_W^i are the control region based data-to-simulation correction ratios in the transfer factor equations (Eq. 4.25), $\theta_{Z,\text{sig}}^{i,j}$ and $\theta_{W,\text{sig}}^{i,j}$ encapsulate all relevant uncertainties related to the transfer factors (both from the data-driven closure tests and the variations in simulation), the \mathcal{H}_T shape, and the limited number of simulated events, $b_{\text{QCD},\mu}^i$ is the number of QCD events estimated using the method described in Sec. 4.11 with $\theta_{\text{QCD,sig}}^{i,j}$ encoding its uncertainty, $s_{\text{sig}}^{i,j}$ is the expected number of signal events based on simulation with $\theta_{s,\mu}^i$ encapsulating its uncertainties, and $\mu_s = \frac{\sigma}{\sigma_{\text{th}}}$ is a signal strength parameter that scales the signal model's cross section with respect to its theoretical value and is relevant when setting limits (Sec. 5.5).

The component of the likelihood function related to the $(n_{\text{jet}}, n_b, H_T)$ bin i in the $\mu + \text{jets}$ control region is given by:

$$\mathcal{L}_\mu^i = \mathcal{P} \left(n_\mu^i \middle| b_\mu^i r_W^i \theta_{b,\mu}^i + b_{\text{QCD},\mu}^i + \mu_s s_\mu^i \theta_{s,\mu}^i \right), \quad (5.2)$$

in which the small potential contributions from QCD and signal events are accounted for based on the simulation. The signal contamination is only non-negligible for SUSY models containing top and bottom quarks. Similarly, the

likelihood in the $\mu\mu + \text{jets}$ control region is written as:

$$\mathcal{L}_{\mu\mu}^i = \mathcal{P} \left(n_{\mu\mu}^i \middle| b_{\mu\mu}^i r_Z^i \theta_{b,\mu\mu}^i + b_{\text{QCD},\mu\mu}^i + \mu_s s_{\mu\mu}^i \theta_{s,\mu\mu}^i \right). \quad (5.3)$$

The correction parameters r_Z^i and r_W^i are shared between the signal region and relevant control region. These parameters are unconstrained (they are modelled by a uniform distribution) and therefore allow the background estimations to be made when maximising the likelihood function over the control regions.

Each source of uncertainty (described in Sec. 4.12) results in an uncertainty on the expected number of events of a given process in each bin of the search. The correlations of the uncertainties between bins are included in the likelihood function and, for simplicity, are chosen to be either 0 (uncorrelated) or 1 (perfectly correlated). As a simple example, a correlation of 1 between two bins, each with a (different) expected number of event counts and associated uncertainty, means that if the counts in one bin are increased by one standard deviation, the counts in the other bin also increase by one standard deviation. This is implemented in the likelihood model such that bins that are assumed to be fully correlated share the same nuisance parameter, whereas bins that are uncorrelated have independent nuisance parameters.

The nuisance parameters representing the systematic uncertainties derived from the data-driven closure tests (Sec. 4.12.2) are modelled as a log-normal distribution. As these are derived in turn as a function of n_{jet} and H_T , integrated over the other dimensions, and are statistical in nature, two sets of nuisance parameters are included that are considered to be correlated across the n_b , H_T and \mathcal{H}_T (n_{jet} , n_b and \mathcal{H}_T) dimensions and uncorrelated in n_{jet} (H_T).

The systematic uncertainties derived on the \mathcal{H}_T shape (Sec. 4.12.3) are incorporated as $\pm 1\sigma$ alternative \mathcal{H}_T distributions. The event yields in each bin of the distributions are interpolated quadratically between the alternative shapes and extrapolated linearly beyond this. This “morphing” procedure is controlled by a Gaussian nuisance parameter, and is described in Ref. [70]. Uncertainties on the \mathcal{H}_T distributions are derived by performing the linear fits described in Sec. 4.12.3 integrating over H_T and n_{jet} in turn. This results in two sets of uncertainties that are correlated in H_T and n_{jet} , respectively, and are derived for each of the $Z(\rightarrow \nu\nu) + \text{jets}$ (from the $\mu\mu$

$\mu + \text{jets}$ control region fit) and $W(\rightarrow \ell\nu) + \text{jets}$ (from the $\mu + \text{jets}$ control region fit) processes.

Similarly, the systematic uncertainties derived from variations of the data-to-simulation correction factors (Sec. 4.12.1) are also incorporated as alternative H_T distributions in the signal region. In this case, these may also change the H_T normalisation and therefore affect the transfer factors. In the control regions there is effectively no H_T shape as they are not binned in this variable. Each of these uncertainties is assumed to originate from a unique underlying source, and so they are treated as being fully correlated across the full parameter space of the signal and control regions. In other words, there is only one nuisance parameter for each source of uncertainty that is shared among all bins and processes.

The statistical uncertainties due to the limited number of simulated events are modelled as a Gaussian distribution in each bin, and are uncorrelated across bins. Finally, the QCD estimate in the signal region is assigned a conservative 100% uncertainty, modelled as a log-normal distribution, that is uncorrelated across n_{jet} and H_T and correlated across n_b and H_T .

The probability densities of the nuisance parameters are encoded within the likelihood function $\mathcal{L}_{\text{nuis}}$. The total likelihood for all bins in the signal and control regions and their uncertainties is then given by the product:

$$\mathcal{L} = \mathcal{L}_{\text{nuis}} \prod_k \mathcal{L}_{\text{sig}}^k \prod_i \mathcal{L}_\mu^i \prod_i \mathcal{L}_{\mu\mu}^i \quad (5.4)$$

5.4. Comparison of expected background and observed data

As will be discussed in Sec. 5.5, the sensitivity of the search is assessed by comparing the values of the maximised likelihood function under the background-only hypothesis ($\mu_s = 0$) and the background-plus-signal hypothesis ($\mu_s \neq 0$). First, it is instructive to compare the observed event counts in data with those expected from the standard model. The expected standard model background is obtained by performing the maximum likelihood fit under the background-only hypothesis to the control regions only (i.e. the signal region is excluded). This is essentially

equivalent to the application of the transfer factor equations (Sec. 4.10), accounting for uncertainties.

The results of this fit are shown in Figs. 5.3 and 5.4. These show the observed number of events in data and the expected number of Z , $W/t\bar{t}$ and QCD background events in every $(n_{\text{jet}}, n_b, H_T, \cancel{H}_T)$ bin of the signal region. The uncertainties on the background expectation include both the systematic and statistical components added in quadrature. Also shown are the ratios in each bin between the observed and expected number of events, and the z-scores (the difference between observed and expected counts, divided by the uncertainty on the expected counts). The ratios and z-scores, integrated over \cancel{H}_T , are also summarised in Fig. 5.5. The observed and expected event counts are also summarised in tabulated form in App. B.1.

Overall, no statistically significant excess is observed in the data. The z-scores are found to be centred on zero, with almost all bins having values within $\pm 2\sigma$. Similarly, the ratios of observed and expected counts are consistent with unity.

A likelihood fit is also performed under the background-only hypothesis to the full control and signal region parameter space. The results of this are shown in App B.2. Again, the binned observed number of events is found to be consistent, within uncertainties, with those expected from the standard model. The best fit values of the nuisance parameters are shown in App. B.3 and can be seen to be within their $\pm 1\sigma$ values.

5.5. Procedure for setting limits on signal models

Given the good agreement between the observed data and the standard model expectation, with no significant excess above the number of expected events in any bin, no evidence of new physics beyond the standard model is found. Statistical hypothesis tests are carried out in order to assess the incompatibility of the data with various models of both prompt and long-lived supersymmetry. Upper bounds are placed on their cross sections at a 95% confidence level.

In the hypothesis tests, the parameter being tested is the signal strength, while all other parameters are considered to be nuisance parameters, labelled collectively as θ . For a test of a model with a signal strength of μ_s , one can use a profile likelihood

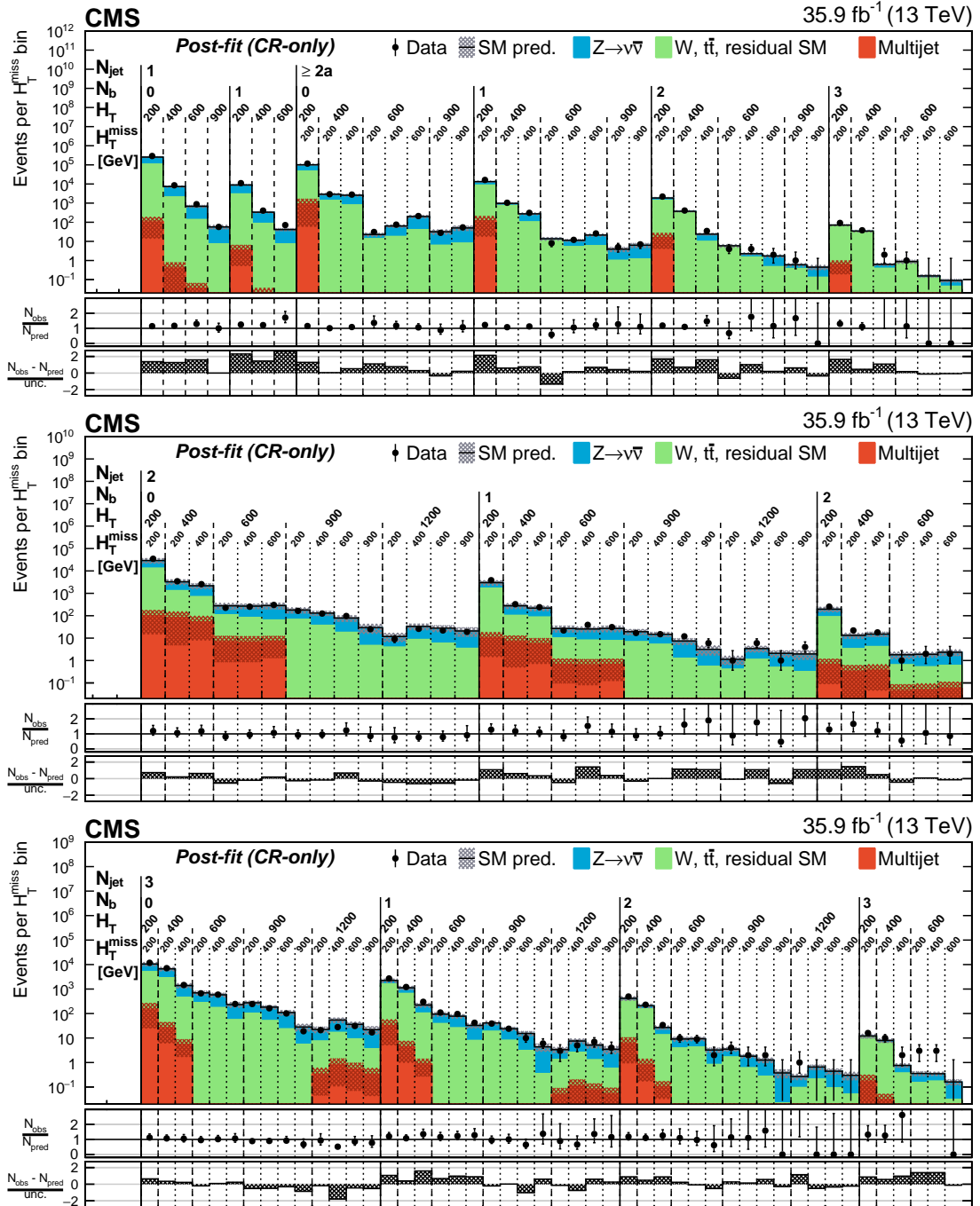


Figure 5.3.: Number of events observed (solid markers) and expected number of Z , $W/t\bar{t}$ and QCD background events (histograms, with shaded bands representing the statistical and systematic uncertainties) in every n_b , H_T and \cancel{H}_T bin of the jet categories $n_{\text{jet}} = 1$, $\geq 2a$ (top), $n_{\text{jet}} = 2$ (middle), and $n_{\text{jet}} = 3$ (bottom), as determined from the maximum likelihood fit to the control regions. The centre panel of each sub-figure shows the ratios of the observed and expected counts, while the lower panel shows the corresponding z-score, as defined in the text.

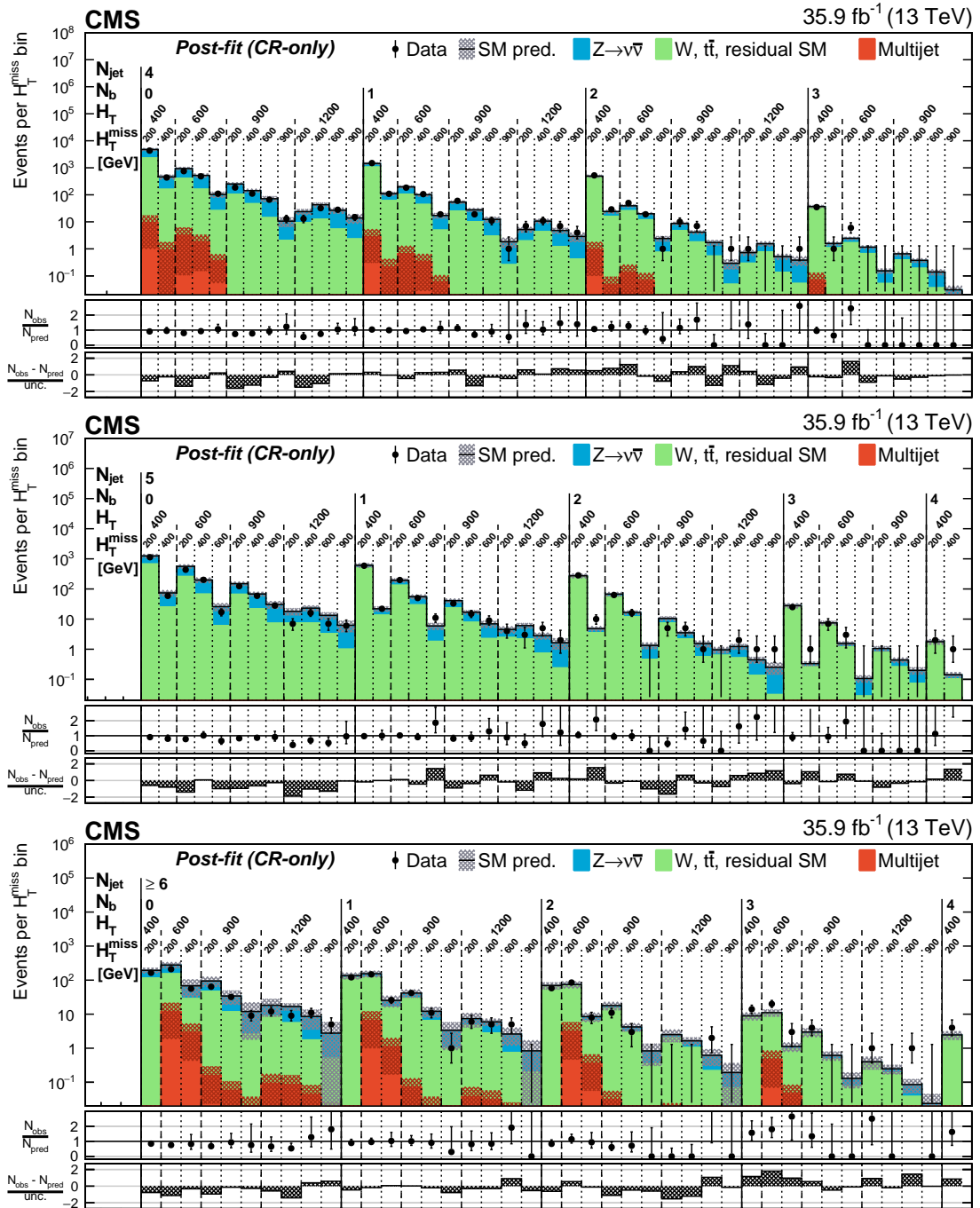


Figure 5.4.: Number of events observed (solid markers) and expected number of Z , $W/t\bar{t}$ and QCD background events (histograms, with shaded bands representing the statistical and systematic uncertainties) in every n_b , H_T and \cancel{H}_T bin of the jet categories $n_{\text{jet}} = 4$ (top), $n_{\text{jet}} = 5$ (middle), and $n_{\text{jet}} \geq 6$ (bottom), as determined from the background-only maximum likelihood fit to the control regions. The centre panel of each sub-figure shows the ratios of the observed and expected counts, while the lower panel shows the corresponding z-score, as defined in the text.

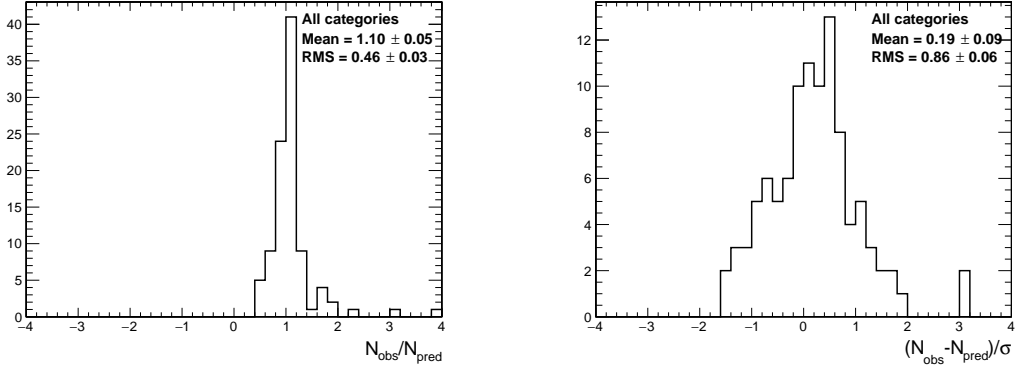


Figure 5.5.: Histograms of the ratios of the observed and expected event counts (left) and corresponding z-scores (right), as defined in the text, for all (n_{jet} , n_b , H_T) bins, as determined from the background-only maximum likelihood fit to the control regions.

ratio as a test statistic:

$$t(\mu_s) = 2 \ln \frac{\mathcal{L}(\hat{\mu}_s, \hat{\theta})}{\mathcal{L}(\mu_s, \hat{\theta}(\mu_s))} \quad (5.5)$$

where $\hat{\mu}_s$ and $\hat{\theta}$ are the global maximum likelihood values of the signal strength and nuisance parameters, and $\hat{\theta}(\mu_s)$ is the maximum likelihood value of the nuisance parameters for a fixed signal strength of μ_s . A value of $t(\mu_s) = 0$ represents a perfect agreement between the hypothesised signal strength μ_s and the observed data, while larger values of $t(\mu_s)$ represent an increasing incompatibility between μ_s and the data.

The best fit value of the signal strength is constrained to lie within $0 \leq \hat{\mu}_s \leq \mu_s$. The lower constraint is imposed so as to avoid a non-physical cross section. The upper bound is chosen so that an upward fluctuation in the signal counts such that $\hat{\mu}_s > \mu_s$ is not treated as evidence against that model. The final test statistic is then given by [71]:

$$t(\mu_s) = \begin{cases} 2 \ln \frac{\mathcal{L}(0, \hat{\theta}(0))}{\mathcal{L}(\mu_s, \hat{\theta}(\mu_s))} & \hat{\mu}_s < 0 \\ 2 \ln \frac{\mathcal{L}(\hat{\mu}_s, \hat{\theta})}{\mathcal{L}(\mu_s, \hat{\theta}(\mu_s))} & 0 \leq \hat{\mu}_s \leq \mu_s \\ 0 & \hat{\mu}_s > \mu_s \end{cases} \quad (5.6)$$

The incompatibility of a signal model with data can be assessed with the p-value:

$$\text{CL}_{b+s}(\mu_s) = \int_{t(\mu_s)_{\text{obs}}}^{\infty} f(t(\mu_s)|\mu_s) dt(\mu_s) \quad (5.7)$$

where $f(t(\mu_s)|\mu_s)$ is the probability density of the test statistic under the hypothesised signal strength μ_s , and $t(\mu_s)_{\text{obs}}$ is the value of the test statistic observed in data. In order to reject a signal model, not only is a small p-value CL_{b+s} required, but also a good compatibility with the background-only model, as determined by the probability:

$$\text{CL}_b(\mu_s) = \int_{t(\mu_s)_{\text{obs}}}^{\infty} f(t(\mu_s)|0) dt(\mu_s) \quad (5.8)$$

where $f(t(\mu_s)|0)$ is the probability density of the test statistic under the background-only model ($\mu_s = 0$). The ratio of the two probabilities is then constructed as [72,73]:

$$\text{CL}_s(\mu_s) = \frac{\text{CL}_{b+s}(\mu_s)}{\text{CL}_b(\mu_s)} \quad (5.9)$$

A particular signal strength is considered to be excluded at a 95% confidence level if the corresponding CL_s value is less than 0.05. For a given signal model, the upper limit on the signal strength $\mu_s^{95\%}$ is given by the largest value of μ_s that is excluded with $\text{CL}_s < 0.05$.

The distributions $f(t(\mu_s)|\mu_s)$ and $f(t(\mu_s)|0)$ are approximated by analytical probability functions that are derived in the limit of a large sample of events [74]. While the above procedure provides the *observed* limit on the signal strength, an *expected* limit can also be computed as the median value of $\mu_s^{95\%}$ obtained under the background-only model. The uncertainty on the expected limit is given by the appropriate quantiles of the distribution of $\mu_s^{95\%}$.

Simplified models of supersymmetry are simulated with a range of gluino/squark and LSP masses, and for a range of gluino lifetimes in the case of T1qqqqLL. An upper limit on the signal strength (and cross section) of each mass point is computed. The excluded region in the mass parameter space corresponds to mass points with limits on their signal strength of $\mu_s^{95\%} < 1$.

Model family	Best mass limit [GeV]	
	Gluino or squark	$\tilde{\chi}_1^0$
T2bb	1050	500
T2tt	1000	400
T2cc	500	475
T2qq_8fold	1325	575
T2qq_1fold	675	350
T1bbbb	1900	1150
T1tttt	1650	850
T1qqqq	1650	900
T1qqqqLL (metastable)	900	900
T1qqqqLL ($c\tau = 1$ mm)	1750	1000

Table 5.2.: Summary of the observed largest excluded mass at 95% confidence level for the parent SUSY particle (gluino or squark) and the LSP ($\tilde{\chi}_1^0$), for each family of simplified models.

5.6. Limits on supersymmetry with prompt decays

Figure 5.6 shows the excluded regions for the various simplified model families involving the production and prompt decay of squarks (T2 models) and gluinos (T1 models). Both the expected and observed limits are shown.

Squark masses up to 1050, 1000 and 1325 GeV are excluded for bottom, top and mass-degenerate light-flavour squarks, respectively. The corresponding lower bounds on the LSP mass from squark decays are 500, 400 and 575 GeV. Gluino masses up to 1900, 1650 and 1650 GeV are excluded for gluino decays via virtual bottom, top and light-flavour squarks. The corresponding largest exclusions on the LSP mass are 1150, 850 and 900 GeV.

The largest excluded masses (according to the observed limits) of squarks, gluinos and neutralinos are summarised in Tab. 5.2 for the prompt SUSY models, as well as some of the long-lived SUSY models that will be discussed in the next section.

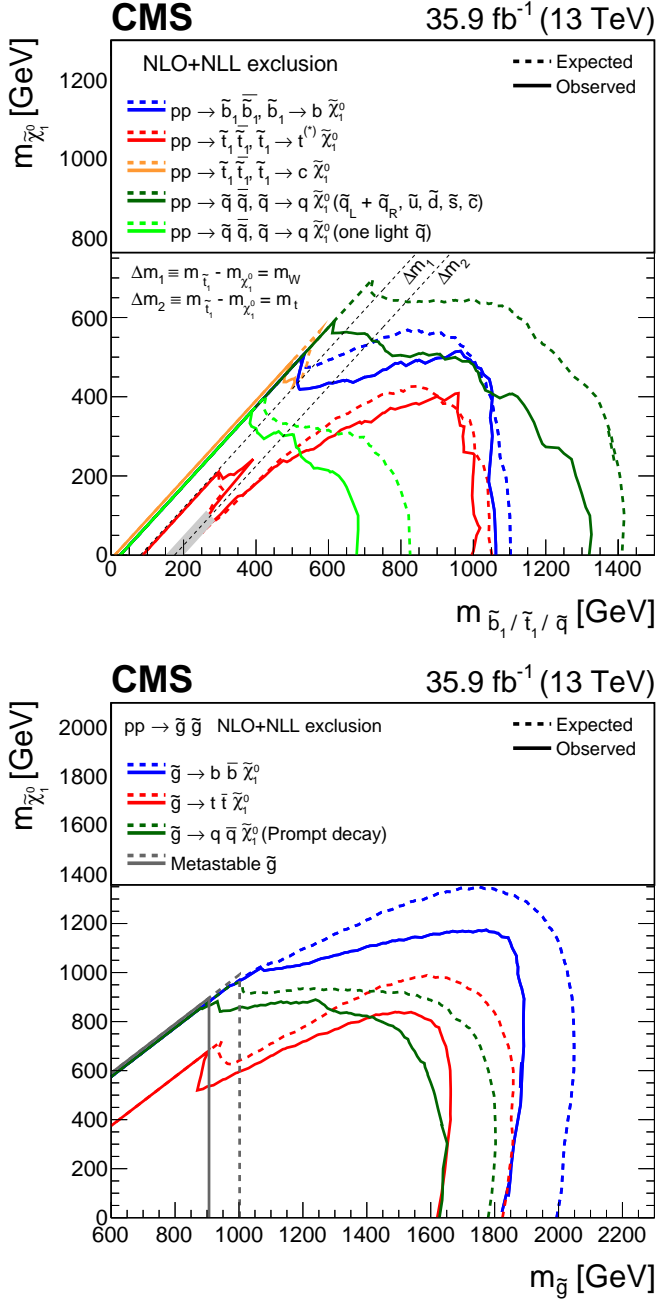


Figure 5.6.: Observed and expected mass exclusions at 95% confidence level (indicated by solid and dashed contours, respectively) for various families of simplified models. The upper subfigure summarises the mass exclusions for five model families that involve the direct pair production of squarks (T2bb, T2tt, T2cc, T2qq_8fold and T2qq_1fold). The grey shaded region denotes T2tt models that are not considered for interpretation. The lower subfigure includes three models that involve the production and prompt decay of gluino pairs (T1bbbb, T1tttt, and T1qqqq). A final scenario involves the production of gluinos that are assumed to be metastable on the detector scale (T1qqqqLL).

5.7. Limits on long-lived supersymmetry

Simplified models of split SUSY (T1qqqqLL) are simulated with a range of gluino and LSP masses for various gluino lifetimes from $c\tau = 1 \mu\text{m}$ to 100 m, in addition to a promptly decaying and metastable gluino. The prompt decay scenario is equivalent to the T1qqqq model. The limits are presented in the $(m_{\tilde{g}}, m_{\tilde{\chi}_1^0})$ plane for each simulated value of $c\tau$ in Figs. 5.7-5.9. Both the expected and observed exclusion regions are shown, with experimental uncertainties and uncertainties on the theoretical cross sections indicated. The excluded mass regions for each value of $c\tau$ are summarised in Fig. 5.10. Finally, the limits in the $(m_{\tilde{g}}, c\tau)$ plane, for fixed $m_{\tilde{\chi}_1^0} = 100 \text{ GeV}$ and for $m_{\tilde{g}} - m_{\tilde{\chi}_1^0} = 100 \text{ GeV}$, are shown in Fig. 5.11.

For the model with a promptly decaying gluino, gluino and LSP masses of up to $\sim 1650 \text{ GeV}$ and $\sim 900 \text{ GeV}$, respectively, are excluded, as seen in the previous section for T1qqqq. The excluded regions for models with gluino lifetimes of $c\tau = 1, 10, 100 \mu\text{m}$ are comparable to the prompt decay scenario. A moderate improvement in sensitivity is found for models with $c\tau = 1$ and 10 mm, with maximum excluded gluino and LSP masses of 1750 GeV and 1000 GeV, respectively. This is because these signal events occupy the high n_b categories, and the amount of background is considerably smaller than in the bins with no b-tagged jets. The sensitivity is reduced for models with lifetimes larger than $c\tau > 100 \text{ mm}$ as the acceptance to jets from the gluino decay becomes smaller. The limiting case is that of a metastable gluino. In this case, the gluinos always decay outside of the detector and so the acceptance for these models relies entirely on ISR jets. Gluino masses up to 900 GeV are excluded, and the sensitivity is independent of the LSP mass.

The observed exclusion regions are found to be $\sim 1\text{-}2\sigma$ weaker than the expected ones for most of the models considered. This difference is due to slight upward fluctuations in the observed events across several categories in the signal region that signal events are expected to occupy.

As mentioned in Sec. 4.8.2, the results for the split SUSY models have been obtained assuming no interactions of the R-hadrons with the detector material. Nevertheless, the effect of matter interactions has been checked. A non-negligible fraction of R-hadrons that traverse the muon chambers are identified as muons. Similarly, charged R-hadrons that decay near the calorimeters may be reconstructed as isolated tracks. This leads to a reduction in acceptance for models with $c\tau \gtrsim 1 \text{ m}$

as a consequence of the veto on events containing muons or isolated tracks. The excluded mass regions weaken by 50–200 GeV for these signal models. The change is negligible for models with $c\tau \lesssim 1$ m.

Despite being optimised for prompt decay signatures and not employing dedicated techniques for identifying long-lived particles, the search can be seen to have a good sensitivity across a wide range of lifetimes and masses. This is mainly due to the inclusive nature of the search, with low thresholds on kinematic variables such as H_T and n_{jet} , and an acceptance to jets from ISR. In particular, this search provides coverage that is complementary to dedicated searches at the LHC (described in Sec. 2.6) for models with $c\tau \lesssim 1$ cm ($\tau \lesssim 10$ ps). This is because dedicated techniques require a minimum decay length. It is also complementary for models with a very compressed mass spectrum and a decay length within the scale of the detector, as in this case dedicated techniques require a sufficiently large mass difference such that the decay products can be reconstructed.

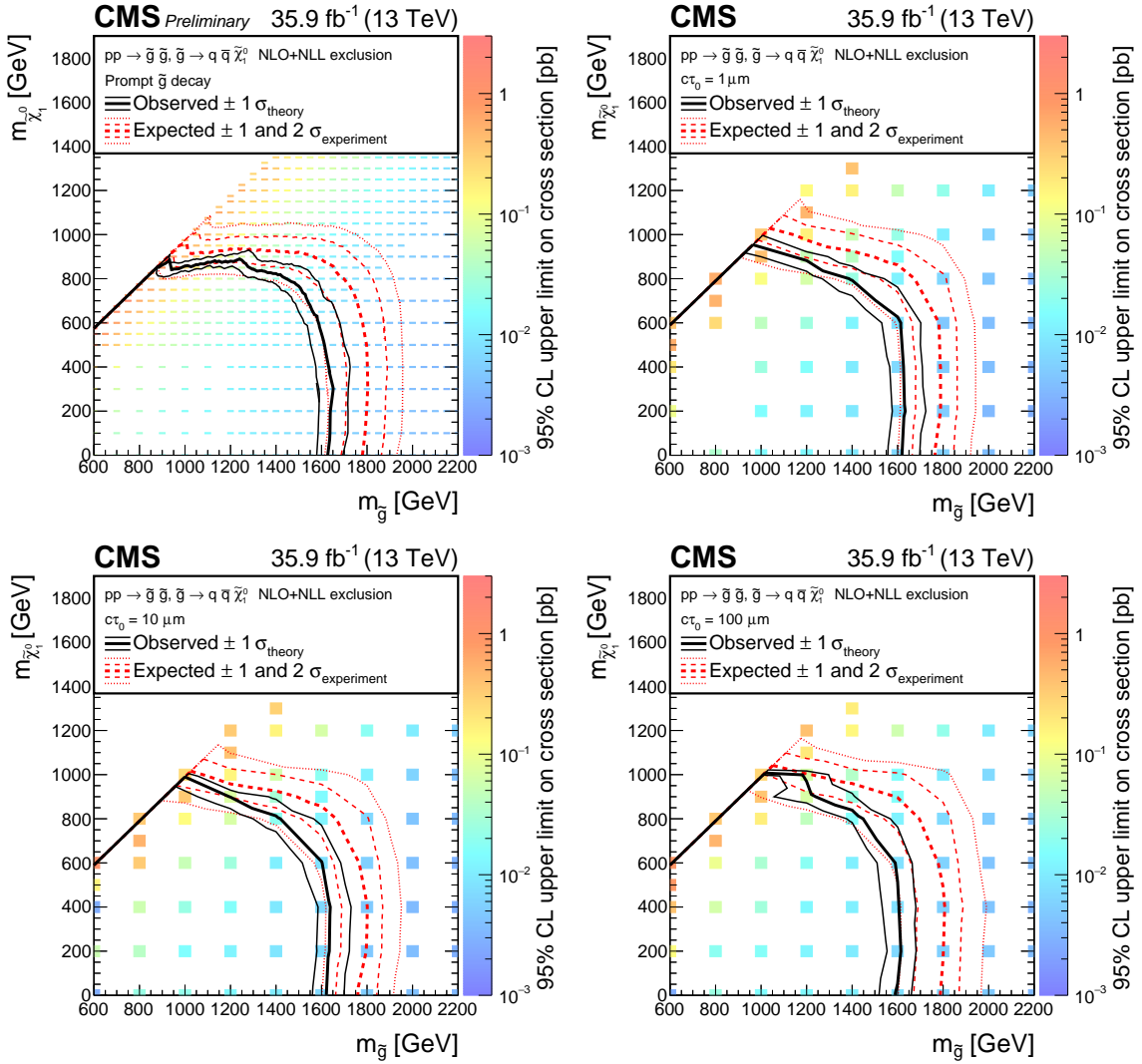


Figure 5.7.: Observed upper limit in cross section at 95% confidence level (indicated by the colour scale) as a function of the \tilde{g} and $\tilde{\chi}_1^0$ masses for the split SUSY simplified models. Each subfigure represents a different gluino lifetime. The thick (thin) black line indicates the observed excluded region assuming the nominal ($\pm 1\sigma$ in theoretical cross section uncertainty) production cross section. The red dashed (dashed and dotted) represents the median ($\pm 1\sigma$ and $\pm 2\sigma$ in experimental uncertainty) expected excluded region.

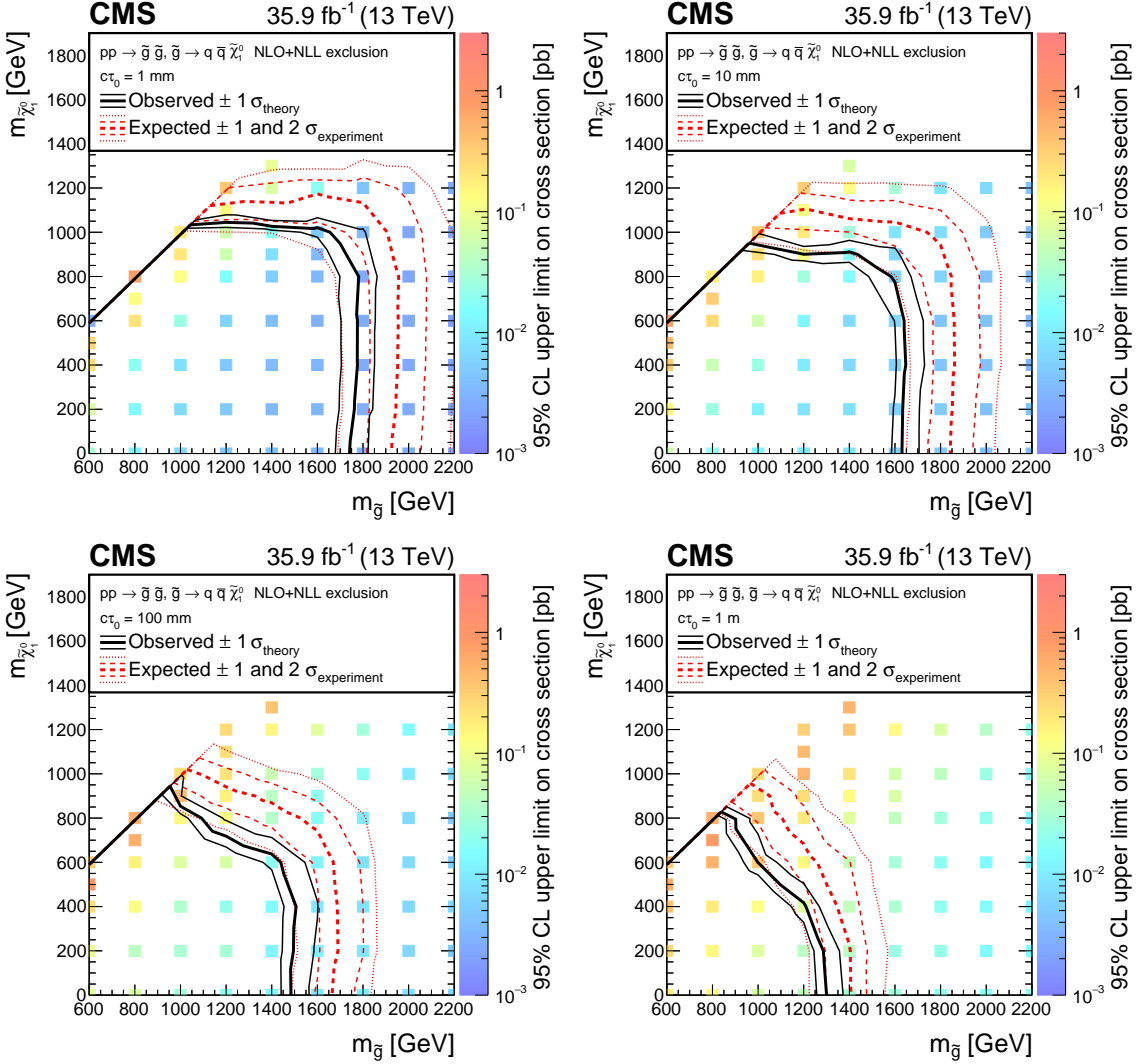


Figure 5.8: Observed upper limit in cross section at 95% confidence level (indicated by the colour scale) as a function of the \tilde{g} and $\tilde{\chi}_1^0$ masses for the split SUSY simplified models. Each subfigure represents a different gluino lifetime. The thick (thin) black line indicates the observed excluded region assuming the nominal ($\pm 1\sigma$ in theoretical cross section uncertainty) production cross section. The red dashed (dashed and dotted) represents the median ($\pm 1\sigma$ and $\pm 2\sigma$ in experimental uncertainty) expected excluded region.

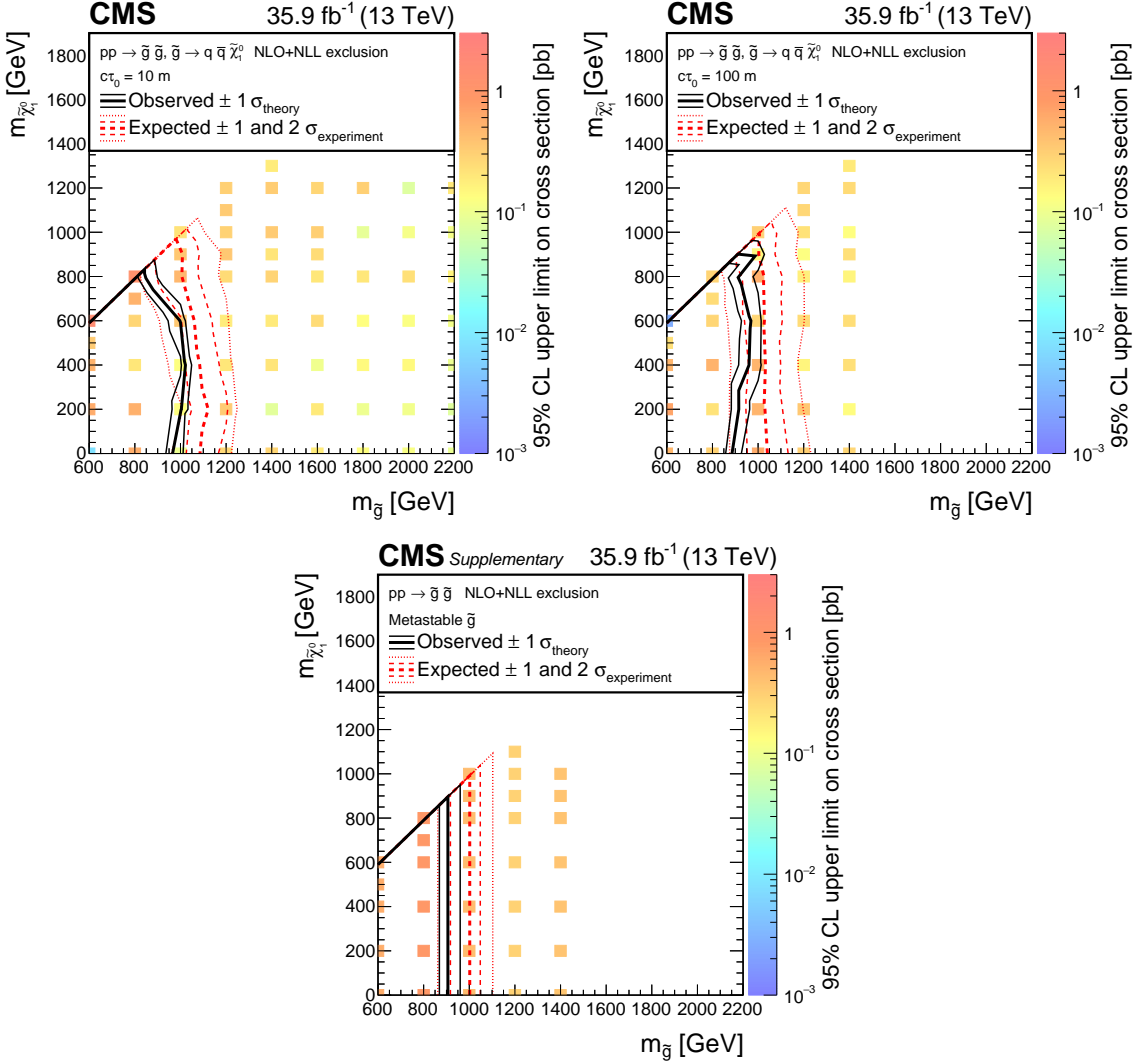


Figure 5.9.: Observed upper limit in cross section at 95% confidence level (indicated by the colour scale) as a function of the \tilde{g} and $\tilde{\chi}_1^0$ masses for the slit SUSY simplified models. Each subfigure represents a different gluino lifetime. The thick (thin) black line indicates the observed excluded region assuming the nominal ($\pm 1\sigma$ in theoretical cross section uncertainty) production cross section. The red dashed (dashed and dotted) represents the median ($\pm 1\sigma$ and $\pm 2\sigma$ in experimental uncertainty) expected excluded region.

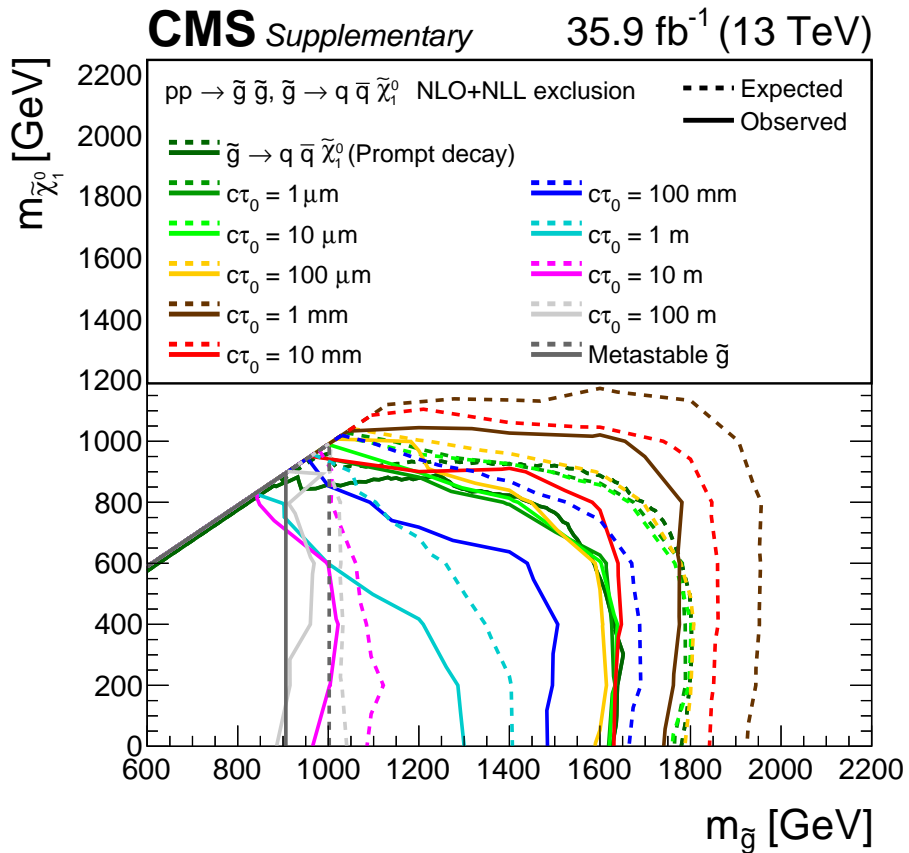


Figure 5.10.: Summary of observed and expected excluded regions at 95% confidence level as a function of the \tilde{g} and $\tilde{\chi}_1^0$ masses for various gluino lifetimes for the split SUSY simplified models.

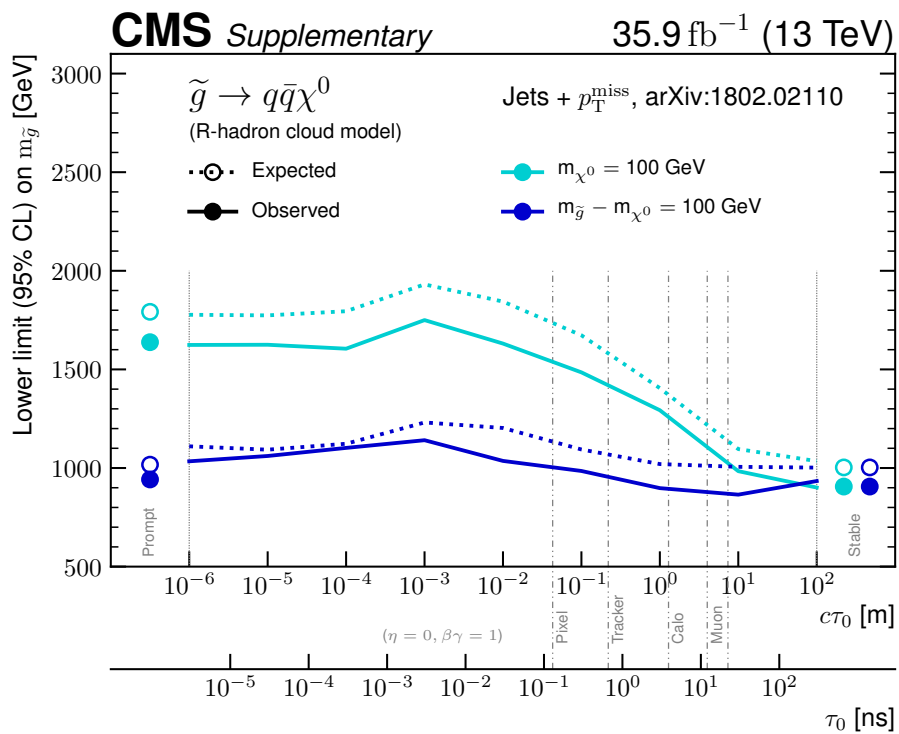


Figure 5.11.: Observed and expected lower limit at 95% confidence level on $m_{\tilde{g}}$ as a function of the gluino's lifetime for fixed $m_{\tilde{\chi}_1^0} = 100 \text{ GeV}$ and for $m_{\tilde{g}} - m_{\tilde{\chi}_1^0} = 100 \text{ GeV}$. The cases of a prompt and metastable gluino are also indicated.

Chapter 6.

Conclusion

The extremely successful standard model of particle physics was completed with the discovery of the Higgs boson at the LHC in 2012. However, it is clear that the standard model is not a complete theory. Its shortcomings include the lack of a dark matter particle and the non-inclusion of the gravitational force, among others. There are many theories beyond the standard model, such as supersymmetry, that attempt to solve its problems. Some of these models, such as split supersymmetry, predict the existence of massive long-lived particles. The LHC presents an excellent opportunity to search for new physics.

This thesis has presented an inclusive search for supersymmetry with the CMS detector in events containing missing transverse momentum and at least one jet. The data correspond to an integrated luminosity of 35.9 fb^{-1} of proton-proton collisions at a centre-of-mass energy of 13 TeV at the LHC. The analysis has been optimised for new physics signatures from promptly decaying particles, but is nevertheless sensitive to signatures from long-lived particles, providing complementary coverage to dedicated searches at the LHC, in particular for lifetimes of $c\tau \lesssim 1 \text{ cm}$. This is the first interpretation of a ‘prompt’ new physics search in the context of long-lived particles.

Candidate signal events are categorised according to the number of jets, the number of b-tagged jets, the total hadronic transverse energy and the missing hadronic transverse energy. The large QCD background is suppressed with dedicated kinematic variables. The dominant standard model backgrounds, namely $Z(\rightarrow \nu\nu) + \text{jets}$, $W(\rightarrow \ell\nu) + \text{jets}$ and $t\bar{t}$ are estimated using single and double muon control regions, and appropriate uncertainties are assigned. No significant excess above the standard model expectation in the observed number of events is found. Statistical

hypothesis tests are performed to set upper limits at 95% confidence level on the cross sections of simplified models of supersymmetry.

For models with promptly decaying SUSY particles, gluinos are excluded up to almost 2 TeV, and squarks are excluded up to over 1 TeV. For the split SUSY model, gluino masses up to 1750 and 900 GeV are excluded for gluinos with $c\tau = 1$ mm and metastable gluinos, respectively. These results do not consider the model-dependent interactions of R-hadrons with the detector material. The sensitivity of this search is only moderately dependent on these matter interactions for models with $c\tau \gtrsim 1$ m, while no dependence is found for models with $c\tau$ below 1 m.

There has been no evidence for physics beyond the standard model so far. However, the LHC still presents an excellent opportunity to discover new physics within the next decade, as it will continue to operate until a total integrated luminosity of 3000 fb^{-1} . As well as exploiting the larger dataset, more sophisticated search techniques can be developed. For example, a displaced jet tagging algorithm based on deep learning methods, similar to the b-tagging algorithm, would significantly improve the acceptance for long-lived particles over a wide range of lifetimes.

Appendix A.

Appendix: Search strategy

A.1. Uncertainties on transfer factors derived from variations in simulation

This appendix shows the changes of the transfer factors, which are used to assign systematic uncertainties to them, upon varying the various correction factors applied to the simulation (Sec. 4.9) by one standard deviation up and down according to their measured uncertainties. This is discussed in Sec. 4.12.1.

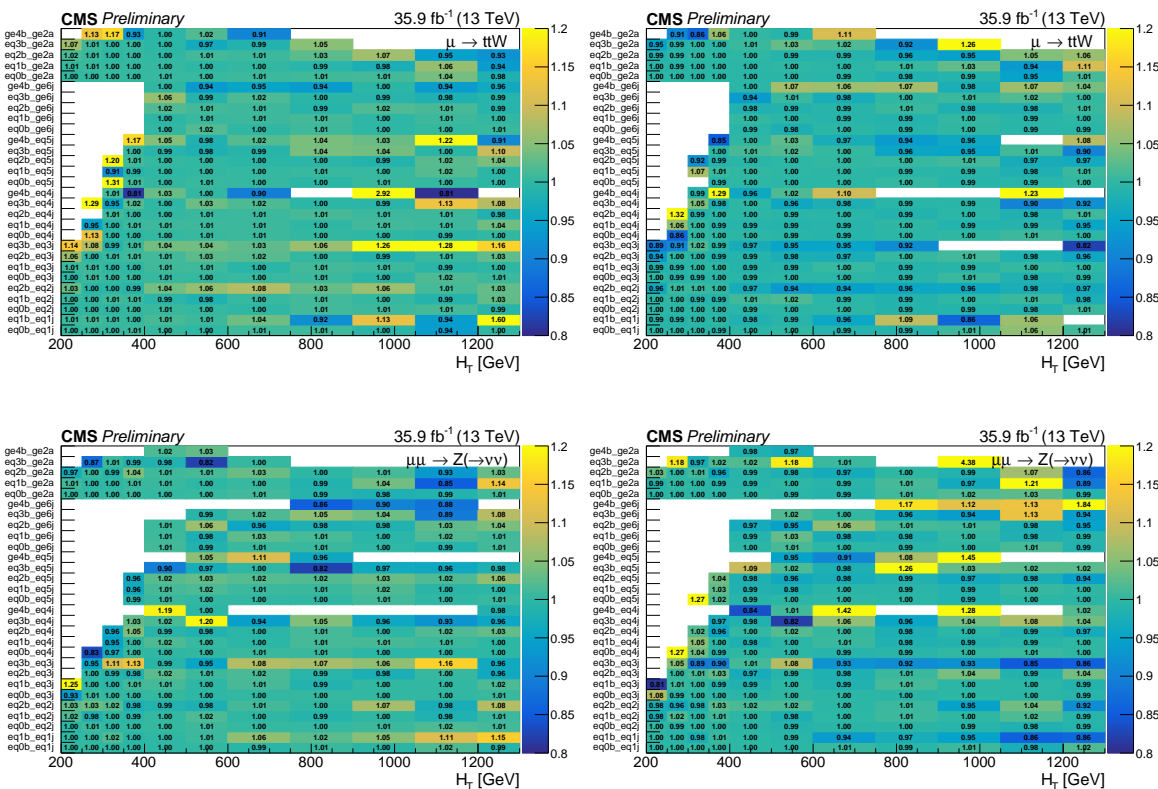


Figure A.1: The ratio of the $T(\mu \rightarrow W/t\bar{t})$ (top) and $T(\mu\mu \rightarrow Z)$ (bottom) transfer factors in each $(n_{\text{jet}}, n_b, H_T)$ bin when varying the pileup correction factors by $+1\sigma$ (left) and -1σ (right) with respect to their nominal values.

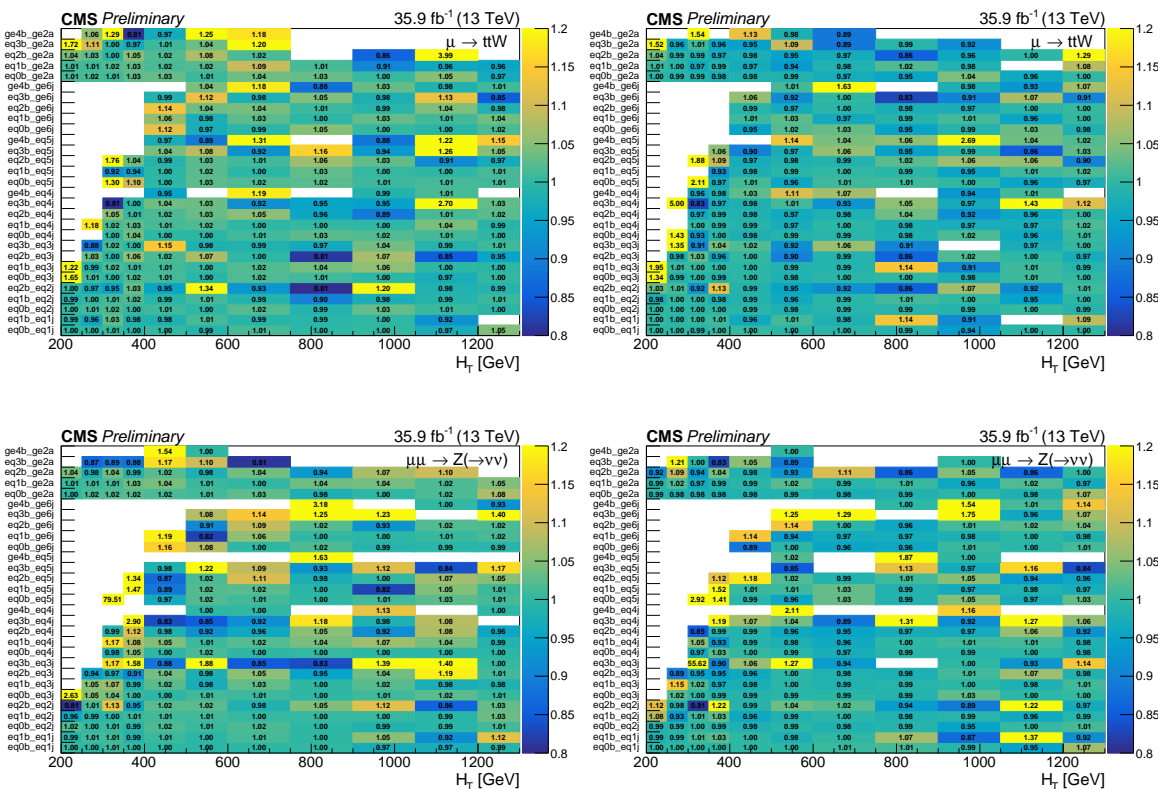


Figure A.2: The ratio of the $T(\mu \rightarrow W/t\bar{t})$ (top) and $T(\mu\mu \rightarrow Z)$ (bottom) transfer factors in each $(n_{\text{jet}}, n_b, H_T)$ bin when varying the jet energy correction factors by $+1\sigma$ (left) and -1σ (right) with respect to their nominal values.

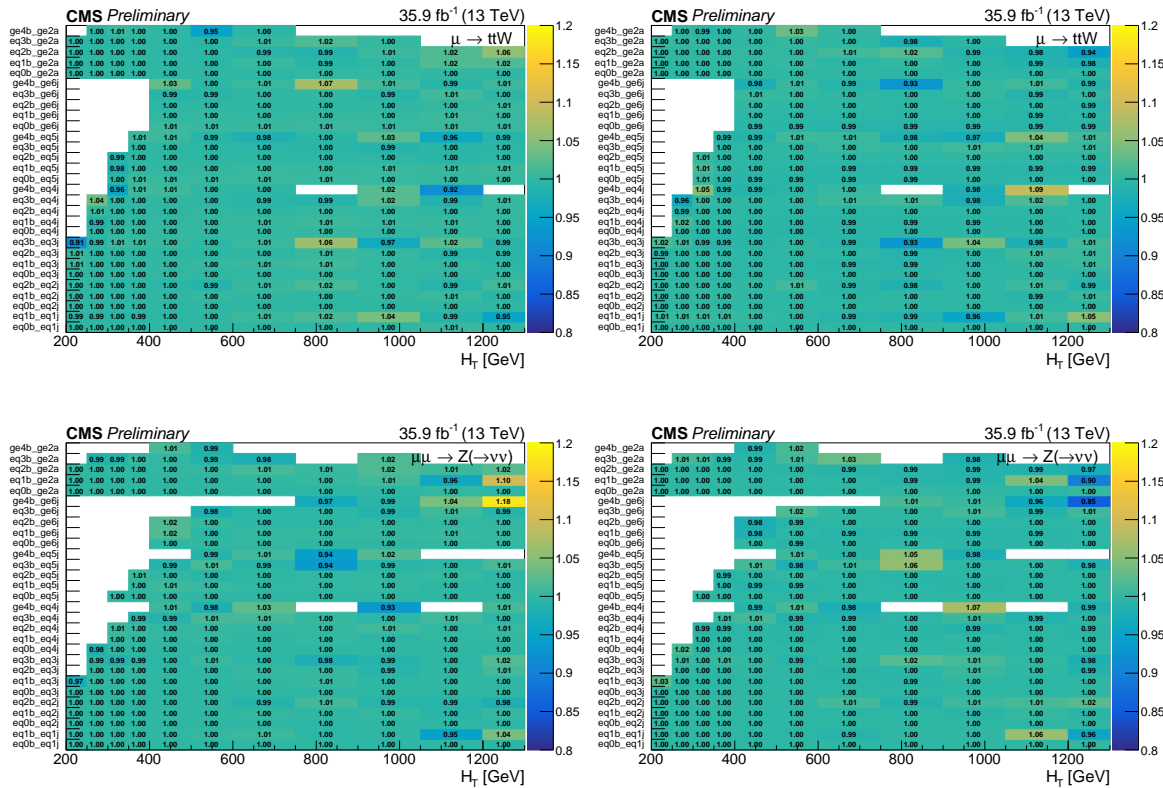


Figure A.3.: The ratio of the $T(\mu \rightarrow W/t\bar{t})$ (top) and $T(\mu\mu \rightarrow Z)$ (bottom) transfer factors in each (n_{jet} , n_b , H_T) bin when varying the b-tagging correction factors for bottom and charm quarks by $+1\sigma$ (left) and -1σ (right) with respect to their nominal values.

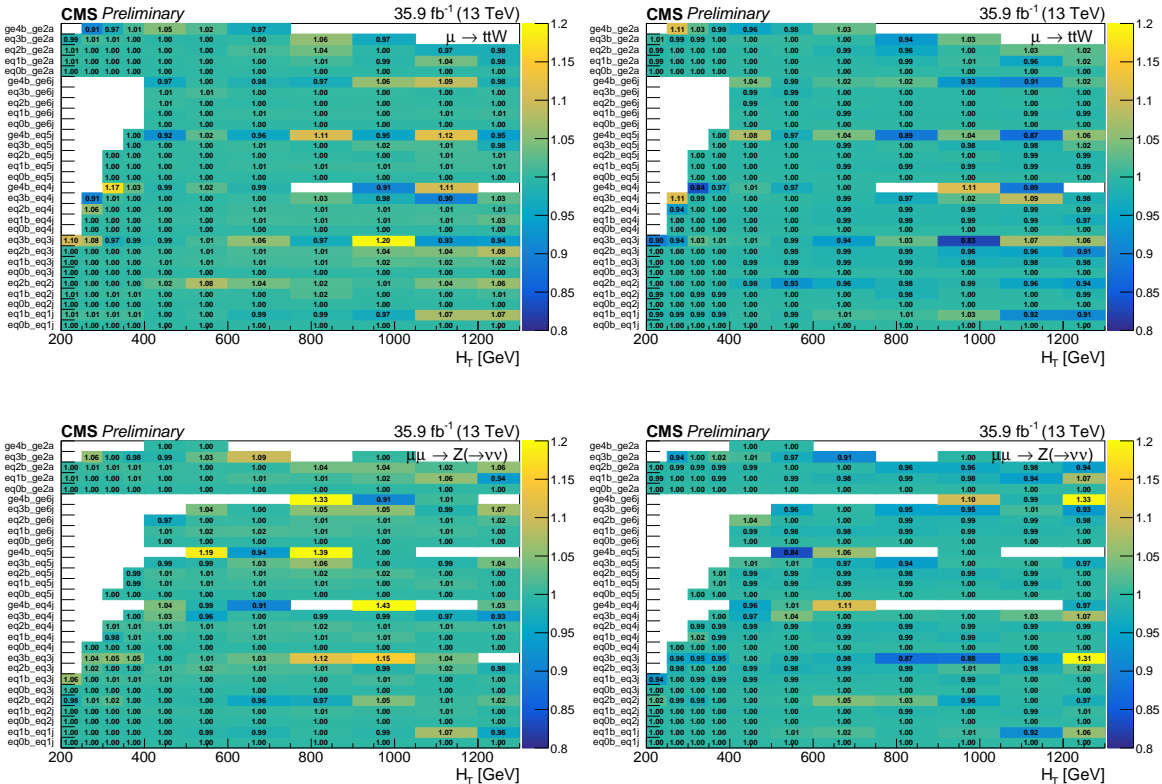


Figure A.4: The ratio of the $T(\mu \rightarrow W/t\bar{t})$ (top) and $T(\mu\mu \rightarrow Z)$ (bottom) transfer factors in each (n_{jet} , n_b , H_T) bin when varying the b-tagging correction factors for light partons (u, d, s, gluon) by $+1\sigma$ (left) and -1σ (right) with respect to their nominal values.

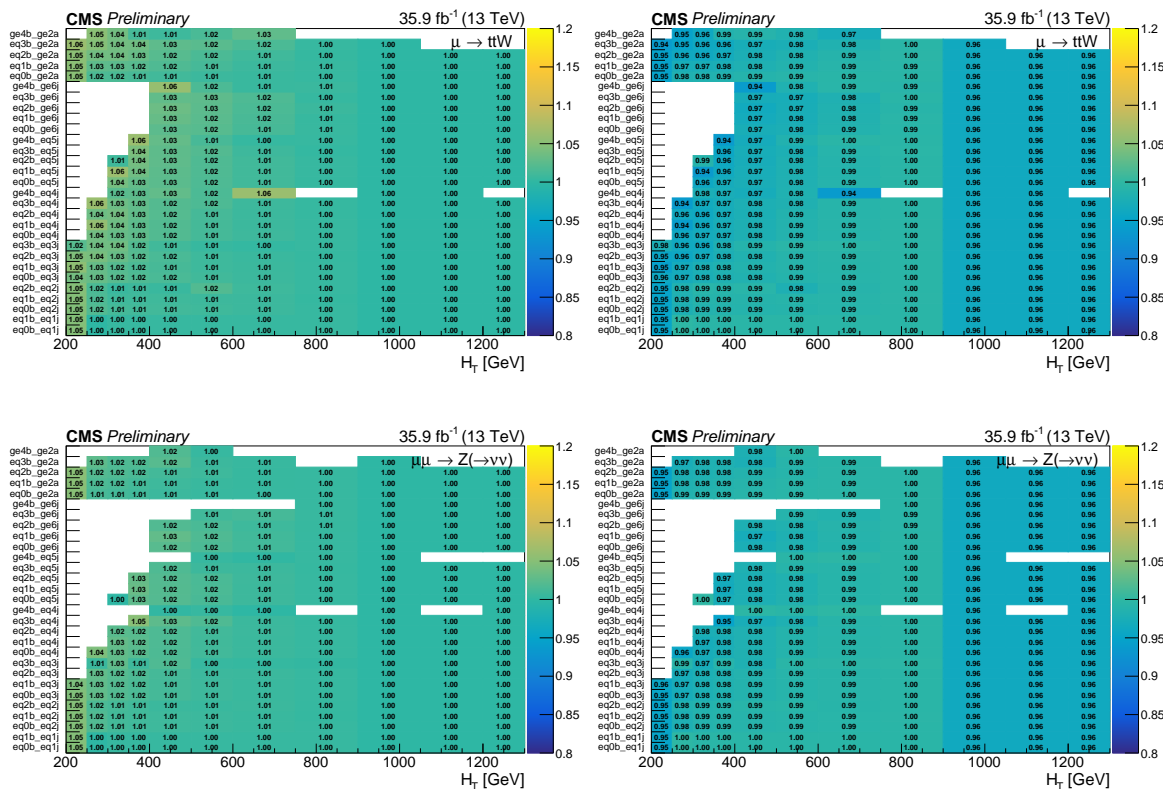


Figure A.5: The ratio of the $T(\mu \rightarrow W/t\bar{t})$ (top) and $T(\mu\mu \rightarrow Z)$ (bottom) transfer factors in each (n_{jet}, n_b, H_T) bin when varying the trigger correction factors by $+1\sigma$ (left) and -1σ (right) with respect to their nominal values.

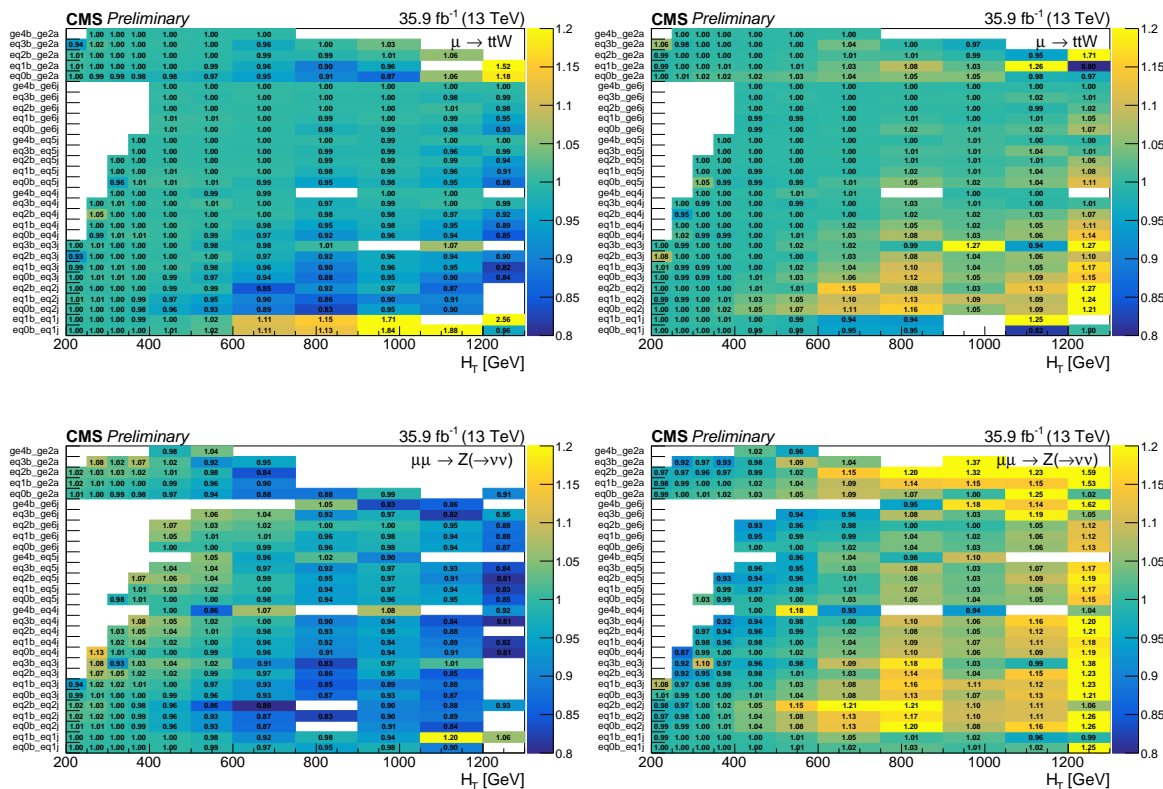


Figure A.6: The ratio of the $T(\mu \rightarrow W/t\bar{t})$ (top) and $T(\mu\mu \rightarrow Z)$ (bottom) transfer factors in each $(n_{\text{jet}}, n_b, H_T)$ bin when varying the boson p_T dependent NLO correction factors by $+1\sigma$ (left) and -1σ (right) with respect to their nominal values.

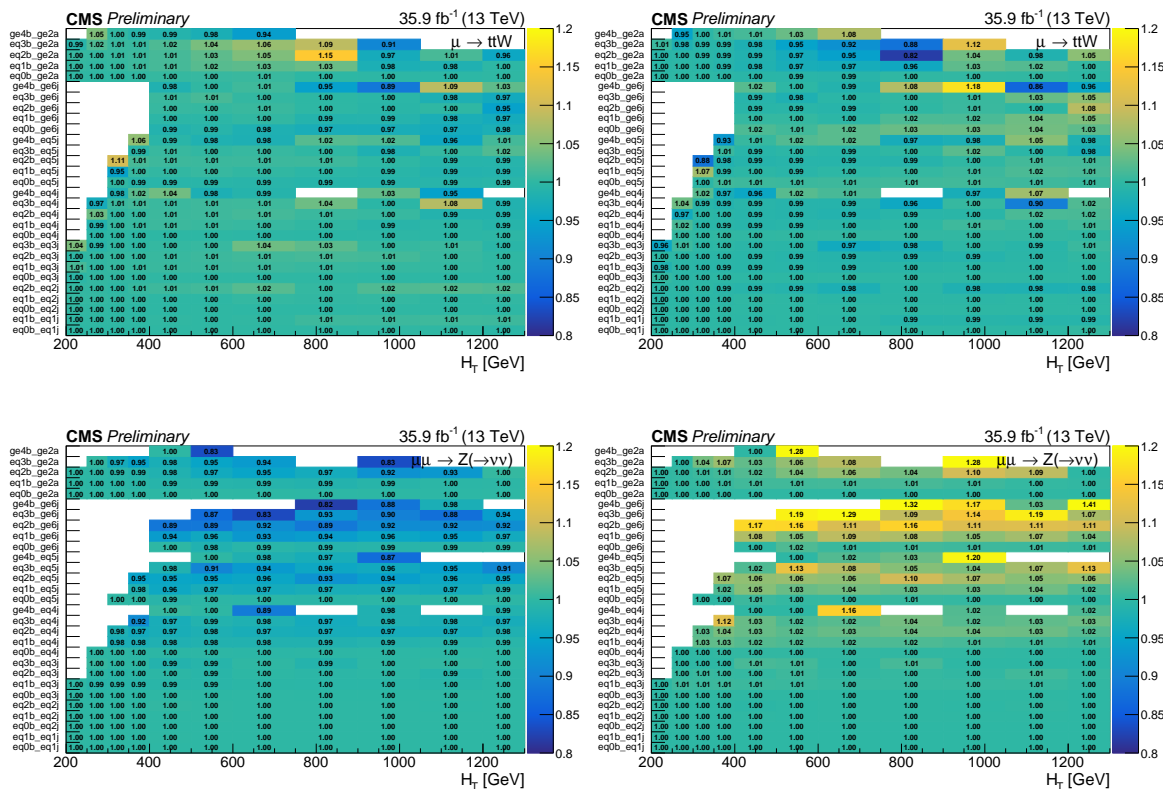


Figure A.7.: The ratio of the $T(\mu \rightarrow W/t\bar{t})$ (top) and $T(\mu\mu \rightarrow Z)$ (bottom) transfer factors in each $(n_{\text{jet}}, n_b, H_T)$ bin when varying the $t\bar{t}$ ISR correction factors by $+1\sigma$ (left) and -1σ (right) with respect to their nominal values.

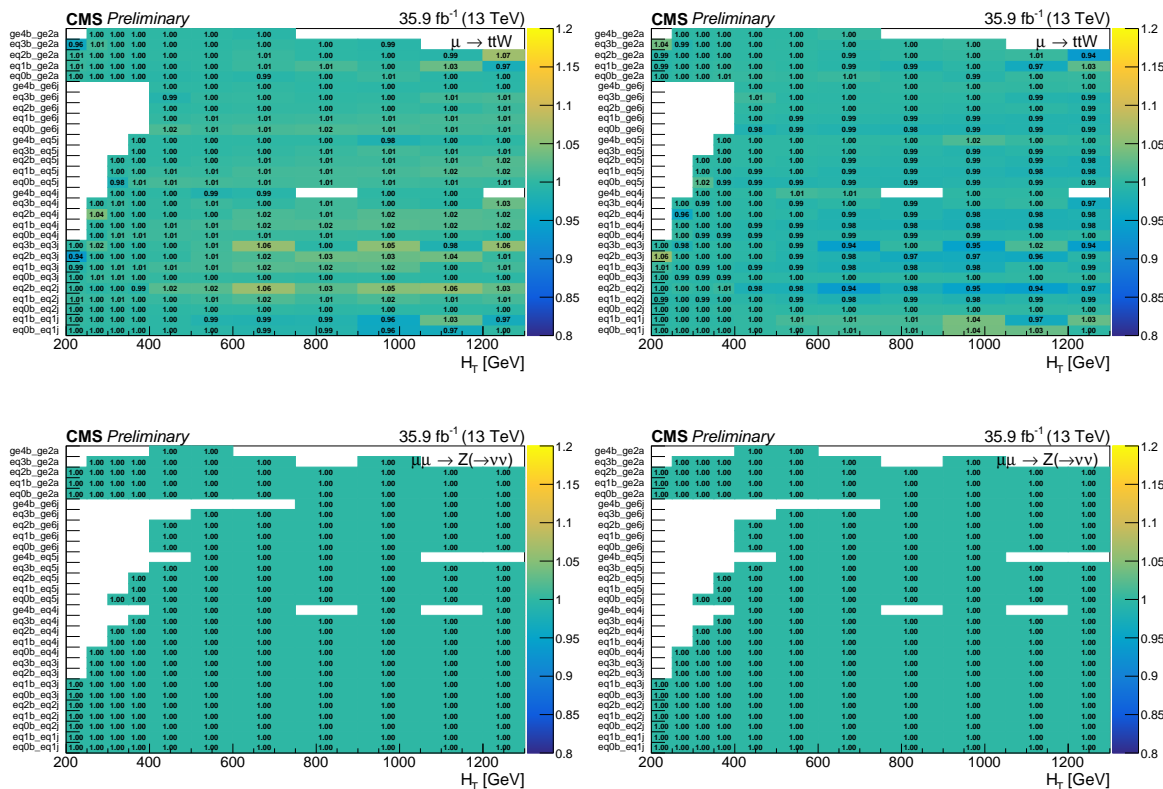


Figure A.8.: The ratio of the $T(\mu \rightarrow W/t\bar{t})$ (top) and $T(\mu\mu \rightarrow Z)$ (bottom) transfer factors in each $(n_{\text{jet}}, n_b, H_T)$ bin when varying the W cross section correction factors by $+1\sigma$ (left) and -1σ (right) with respect to their nominal values.

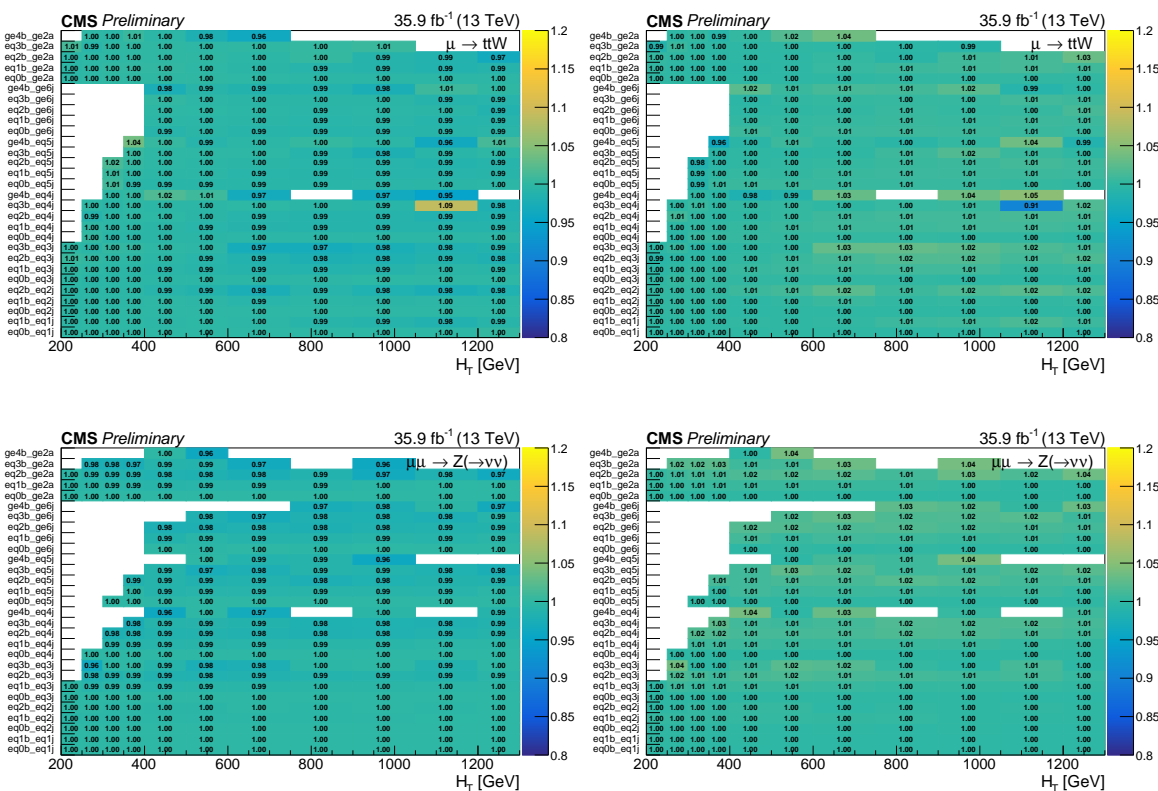


Figure A.9.: The ratio of the $T(\mu \rightarrow W/t\bar{t})$ (top) and $T(\mu\mu \rightarrow Z)$ (bottom) transfer factors in each $(n_{\text{jet}}, n_b, H_T)$ bin when varying the $t\bar{t}$ cross section correction factors by $+1\sigma$ (left) and -1σ (right) with respect to their nominal values.

Appendix B.

Appendix: Results and interpretation

B.1. Comparison of expected background and observed data

This appendix shows the results of the maximum likelihood fit to the control regions under the background-only hypothesis, as discussed in Sec. 5.4, in tabulated form.

Table B.1.: Observed data counts and background expectations from the background-only likelihood fit to the control regions, for the $n_{\text{jet}} = 1$ category. The uncertainties in the background expectations include statistical as well as systematic contributions.

n_{jet}	n_b	H_T [GeV]	Data	SM		
1	0	200 – 400	291353	254856.1	\pm	30252.2
1	0	400 – 600	8572	7342.2	\pm	610.4
1	0	600 – 900	878	680.1	\pm	206.4
1	0	900 – ∞	57	56.9	\pm	31.6
1	1	200 – 400	11072	8864.3	\pm	1044.9
1	1	400 – 600	406	334.6	\pm	32.4
1	1	600 – ∞	71	41.5	\pm	13.1

Table B.2.: Observed data counts and background expectations from the background-only likelihood fit to the control regions, for the $n_{\text{jet}} \geq 2a$ category. The uncertainties in the background expectations include statistical as well as systematic contributions.

n_{jet}	n_b	H_T [GeV]	\mathcal{H}_T [GeV]	Data	SM	
$\geq 2a$	0	200 – 400	$200 - \infty$	116868	101411.4	\pm 14127.9
$\geq 2a$	0	400 – 600	200 – 400	2932	2909.4	\pm 396.2
$\geq 2a$	0	400 – 600	$400 - \infty$	2800	2582.2	\pm 345.7
$\geq 2a$	0	600 – 900	200 – 400	31	22.7	\pm 5.2
$\geq 2a$	0	600 – 900	400 – 600	75	63.8	\pm 12.3
$\geq 2a$	0	600 – 900	$600 - \infty$	211	198.9	\pm 62.8
$\geq 2a$	0	$900 - \infty$	200 – 900	28	31.8	\pm 12.5
$\geq 2a$	0	$900 - \infty$	$900 - \infty$	54	50.3	\pm 32.0
$\geq 2a$	1	200 – 400	$200 - \infty$	16307	13333.6	\pm 1563.7
$\geq 2a$	1	400 – 600	200 – 400	1042	969.1	\pm 129.2
$\geq 2a$	1	400 – 600	$400 - \infty$	310	275.8	\pm 36.0
$\geq 2a$	1	600 – 900	200 – 400	8	13.7	\pm 2.7
$\geq 2a$	1	600 – 900	400 – 600	12	11.4	\pm 1.8
$\geq 2a$	1	600 – 900	$600 - \infty$	26	21.5	\pm 6.4
$\geq 2a$	1	$900 - \infty$	200 – 900	5	3.9	\pm 1.5
$\geq 2a$	1	$900 - \infty$	$900 - \infty$	7	6.3	\pm 4.0
$\geq 2a$	2	200 – 400	$200 - \infty$	2200	1856.5	\pm 229.0
$\geq 2a$	2	400 – 600	200 – 400	410	373.9	\pm 52.5
$\geq 2a$	2	400 – 600	$400 - \infty$	35	23.9	\pm 3.4
$\geq 2a$	2	600 – 900	200 – 400	4	5.9	\pm 1.2
$\geq 2a$	2	600 – 900	400 – 600	4	2.3	\pm 0.4
$\geq 2a$	2	600 – 900	$600 - \infty$	2	1.7	\pm 0.5
$\geq 2a$	2	$900 - \infty$	200 – 900	1	0.6	\pm 0.1
$\geq 2a$	2	$900 - \infty$	$900 - \infty$	0	0.4	\pm 0.3
$\geq 2a$	3	200 – 400	$200 - \infty$	92	70.7	\pm 10.0
$\geq 2a$	3	400 – 600	200 – 400	38	34.4	\pm 5.4
$\geq 2a$	3	400 – 600	$400 - \infty$	2	0.6	\pm 0.1
$\geq 2a$	3	$600 - \infty$	200 – 400	1	0.9	\pm 0.2
$\geq 2a$	3	$600 - \infty$	400 – 600	0	0.2	\pm 0.0
$\geq 2a$	3	$600 - \infty$	$600 - \infty$	0	0.1	\pm 0.0

Table B.3.: Observed data counts and background expectations from the background-only likelihood fit to the control regions, for the $n_{\text{jet}} = 2$ category. The uncertainties in the background expectations include statistical as well as systematic contributions.

n_{jet}	n_b	H_T [GeV]	\mathcal{H}_T [GeV]	Data	SM	
2	0	200 – 400	200 – ∞	34934	29224.5	\pm 6798.6
2	0	400 – 600	200 – 400	3468	3274.3	\pm 759.7
2	0	400 – 600	400 – ∞	2568	2176.9	\pm 560.2
2	0	600 – 900	200 – 400	226	276.7	\pm 74.0
2	0	600 – 900	400 – 600	253	268.4	\pm 65.1
2	0	600 – 900	600 – ∞	303	284.6	\pm 110.9
2	0	900 – 1200	200 – 400	165	179.3	\pm 54.6
2	0	900 – 1200	400 – 600	125	130.9	\pm 34.6
2	0	900 – 1200	600 – 900	97	78.7	\pm 35.5
2	0	900 – 1200	900 – ∞	25	29.3	\pm 19.3
2	0	1200 – ∞	200 – 400	9	11.8	\pm 5.1
2	0	1200 – ∞	400 – 600	26	33.4	\pm 9.7
2	0	1200 – ∞	600 – 900	22	28.0	\pm 12.9
2	0	1200 – ∞	900 – ∞	19	20.9	\pm 16.7
2	1	200 – 400	200 – ∞	3850	3006.6	\pm 674.9
2	1	400 – 600	200 – 400	327	277.4	\pm 65.3
2	1	400 – 600	400 – ∞	240	219.3	\pm 55.1
2	1	600 – 900	200 – 400	22	26.9	\pm 7.1
2	1	600 – 900	400 – 600	39	25.5	\pm 6.3
2	1	600 – 900	600 – ∞	31	27.1	\pm 10.1
2	1	900 – 1200	200 – 400	17	19.3	\pm 5.8
2	1	900 – 1200	400 – 600	15	14.9	\pm 4.0
2	1	900 – 1200	600 – 900	12	7.4	\pm 3.3
2	1	900 – 1200	900 – ∞	6	3.2	\pm 2.1
2	1	1200 – ∞	200 – 400	1	1.1	\pm 0.5
2	1	1200 – ∞	400 – 600	6	3.4	\pm 1.0
2	1	1200 – ∞	600 – 900	1	2.1	\pm 0.9
2	1	1200 – ∞	900 – ∞	4	2.0	\pm 1.6
2	2	200 – 400	200 – ∞	254	196.1	\pm 44.4
2	2	400 – 600	200 – 400	22	13.2	\pm 3.2
2	2	400 – 600	400 – ∞	18	15.2	\pm 3.8
2	2	600 – ∞	200 – 400	1	1.8	\pm 0.5
2	2	600 – ∞	400 – 600	2	1.9	\pm 0.5
2	2	600 – ∞	600 – ∞	2	2.3	\pm 0.9

Table B.4.: Observed data counts and background expectations from the background-only likelihood fit to the control regions, for the $n_{\text{jet}} = 3$ category. The uncertainties in the background expectations include statistical as well as systematic contributions.

n_{jet}	n_b	H_T [GeV]	\mathcal{H}_T [GeV]	Data	SM	
3	0	200 – 400	200 – ∞	11815	10504.3	\pm 1860.3
3	0	400 – 600	200 – 400	7120	6666.9	\pm 1143.0
3	0	400 – 600	400 – ∞	1463	1391.0	\pm 288.2
3	0	600 – 900	200 – 400	668	698.5	\pm 132.2
3	0	600 – 900	400 – 600	593	582.0	\pm 123.5
3	0	600 – 900	600 – ∞	246	231.4	\pm 91.2
3	0	900 – 1200	200 – 400	245	275.3	\pm 47.6
3	0	900 – 1200	400 – 600	164	182.3	\pm 31.1
3	0	900 – 1200	600 – 900	101	109.8	\pm 42.1
3	0	900 – 1200	900 – ∞	19	28.2	\pm 16.4
3	0	1200 – ∞	200 – 400	21	22.5	\pm 6.5
3	0	1200 – ∞	400 – 600	28	54.2	\pm 11.0
3	0	1200 – ∞	600 – 900	31	36.1	\pm 13.3
3	0	1200 – ∞	900 – ∞	17	22.0	\pm 15.6
3	1	200 – 400	200 – ∞	2703	2242.6	\pm 400.0
3	1	400 – 600	200 – 400	1212	1125.8	\pm 197.2
3	1	400 – 600	400 – ∞	301	222.4	\pm 42.5
3	1	600 – 900	200 – 400	110	94.6	\pm 18.3
3	1	600 – 900	400 – 600	96	77.9	\pm 16.2
3	1	600 – 900	600 – ∞	42	32.7	\pm 12.4
3	1	900 – 1200	200 – 400	39	41.2	\pm 7.5
3	1	900 – 1200	400 – 600	24	23.9	\pm 4.1
3	1	900 – 1200	600 – 900	10	15.4	\pm 5.8
3	1	900 – 1200	900 – ∞	6	4.4	\pm 2.2
3	1	1200 – ∞	200 – 400	3	3.4	\pm 0.9
3	1	1200 – ∞	400 – 600	5	7.5	\pm 1.6
3	1	1200 – ∞	600 – 900	7	5.1	\pm 1.9
3	1	1200 – ∞	900 – ∞	4	3.5	\pm 2.4
3	2	200 – 400	200 – ∞	495	418.2	\pm 79.0
3	2	400 – 600	200 – 400	229	208.3	\pm 38.9
3	2	400 – 600	400 – ∞	34	27.0	\pm 5.2
3	2	600 – 900	200 – 400	10	9.1	\pm 1.8
3	2	600 – 900	400 – 600	9	9.3	\pm 1.9
3	2	600 – 900	600 – ∞	2	3.2	\pm 1.2
3	2	900 – 1200	200 – 400	4	3.5	\pm 0.7
3	2	900 – 1200	400 – 600	2	1.8	\pm 0.3
3	2	900 – 1200	600 – 900	2	1.3	\pm 0.5
3	2	900 – 1200	900 – ∞	0	0.4	\pm 0.2
3	2	1200 – ∞	200 – 400	1	0.3	\pm 0.1
3	2	1200 – ∞	400 – 600	0	0.7	\pm 0.1
3	2	1200 – ∞	600 – 900	0	0.4	\pm 0.2
3	2	1200 – ∞	900 – ∞	0	0.3	\pm 0.2
3	3	200 – 400	200 – ∞	16	12.1	\pm 2.5
3	3	400 – 600	200 – 400	10	7.9	\pm 1.6
3	3	400 – 600	400 – ∞	2	0.8	\pm 0.2
3	3	600 – ∞	200 – 400	3	0.4	\pm 0.1
3	3	600 – ∞	400 – 600	3	0.3	\pm 0.1
3	3	600 – ∞	600 – ∞	0	0.2	\pm 0.1

Table B.5.: Observed data counts and background expectations from the background-only likelihood fit to the control regions, for the $n_{\text{jet}} = 4$ category. The uncertainties in the background expectations include statistical as well as systematic contributions.

n_{jet}	n_b	H_T [GeV]	\mathcal{H}_T [GeV]	Data	SM	
4	0	400 – 600	200 – 400	4324	4749.1	\pm 621.7
4	0	400 – 600	400 – ∞	437	460.4	\pm 78.3
4	0	600 – 900	200 – 400	751	937.0	\pm 113.5
4	0	600 – 900	400 – 600	484	521.7	\pm 76.4
4	0	600 – 900	600 – ∞	110	103.7	\pm 35.1
4	0	900 – 1200	200 – 400	186	251.2	\pm 36.7
4	0	900 – 1200	400 – 600	111	142.9	\pm 20.7
4	0	900 – 1200	600 – 900	66	71.7	\pm 25.6
4	0	900 – 1200	900 – ∞	13	10.6	\pm 5.8
4	0	1200 – ∞	200 – 400	13	23.8	\pm 6.0
4	0	1200 – ∞	400 – 600	32	43.0	\pm 8.2
4	0	1200 – ∞	600 – 900	28	26.8	\pm 9.9
4	0	1200 – ∞	900 – ∞	15	13.9	\pm 9.4
4	1	400 – 600	200 – 400	1497	1444.4	\pm 191.1
4	1	400 – 600	400 – ∞	109	109.8	\pm 16.5
4	1	600 – 900	200 – 400	184	196.6	\pm 23.6
4	1	600 – 900	400 – 600	106	100.9	\pm 14.0
4	1	600 – 900	600 – ∞	19	17.2	\pm 5.5
4	1	900 – 1200	200 – 400	60	53.8	\pm 7.6
4	1	900 – 1200	400 – 600	19	27.7	\pm 4.1
4	1	900 – 1200	600 – 900	11	12.3	\pm 4.2
4	1	900 – 1200	900 – ∞	1	1.8	\pm 1.0
4	1	1200 – ∞	200 – 400	7	5.2	\pm 1.3
4	1	1200 – ∞	400 – 600	11	10.6	\pm 2.1
4	1	1200 – ∞	600 – 900	7	4.8	\pm 1.7
4	1	1200 – ∞	900 – ∞	4	2.9	\pm 1.8
4	2	400 – 600	200 – 400	524	490.0	\pm 72.7
4	2	400 – 600	400 – ∞	29	24.0	\pm 4.0
4	2	600 – 900	200 – 400	50	39.2	\pm 5.0
4	2	600 – 900	400 – 600	19	19.9	\pm 2.7
4	2	600 – 900	600 – ∞	1	2.4	\pm 0.7
4	2	900 – 1200	200 – 400	10	8.7	\pm 1.2
4	2	900 – 1200	400 – 600	7	4.1	\pm 0.7
4	2	900 – 1200	600 – 900	0	1.7	\pm 0.6
4	2	900 – 1200	900 – ∞	1	0.3	\pm 0.2
4	2	1200 – ∞	200 – 400	1	0.7	\pm 0.2
4	2	1200 – ∞	400 – 600	0	1.5	\pm 0.3
4	2	1200 – ∞	600 – 900	0	0.5	\pm 0.2
4	2	1200 – ∞	900 – ∞	1	0.4	\pm 0.2
4	3	400 – 600	200 – 400	35	36.8	\pm 6.0
4	3	400 – 600	400 – ∞	1	1.6	\pm 0.3
4	3	600 – 900	200 – 400	6	2.5	\pm 0.3
4	3	600 – 900	400 – 600	0	1.2	\pm 0.2
4	3	600 – 900	600 – ∞	0	0.2	\pm 0.0
4	3	900 – ∞	200 – 400	0	0.7	\pm 0.1
4	3	900 – ∞	400 – 600	0	0.4	\pm 0.1
4	3	900 – ∞	600 – 900	0	0.1	\pm 0.0
4	3	900 – ∞	900 – ∞	0	0.0	\pm 0.0

Table B.6.: Observed data counts and background expectations from the background-only likelihood fit to the control regions, for the $n_{\text{jet}} = 5$ category. The uncertainties in the background expectations include statistical as well as systematic contributions.

n_{jet}	n_b	H_T [GeV]	\mathcal{H}_T [GeV]	Data	SM	
5	0	400 – 600	200 – 400	1132	1250.0	\pm 197.6
5	0	400 – 600	$400 - \infty$	59	74.0	\pm 16.6
5	0	600 – 900	200 – 400	435	561.4	\pm 80.0
5	0	600 – 900	400 – 600	201	197.5	\pm 35.4
5	0	600 – 900	$600 - \infty$	17	25.9	\pm 9.5
5	0	900 – 1200	200 – 400	124	149.9	\pm 21.2
5	0	900 – 1200	400 – 600	59	68.1	\pm 10.1
5	0	900 – 1200	$600 - \infty$	28	30.7	\pm 11.6
5	0	$1200 - \infty$	200 – 400	7	18.1	\pm 4.7
5	0	$1200 - \infty$	400 – 600	16	23.1	\pm 4.7
5	0	$1200 - \infty$	600 – 900	7	13.2	\pm 5.2
5	0	$1200 - \infty$	$900 - \infty$	6	6.2	\pm 4.3
5	1	400 – 600	200 – 400	591	608.6	\pm 105.2
5	1	400 – 600	$400 - \infty$	22	22.0	\pm 4.5
5	1	600 – 900	200 – 400	198	194.1	\pm 29.9
5	1	600 – 900	400 – 600	50	55.2	\pm 9.2
5	1	600 – 900	$600 - \infty$	11	5.9	\pm 1.9
5	1	900 – 1200	200 – 400	33	41.0	\pm 5.8
5	1	900 – 1200	400 – 600	15	16.9	\pm 2.4
5	1	900 – 1200	$600 - \infty$	9	7.0	\pm 2.4
5	1	$1200 - \infty$	200 – 400	4	4.5	\pm 1.1
5	1	$1200 - \infty$	400 – 600	3	6.1	\pm 1.2
5	1	$1200 - \infty$	600 – 900	5	2.8	\pm 1.0
5	1	$1200 - \infty$	$900 - \infty$	2	1.6	\pm 1.1
5	2	400 – 600	200 – 400	284	273.9	\pm 51.3
5	2	400 – 600	$400 - \infty$	10	4.8	\pm 1.0
5	2	600 – 900	200 – 400	63	67.5	\pm 11.6
5	2	600 – 900	400 – 600	16	16.5	\pm 2.8
5	2	600 – 900	$600 - \infty$	0	1.3	\pm 0.4
5	2	900 – 1200	200 – 400	5	10.5	\pm 1.6
5	2	900 – 1200	400 – 600	5	3.5	\pm 0.6
5	2	900 – 1200	$600 - \infty$	1	1.5	\pm 0.5
5	2	$1200 - \infty$	200 – 400	0	1.0	\pm 0.2
5	2	$1200 - \infty$	400 – 600	2	1.2	\pm 0.2
5	2	$1200 - \infty$	600 – 900	1	0.4	\pm 0.1
5	2	$1200 - \infty$	$900 - \infty$	1	0.3	\pm 0.2
5	3	400 – 600	200 – 400	25	28.0	\pm 5.4
5	3	400 – 600	$400 - \infty$	1	0.3	\pm 0.1
5	3	600 – 900	200 – 400	7	7.5	\pm 1.3
5	3	600 – 900	400 – 600	3	1.5	\pm 0.3
5	3	600 – 900	$600 - \infty$	0	0.1	\pm 0.0
5	3	$900 - \infty$	200 – 400	0	1.1	\pm 0.2
5	3	$900 - \infty$	400 – 600	0	0.4	\pm 0.1
5	3	$900 - \infty$	$600 - \infty$	0	0.2	\pm 0.1
5	≥ 4	400 – ∞	200 – 400	2	1.8	\pm 0.4
5	≥ 4	400 – ∞	$400 - \infty$	1	0.1	\pm 0.0

Table B.7.: Observed data counts and background expectations from the background-only likelihood fit to the control regions, for the $n_{\text{jet}} \geq 6$ category. The uncertainties in the background expectations include statistical as well as systematic contributions.

n_{jet}	n_b	H_T [GeV]	\mathcal{H}_T [GeV]	Data	SM	
≥ 6	0	400 – 600	$200 - \infty$	164	193.7	\pm 34.3
≥ 6	0	600 – 900	200 – 400	210	278.0	\pm 54.6
≥ 6	0	600 – 900	$400 - \infty$	56	68.1	\pm 37.3
≥ 6	0	900 – 1200	200 – 400	64	94.4	\pm 29.3
≥ 6	0	900 – 1200	400 – 600	32	34.2	\pm 16.3
≥ 6	0	900 – 1200	$600 - \infty$	9	12.0	\pm 10.7
≥ 6	0	$1200 - \infty$	200 – 400	12	18.3	\pm 10.0
≥ 6	0	$1200 - \infty$	400 – 600	9	16.8	\pm 4.0
≥ 6	0	$1200 - \infty$	600 – 900	11	8.6	\pm 5.7
≥ 6	0	$1200 - \infty$	$900 - \infty$	5	2.8	\pm 3.3
≥ 6	1	400 – 600	$200 - \infty$	121	135.5	\pm 29.0
≥ 6	1	600 – 900	200 – 400	148	154.3	\pm 32.3
≥ 6	1	600 – 900	$400 - \infty$	26	25.3	\pm 9.8
≥ 6	1	900 – 1200	200 – 400	42	41.7	\pm 10.3
≥ 6	1	900 – 1200	400 – 600	11	12.1	\pm 4.3
≥ 6	1	900 – 1200	$600 - \infty$	1	3.3	\pm 2.6
≥ 6	1	$1200 - \infty$	200 – 400	6	7.4	\pm 3.2
≥ 6	1	$1200 - \infty$	400 – 600	5	5.9	\pm 1.3
≥ 6	1	$1200 - \infty$	600 – 900	5	2.6	\pm 1.6
≥ 6	1	$1200 - \infty$	$900 - \infty$	0	0.8	\pm 0.9
≥ 6	2	400 – 600	$200 - \infty$	58	69.5	\pm 16.1
≥ 6	2	600 – 900	200 – 400	85	74.4	\pm 16.9
≥ 6	2	600 – 900	$400 - \infty$	8	8.5	\pm 2.7
≥ 6	2	900 – 1200	200 – 400	11	17.9	\pm 4.4
≥ 6	2	900 – 1200	400 – 600	3	4.2	\pm 1.2
≥ 6	2	900 – 1200	$600 - \infty$	0	0.8	\pm 0.6
≥ 6	2	$1200 - \infty$	200 – 400	0	2.5	\pm 0.9
≥ 6	2	$1200 - \infty$	400 – 600	0	1.6	\pm 0.4
≥ 6	2	$1200 - \infty$	600 – 900	2	0.6	\pm 0.3
≥ 6	2	$1200 - \infty$	$900 - \infty$	0	0.2	\pm 0.2
≥ 6	3	400 – 600	$200 - \infty$	14	8.9	\pm 2.2
≥ 6	3	600 – 900	200 – 400	20	11.1	\pm 2.7
≥ 6	3	600 – 900	$400 - \infty$	3	1.1	\pm 0.4
≥ 6	3	900 – 1200	200 – 400	4	3.0	\pm 0.8
≥ 6	3	900 – 1200	400 – 600	0	0.6	\pm 0.2
≥ 6	3	900 – 1200	$600 - \infty$	0	0.1	\pm 0.1
≥ 6	3	$1200 - \infty$	200 – 400	1	0.4	\pm 0.1
≥ 6	3	$1200 - \infty$	400 – 600	0	0.2	\pm 0.1
≥ 6	3	$1200 - \infty$	600 – 900	1	0.1	\pm 0.0
≥ 6	3	$1200 - \infty$	$900 - \infty$	0	0.0	\pm 0.0
≥ 6	≥ 4	400 – 600	$200 - \infty$	4	2.5	\pm 0.7

B.2. Results under likelihood fit to signal and control regions

This appendix shows the results of the maximum likelihood fit to the signal and control regions under the background-only hypothesis. The same result under a fit to the control regions only (excluding the signal region) was shown in Sec. 5.4.

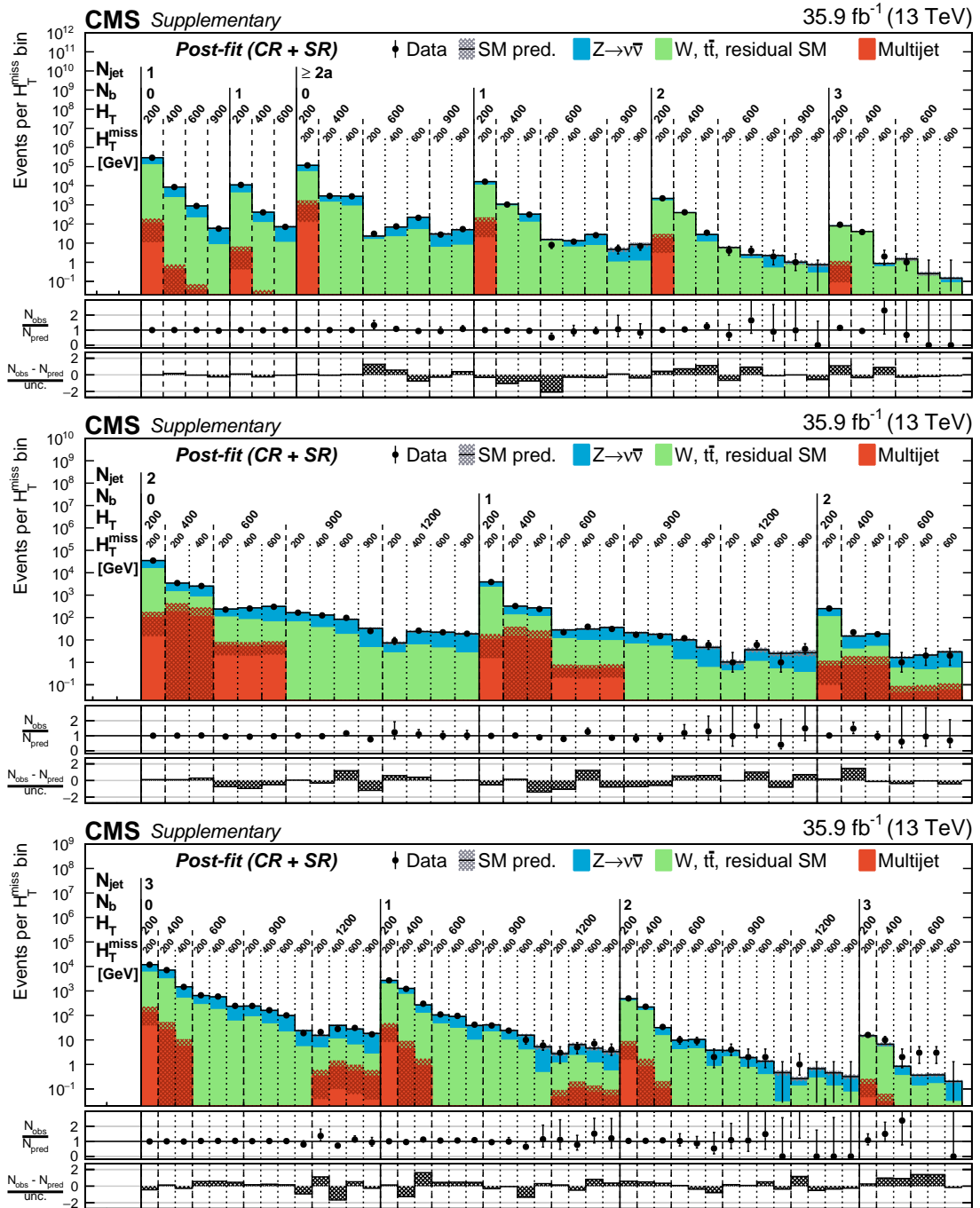


Figure B.1.: Number of events observed (solid markers) and expected number of Z , $W/t\bar{t}$ and QCD background events (histograms, with shaded bands representing the statistical and systematic uncertainties) in every n_b , H_T and H_T^{miss} bin of the jet categories $n_{\text{jet}} = 1, \geq 2a$ (top), $n_{\text{jet}} = 2$ (middle), and $n_{\text{jet}} = 3$ (bottom), as determined from the maximum likelihood fit to the signal and control regions. The centre panel of each sub-figure shows the ratios of the observed and expected counts, while the lower panel shows the corresponding z-score, as defined in the text.

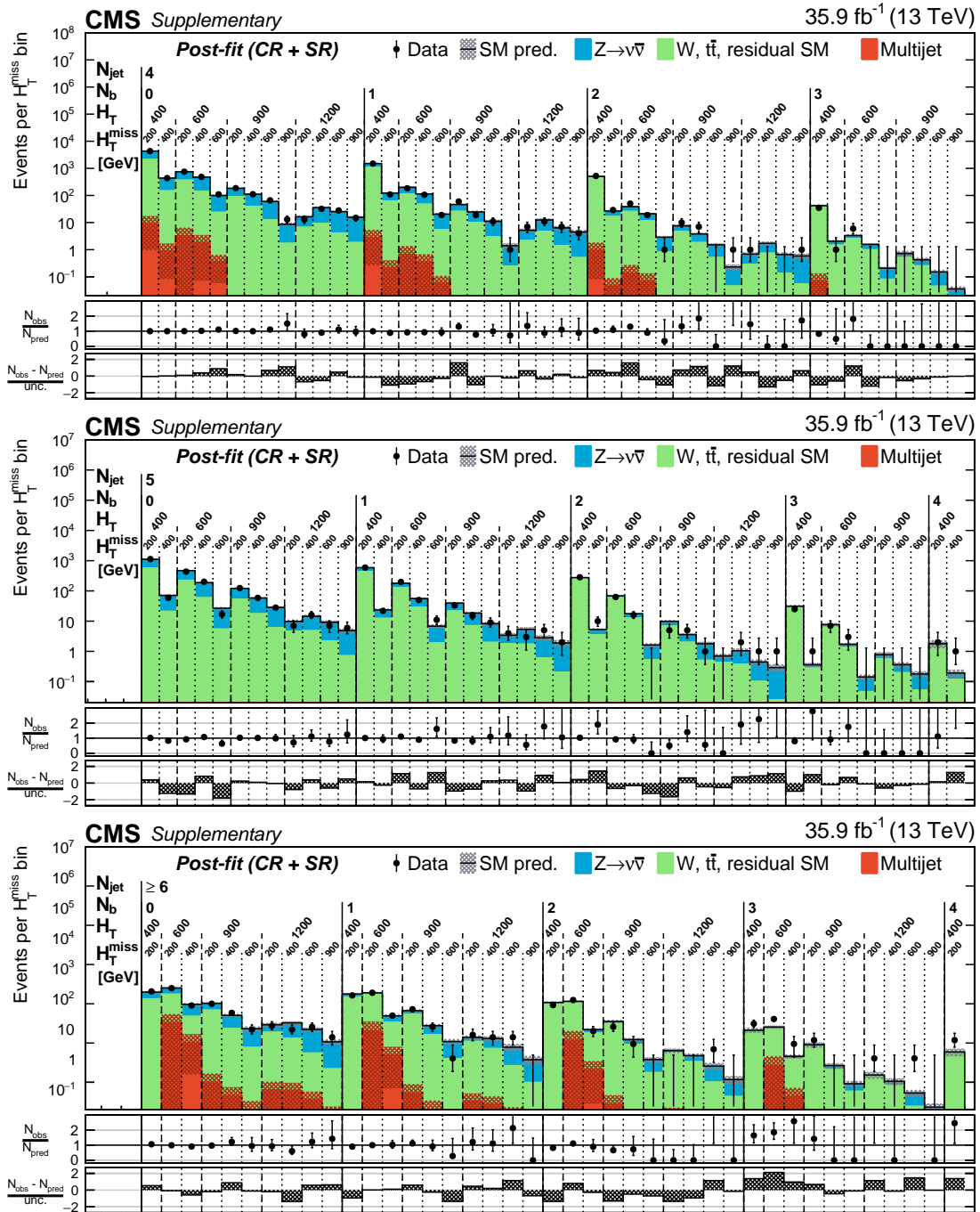


Figure B.2.: Number of events observed (solid markers) and expected number of Z , $W/t\bar{t}$ and QCD background events (histograms, with shaded bands representing the statistical and systematic uncertainties) in every n_b , H_T and H_T^{miss} bin of the jet categories $n_{\text{jet}} = 4$ (top), $n_{\text{jet}} = 5$ (middle), and $n_{\text{jet}} \geq 6$ (bottom), as determined from the background-only maximum likelihood fit to the signal and control regions. The centre panel of each sub-figure shows the ratios of the observed and expected counts, while the lower panel shows the corresponding z-score, as defined in the text.

B.3. Nuisance parameters

This appendix shows the best fit values (and their uncertainties) of the nuisance parameters that encode the systematic uncertainties on the background estimates under a likelihood fit to the signal and control regions for the background-only hypothesis, as discussed in Sec. 5.4.

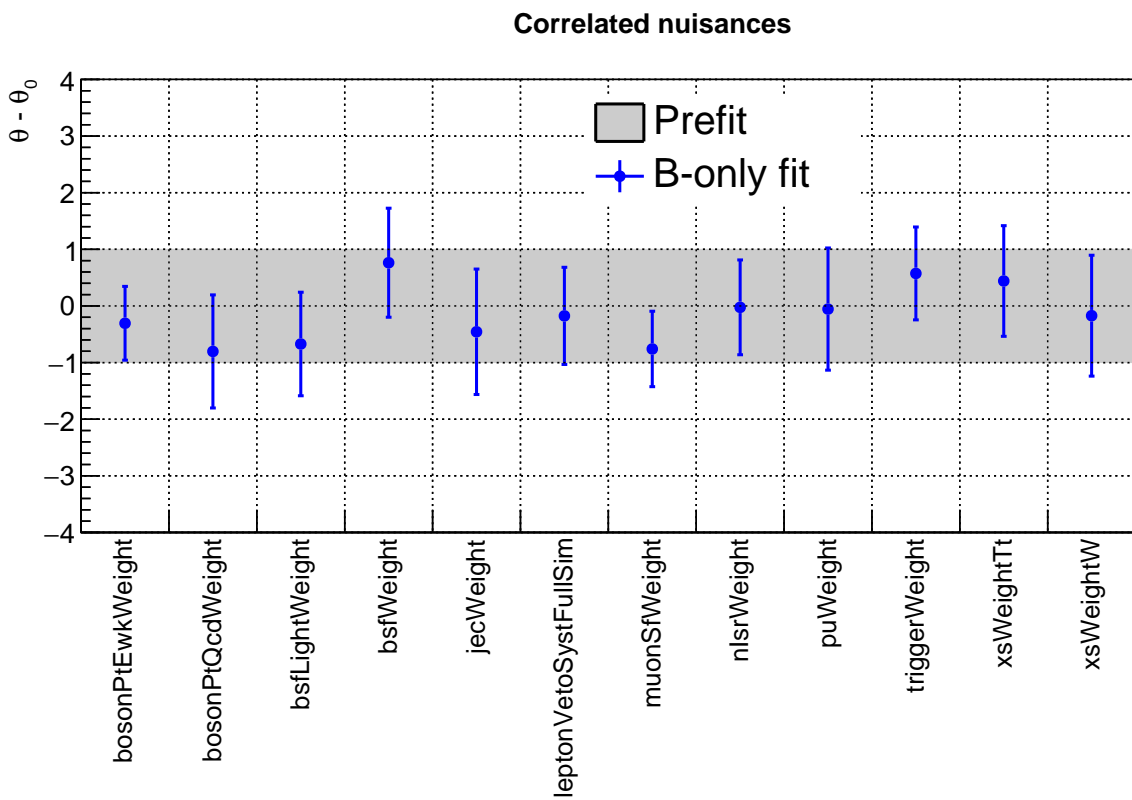


Figure B.3.: Maximum likelihood values of the nuisance parameters related to the systematic uncertainties derived from variations in the simulation correction factors, as determined from the background-only fit to the signal and control regions. From left to right: p_T dependent NLO QCD+EWK corrections; b-tagging efficiency for light and heavy quarks; jet energy; lepton identification, isolation and trigger; ISR jets; pileup; signal region triggers; W and $t\bar{t}$ cross sections.

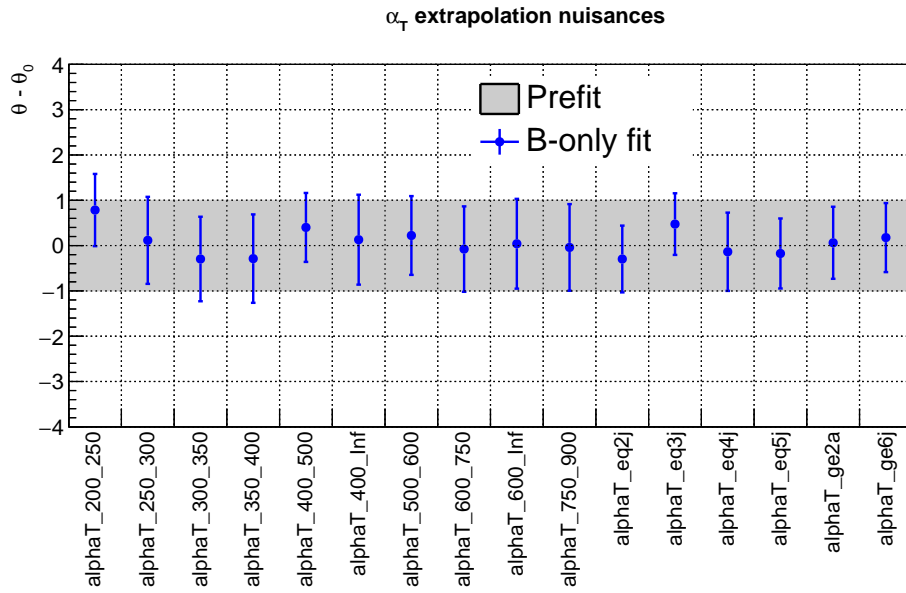


Figure B.4.: Maximum likelihood values of the nuisance parameters related to the systematic uncertainties derived from the α_T closure tests, as determined from the background-only fit to the signal and control regions.

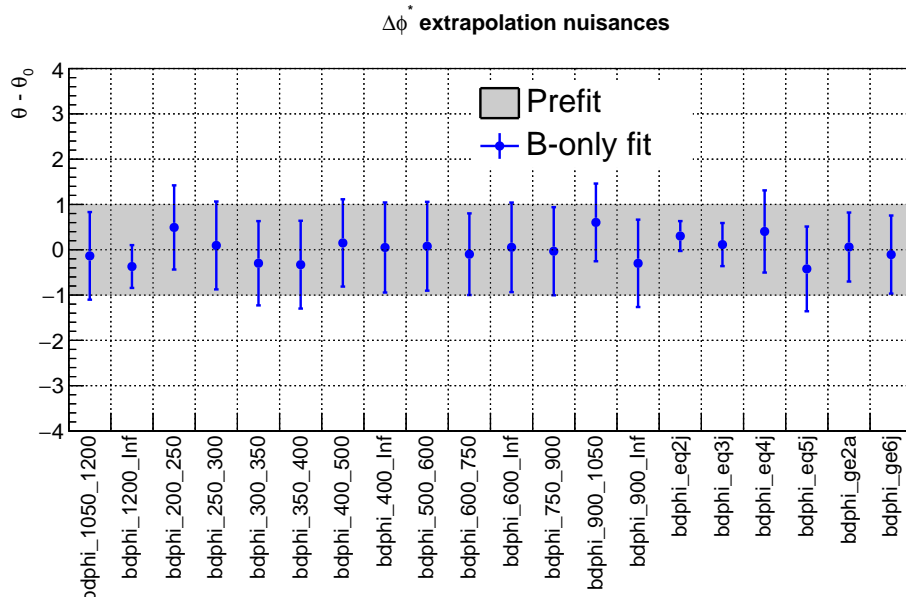


Figure B.5.: Maximum likelihood values of the nuisance parameters related to the systematic uncertainties derived from the $\Delta\phi_{\min}^*$ closure tests, as determined from the background-only fit to the signal and control regions.

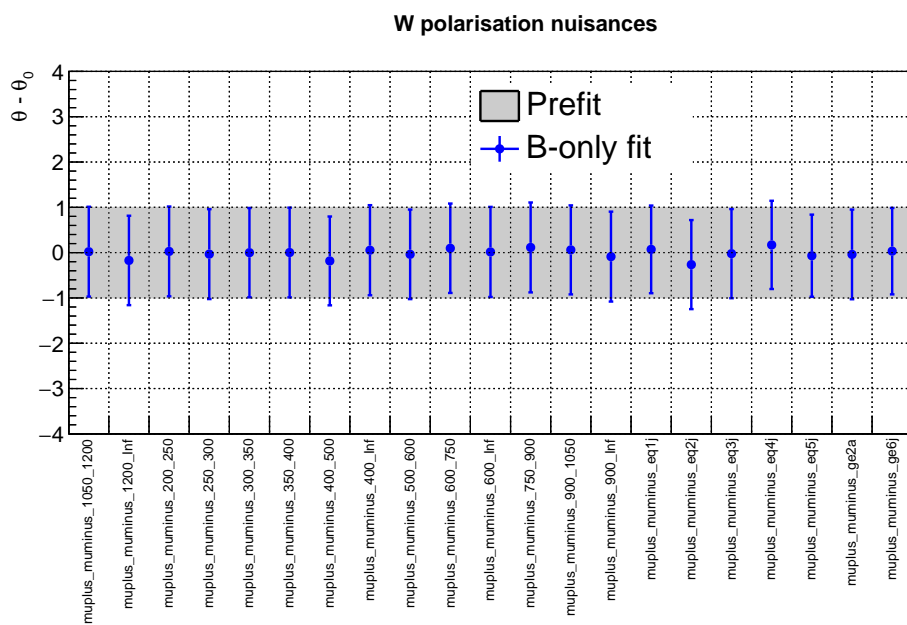


Figure B.6.: Maximum likelihood values of the nuisance parameters related to the systematic uncertainties derived from the W^+ / W^- closure tests, as determined from the background-only fit to the signal and control regions.

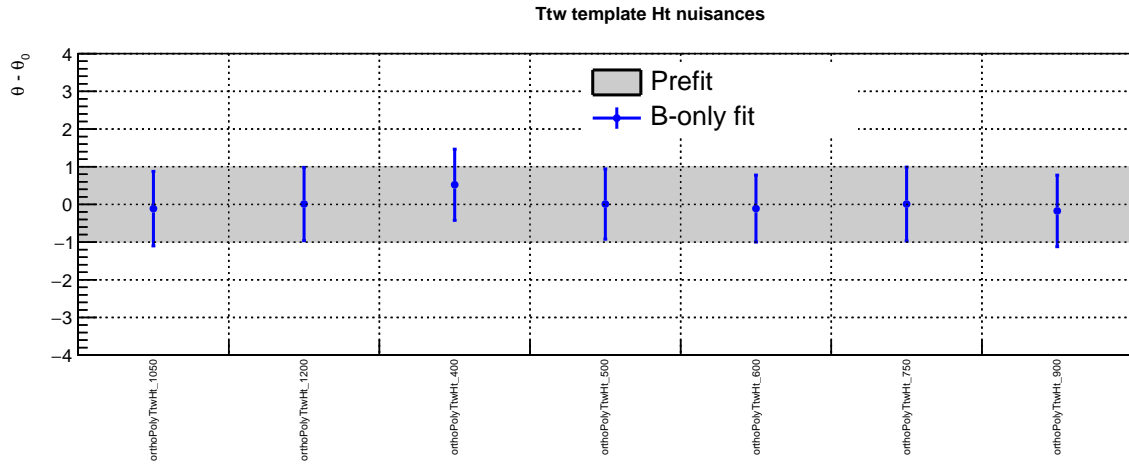


Figure B.7.: Maximum likelihood values of the nuisance parameters related to the H_T -dependent systematic uncertainties on the H_T shape of the $W/t\bar{t}$ processes, as determined from the background-only fit to the signal and control regions.

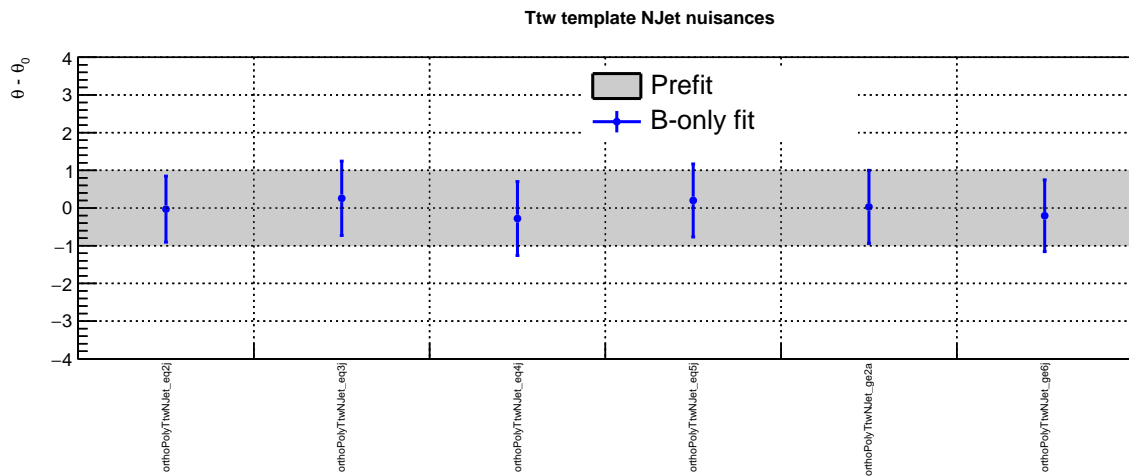


Figure B.8.: Maximum likelihood values of the nuisance parameters related to the n_{jet} -dependent systematic uncertainties on the H_T shape of the $W/t\bar{t}$ processes, as determined from the background-only fit to the signal and control regions.

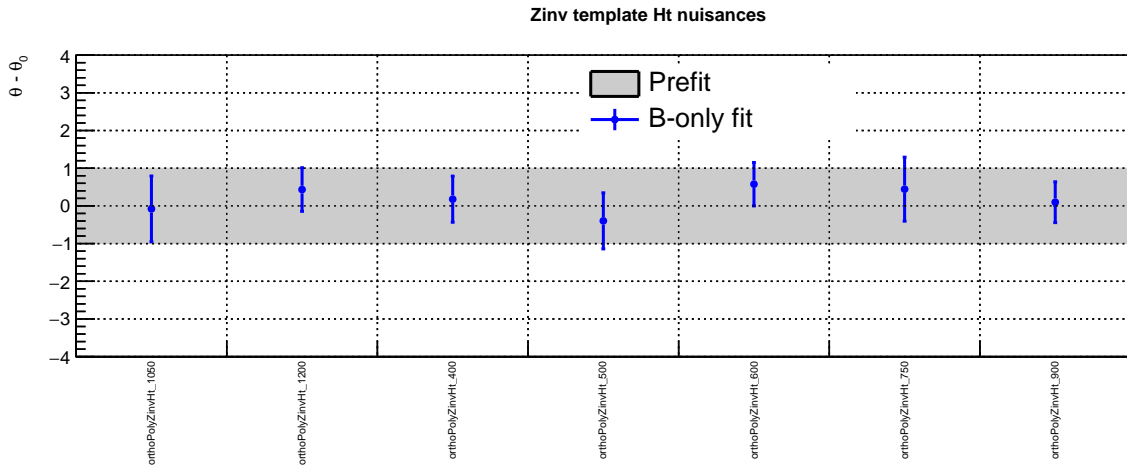


Figure B.9.: Maximum likelihood values of the nuisance parameters related to the H_T -dependent systematic uncertainties on the \mathcal{H}_T shape of the $Z(\rightarrow \nu\nu) + \text{jets}$ process, as determined from the background-only fit to the signal and control regions.

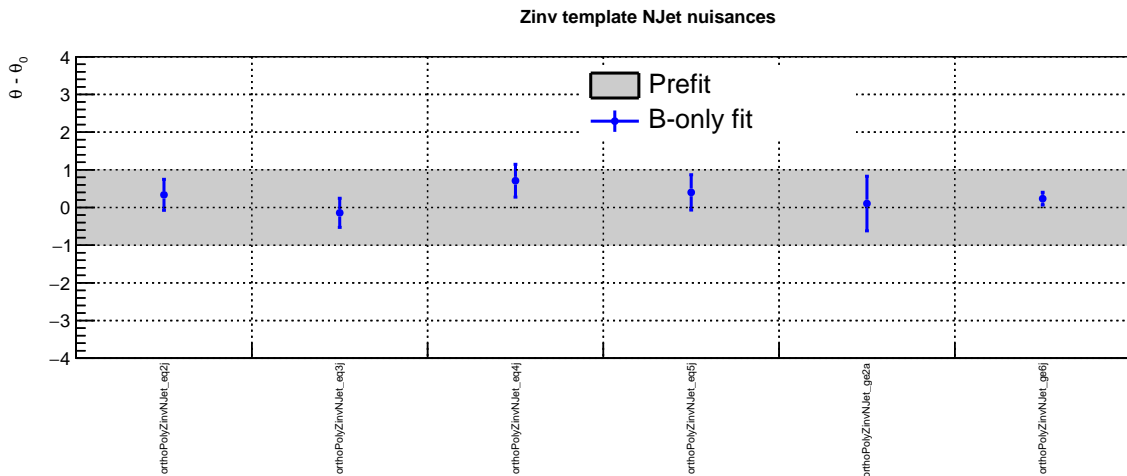


Figure B.10.: Maximum likelihood values of the nuisance parameters related to the n_{jet} -dependent systematic uncertainties on the \mathcal{H}_T shape of the $Z(\rightarrow \nu\nu) + \text{jets}$ process, as determined from the background-only fit to the signal and control regions.

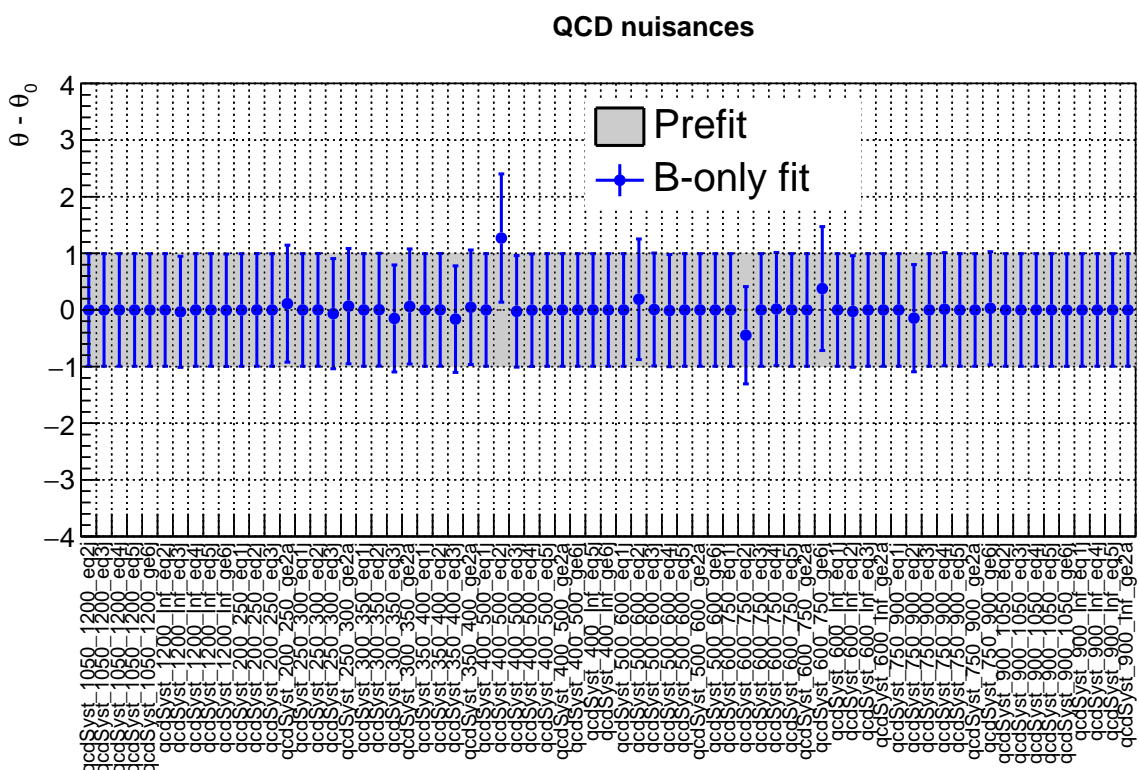


Figure B.11.: Maximum likelihood values of the nuisance parameters related to the systematic uncertainties on the QCD estimation, as determined from the background-only fit to the signal and control regions.

Bibliography

- [1] CMS Collaboration, “Search for natural and split supersymmetry in proton-proton collisions at $\sqrt{s} = 13$ TeV in final states with jets and missing transverse momentum”, [arXiv:1802.02110](https://arxiv.org/abs/1802.02110).
- [2] Particle Data Group Collaboration, “Review of Particle Physics”, *Chinese Physics C* **40** (2016), no. 10, 100001.
- [3] P. W. Higgs, “Broken symmetries and the masses of gauge bosons”, *Phys. Rev. Lett.* **13** (1964) 508, doi:[10.1103/PhysRevLett.13.508](https://doi.org/10.1103/PhysRevLett.13.508).
- [4] F. Englert and R. Brout, “Broken symmetry and the mass of gauge vector mesons”, *Phys. Rev. Lett.* **13** (1964) 321, doi:[10.1103/PhysRevLett.13.321](https://doi.org/10.1103/PhysRevLett.13.321).
- [5] G. S. Guralnik, C. R. Hagen, and T. W. B. Kibble, “Global conservation laws and massless particles”, *Phys. Rev. Lett.* **13** (1964) 585, doi:[10.1103/PhysRevLett.13.585](https://doi.org/10.1103/PhysRevLett.13.585).
- [6] CMS Collaboration, “Observation of a new boson at a mass of 125 GeV with the CMS experiment at the LHC”, *Phys. Lett.* **B716** (2012) 30–61, doi:[10.1016/j.physletb.2012.08.021](https://doi.org/10.1016/j.physletb.2012.08.021), [arXiv:1207.7235](https://arxiv.org/abs/1207.7235).
- [7] ATLAS Collaboration, “Observation of a new particle in the search for the Standard Model Higgs boson with the ATLAS detector at the LHC”, *Phys. Lett.* **B716** (2012) 1–29, doi:[10.1016/j.physletb.2012.08.020](https://doi.org/10.1016/j.physletb.2012.08.020), [arXiv:1207.7214](https://arxiv.org/abs/1207.7214).
- [8] Planck Collaboration, “Planck 2015 results. XIII. Cosmological parameters”, *Astron. Astrophys.* **594** (2016) A13, doi:[10.1051/0004-6361/201525830](https://doi.org/10.1051/0004-6361/201525830), [arXiv:1502.01589](https://arxiv.org/abs/1502.01589).
- [9] F. Zwicky, “On The Masses of Nebulae and of Clusters of Nebulae”, *The Astrophysical Journal* **86** (1937), no. 3,

- [10] A. Bergmann, V. Petrosian, and R. Lynds, “Gravitational lens models of arcs in clusters”, *The Astrophysical Journal* **350** (1990) 23–25.
- [11] G. Hinshaw, D. Larson, E. Komatsu et al., “Nine-year Wilkinson Microwave Anisotropy Probe (WMAP) Observations: Cosmological Parameter Results”, *The Astrophysical Journal Supplement Series* **208** (2013), no. 2, 19.
- [12] D. Clowe et al., “A direct empirical proof of the existence of dark matter”, *The Astrophysical Journal* **648** (2006) L109–L113 [arXiv:astro-ph/0608407].
- [13] G. Steigman and M. S. Turner, “Cosmological Constraints on the Properties of Weakly Interacting Massive Particles”, *Nuclear Physics B* **253** (1985) 375–386.
- [14] SNO Collaboration, “Measurement of the Rate of $\nu_e + d \rightarrow p + p + e^-$ Interactions Produced by 8B Solar Neutrinos at the Sudbury Neutrino Observatory”, *Phys. Rev. Lett.* **87** (Jul, 2001) 071301, doi:10.1103/PhysRevLett.87.071301.
- [15] Super-Kamiokande Collaboration, “Evidence for oscillation of atmospheric neutrinos”, *Phys. Rev. Lett.* **81** (1998) 1562–1567, doi:10.1103/PhysRevLett.81.1562, arXiv:hep-ex/9807003.
- [16] S. P. Martin, “A Supersymmetry Primer”, doi:10.1142/9789812839657_0001, arXiv:hep-ph/9709356. [Adv. Ser. Direct. High Energy Phys.18,1(1998)].
- [17] C. Csaki, “The Minimal supersymmetric standard model (MSSM)”, *Mod. Phys. Lett. A* **11** (1996) 599, doi:10.1142/S021773239600062X, arXiv:hep-ph/9606414.
- [18] Super-Kamiokande Collaboration, “Search for Proton Decay via $p \rightarrow e^+ \pi^0$ and $p \rightarrow \mu^+ \pi^0$ in a Large Water Cherenkov Detector”, *Phys. Rev. Lett.* **102** (2009) 141801, doi:10.1103/PhysRevLett.102.141801, arXiv:0903.0676.
- [19] M. Carena, D. Choudhury, R. A. Diaz et al., “Top-squark searches at the Fermilab Tevatron in models of low-energy supersymmetry breaking”, *Phys. Rev. D* **66** (Dec, 2002) 115010, doi:10.1103/PhysRevD.66.115010.
- [20] R. Barbier, C. Bérat, M. Besançon et al., “R-Parity-violating supersymmetry”, *Physics Reports* **420** (2005), no. 1, 1 – 195, doi:<https://doi.org/10.1016/j.physrep.2005.08.006>.
- [21] M. J. Strassler and K. M. Zurek, “Echoes of a hidden valley at hadron

- colliders”, *Physics Letters B* **651** (2007), no. 5, 374 – 379,
doi:<https://doi.org/10.1016/j.physletb.2007.06.055>.
- [22] N. Arkani-Hamed and S. Dimopoulos, “Supersymmetric unification without low energy supersymmetry and signatures for fine-tuning at the LHC”, *Journal of High Energy Physics* **2005** (2005), no. 06, 073.
- [23] G. Giudice and A. Romanino, “Split supersymmetry”, *Nuclear Physics B* **706** (2005), no. 1, 487,
doi:<https://doi.org/10.1016/j.nuclphysb.2004.11.048>.
- [24] M. Fairbairn, A. Kraan, D. Milstead et al., “Stable massive particles at colliders”, *Physics Reports* **438** (2007), no. 1, 1 – 63,
doi:<https://doi.org/10.1016/j.physrep.2006.10.002>.
- [25] J. Alwall, P. Schuster, and N. Toro, “Simplified Models for a First Characterization of New Physics at the LHC”, *Phys. Rev.* **D79** (2009) 075020,
doi:[10.1103/PhysRevD.79.075020](https://doi.org/10.1103/PhysRevD.79.075020), arXiv:0810.3921.
- [26] LHC New Physics Working Group Collaboration, “Simplified Models for LHC New Physics Searches”, *J. Phys.* **G39** (2012) 105005,
doi:[10.1088/0954-3899/39/10/105005](https://doi.org/10.1088/0954-3899/39/10/105005), arXiv:1105.2838.
- [27] CMS Collaboration, “Search for new phenomena with the M_{T2} variable in the all-hadronic final state produced in proton-proton collisions at $\sqrt{s} = 13$ TeV”, *Eur. Phys. J.* **C77** (2017), no. 10, 710, doi:[10.1140/epjc/s10052-017-5267-x](https://doi.org/10.1140/epjc/s10052-017-5267-x), arXiv:1705.04650.
- [28] CMS Collaboration, “Search for supersymmetry in multijet events with missing transverse momentum in proton-proton collisions at 13 TeV”, *Phys. Rev.* **D96** (2017), no. 3, 032003, doi:[10.1103/PhysRevD.96.032003](https://doi.org/10.1103/PhysRevD.96.032003), arXiv:1704.07781.
- [29] CMS Collaboration, “Search for direct production of supersymmetric partners of the top quark in the all-jets final state in proton-proton collisions at $\sqrt{s} = 13$ TeV”, *JHEP* **10** (2017) 005, doi:[10.1007/JHEP10\(2017\)005](https://doi.org/10.1007/JHEP10(2017)005), arXiv:1707.03316.
- [30] CMS Collaboration, “Search for top squark pair production in pp collisions at $\sqrt{s} = 13$ TeV using single lepton events”, *JHEP* **10** (2017) 019, doi:[10.1007/JHEP10\(2017\)019](https://doi.org/10.1007/JHEP10(2017)019), arXiv:1706.04402.

- [31] CMS Collaboration, “Search for top squarks and dark matter particles in opposite-charge dilepton final states at $\sqrt{s} = 13$ TeV”, *Phys. Rev.* **D97** (2018), no. 3, 032009, doi:10.1103/PhysRevD.97.032009, arXiv:1711.00752.
- [32] ATLAS Collaboration, “Search for long-lived, massive particles in events with displaced vertices and missing transverse momentum in $\sqrt{s} = 13$ TeV pp collisions with the ATLAS detector”, arXiv:1710.04901.
- [33] CMS Collaboration, “Search for decays of stopped exotic long-lived particles produced in proton-proton collisions at $\sqrt{s} = 13$ TeV”, *Submitted to: JHEP* (2017) arXiv:1801.00359.
- [34] CMS Collaboration, “Search for heavy stable charged particles with 12.9 fb^{-1} of 2016 data”,,
- [35] C. Lefèvre, “The CERN accelerator complex. Complexe des accélérateurs du CERN”, (Dec, 2008).
- [36] CMS Collaboration, “The CMS experiment at the CERN LHC”, *JINST* **3** (2008) S08004, doi:10.1088/1748-0221/3/08/S08004.
- [37] ATLAS Collaboration, “The ATLAS Experiment at the CERN Large Hadron Collider”, *JINST* **3** (2008) S08003, doi:10.1088/1748-0221/3/08/S08003.
- [38] LHCb Collaboration, “The LHCb Detector at the LHC”, *JINST* **3** (2008) S08005, doi:10.1088/1748-0221/3/08/S08005.
- [39] ALICE Collaboration, “The ALICE experiment at the CERN LHC”, *JINST* **3** (2008) S08002, doi:10.1088/1748-0221/3/08/S08002.
- [40] CMS Collaboration, “The CMS barrel calorimeter response to particle beams from 2 to 350 GeV”, *Eur. Phys. J.* **C60** (200) 359–373, doi:10.1140/epjc/s10052-009-0959-5.
- [41] CMS Collaboration, “CMS computing: Technical Design Report”, technical report, CERN, Geneva, (2005).
- [42] CMS Collaboration Collaboration, “Particle-flow reconstruction and global event description with the CMS detector. Particle-flow reconstruction and global event description with the CMS detector”, *JINST* **12** (Jun, 2017) P10003. 82 p.

- [43] CMS Collaboration, “Description and performance of track and primary-vertex reconstruction with the CMS tracker”, *JINST* **9** (2014), no. 10, P10009, doi:10.1088/1748-0221/9/10/P10009, arXiv:1405.6569.
- [44] W. Adam, R. Frühwirth, A. Strandlie et al., “Reconstruction of Electrons with the Gaussian-Sum Filter in the CMS Tracker at the LHC”, Technical Report CMS-NOTE-2005-001, CERN, Geneva, (Jan, 2005).
- [45] M. Cacciari, G. P. Salam, and G. Soyez, “The anti- kt jet clustering algorithm”, *Journal of High Energy Physics* **2008** (2008), no. 04, 063.
- [46] T. C. Collaboration, “Determination of jet energy calibration and transverse momentum resolution in CMS”, *Journal of Instrumentation* **6** (2011), no. 11, P11002.
- [47] CMS Collaboration, “Identification of heavy-flavour jets with the CMS detector in pp collisions at 13 TeV”, (2017). arXiv:1712.07158. Submitted to JINST.
- [48] J. Alwall, M. Herquet, F. Maltoni et al., “MadGraph 5 : Going Beyond”, *JHEP* **06** (2011) 128, doi:10.1007/JHEP06(2011)128, arXiv:1106.0522.
- [49] S. Alioli, P. Nason, C. Oleari et al., “A general framework for implementing NLO calculations in shower Monte Carlo programs: the POWHEG BOX”, *JHEP* **06** (2010) 043, doi:10.1007/JHEP06(2010)043, arXiv:1002.2581.
- [50] T. Sjöstrand, S. Ask, J. R. Christiansen et al., “An Introduction to PYTHIA 8.2”, *Comput. Phys. Commun.* **191** (2015) 159–177, doi:10.1016/j.cpc.2015.01.024, arXiv:1410.3012.
- [51] GEANT4 Collaboration, “GEANT4: A Simulation toolkit”, *Nucl. Instrum. Meth.* **A506** (2003) 250–303, doi:10.1016/S0168-9002(03)01368-8.
- [52] CMS Collaboration, “Search for Supersymmetry at the LHC in Events with Jets and Missing Transverse Energy”, *Phys. Rev. Lett.* **107** (2011) 221804, doi:10.1103/PhysRevLett.107.221804, arXiv:1109.2352.
- [53] CMS Collaboration, “Search for Supersymmetry in pp Collisions at 7 TeV in Events with Jets and Missing Transverse Energy”, *Phys. Lett.* **B698** (2011) 196–218, doi:10.1016/j.physletb.2011.03.021, arXiv:1101.1628.
- [54] CMS Collaboration, “Search for supersymmetry in final states with missing

- transverse energy and 0, 1, 2, or at least 3 b-quark jets in 7 TeV pp collisions using the variable alphaT”, *JHEP* **01** (2013) 077,
`doi:10.1007/JHEP01(2013)077`, `arXiv:1210.8115`.
- [55] CMS Collaboration, “Search for supersymmetry in hadronic final states with missing transverse energy using the variables α_T and b-quark multiplicity in pp collisions at $\sqrt{s} = 8$ TeV”, *Eur. Phys. J.* **C73** (2013), no. 9, 2568,
`doi:10.1140/epjc/s10052-013-2568-6`, `arXiv:1303.2985`.
- [56] CMS Collaboration, “A search for new phenomena in pp collisions at $\sqrt{s} = 13$ TeV in final states with missing transverse momentum and at least one jet using the α_T variable”, *Eur. Phys. J. C* **77** (2017) 294,
`doi:10.1140/epjc/s10052-017-4787-8`, `arXiv:1611.00338`.
- [57] CMS Collaboration, “Performance of missing energy reconstruction in 13 TeV pp collision data using the CMS detector”, Technical Report CMS PAS JME-16-004, CERN, Geneva, (2016).
- [58] L. Randall and D. Tucker-Smith, “Dijet Searches for Supersymmetry at the LHC”, *Phys. Rev. Lett.* **101** (2008) 221803,
`doi:10.1103/PhysRevLett.101.221803`, `arXiv:0806.1049`.
- [59] CMS Collaboration, “Public CMS Data Quality Information”.
- [60] J. Alwall, R. Frederix, S. Frixione et al., “The automated computation of tree-level and next-to-leading order differential cross sections, and their matching to parton shower simulations”, *JHEP* **07** (2014) 079,
`doi:10.1007/JHEP07(2014)079`, `arXiv:1405.0301`.
- [61] CMS Collaboration, “The fast simulation of the CMS detector at LHC”, *J. Phys. Conf. Ser.* **331** (2011) 032049, `doi:10.1088/1742-6596/331/3/032049`.
- [62] A. C. Kraan, “Interactions of heavy stable hadronizing particles”, *Eur. Phys. J. C* **37** (2004) 91, `doi:10.1140/epjc/s2004-01946-6`, `arXiv:hep-ex/0404001`.
- [63] R. Mackeprang and A. Rizzi, “Interactions of Coloured Heavy Stable Particles in Matter”, *Eur. Phys. J. C* **50** (2007) 353,
`doi:10.1140/epjc/s10052-007-0252-4`, `arXiv:hep-ph/0612161`.
- [64] ATLAS Collaboration, “Measurement of the Inelastic Proton-Proton Cross Section at $\sqrt{s} = 13$ TeV with the ATLAS Detector at the LHC”, *Phys. Rev. Lett.*

- 117** (2016) 182002, doi:10.1103/PhysRevLett.117.182002,
arXiv:1606.02625.
- [65] CMS Collaboration, “Identification of b quark jets at the CMS Experiment in the LHC Run 2”, Technical Report CMS-PAS-BTV-15-001, CERN, Geneva, (2016).
- [66] CMS Collaboration, “Generic Tag and Probe Tool for Measuring Efficiency at CMS with Early Data”, Technical Report CMS AN-2009/111, CERN, (2009).
- [67] CMS Collaboration, “Search for new physics in final states with an energetic jet or a hadronically decaying W or Z boson and transverse momentum imbalance at $\sqrt{s} = 13$ TeV”, arXiv:1712.02345.
- [68] Z. Bern et al., “Left-Handed W Bosons at the LHC”, *Phys. Rev.* **D84** (2011) 034008, doi:10.1103/PhysRevD.84.034008, arXiv:1103.5445.
- [69] CMS Collaboration, “CMS Luminosity Measurement for the 2015 Data Taking Period”, CMS Physics Analysis Summary CMS-PAS-LUM-15-001, CERN, (2016).
- [70] J. S. Conway, “Incorporating Nuisance Parameters in Likelihoods for Multisource Spectra”, arXiv:1103.0354.
- [71] ATLAS and CMS Collaborations, and LHC Higgs Combination Group, “Procedure for the LHC Higgs boson search combination in Summer 2011”, Technical Report CMS-NOTE-2011-005 ATL-PHYS-PUB-2011-11, CERN, Geneva, (2011).
- [72] T. Junk, “Confidence level computation for combining searches with small statistics”, *Nucl. Instr. Meth. A* **434** (1999) 435, doi:10.1016/S0168-9002(99)00498-2, arXiv:hep-ex/9902006.
- [73] A. L. Read, “Presentation of search results: the CL_s technique”, *J. Phys. G* **28** (2002) 2693, doi:10.1088/0954-3899/28/10/313.
- [74] G. Cowan, K. Cranmer, E. Gross et al., “Asymptotic formulae for likelihood-based tests of new physics”, *Eur. Phys. J. C* **71** (2011) 1554, doi:10.1140/epjc/s10052-011-1554-0, arXiv:1007.1727.

List of figures

2.1. Feynman diagram of long-lived gluino pair production, with each gluino decaying as $\tilde{g} \rightarrow q\bar{q}\tilde{\chi}_1^0$ via a virtual squark \tilde{q}^*	12
3.1. The accelerator complex at CERN leading to the LHC [35]. The various accelerators (LINAC 2, PSB, PS, SPS, LHC) and detectors (CMS, ATLAS, LHCb, ALICE) are described in the text.	15
3.2. Layout of the major components within the CMS detector. These are described in the text.	17
3.3. One quarter cross-sectional view (in the r - z plane) of the CMS detector, indicating lines of constant pseudorapidity and the dimensions of various components.	17
3.4. Schematic cross-sectional view (in the r - z plane) of the CMS tracker [36]. The tracker modules are indicated by the black line segments. . . .	18
3.5. Schematic cross-sectional view (in the r - z plane) of the CMS electromagnetic calorimeter, showing the arrangement of crystals in the barrel, endcap and preshower [36].	19
3.6. One quarter cross-sectional view (in the r - z plane) of the CMS detector, showing the location of the hadronic calorimeter barrel (HB), endcap (HE), outer (HO), and forward (HF) regions [36].	20
3.7. One quarter cross-sectional view (in the r - z plane) of the CMS muon system, showing the location of the drift tube (DT), cathode strip chamber (CSC) and resistive plate chamber (RPC) subsystems [36].	21

3.8. Distribution of the discriminator value of the CSV b-tagging algorithm for jets of different flavours in simulated $t\bar{t}$ events [47]. Jets without at least two tracks are assigned a default value of -1 and are included in the first bin, which contains the underflow entries.	28
4.1. The leading jet's charged hadron energy fraction (left) and ϕ direction before (centre) and after (right) applying a requirement of $f_{\text{CH}} > 0.1$. The large excess in data at f_{CH} values close to zero and $\phi = 0$ and π is consistent with beam halo effects, and is effectively suppressed by the f_{CH} requirement.	38
4.2. The distribution of the α_T variable in data and simulation for events satisfying the signal region selections (Sec. 4.5) except the α_T requirement, plus the additional requirements $n_{\text{jet}} \geq 2$, $p_T^{j_2} > 100$ GeV, and $H_T > 900$ GeV. The ability of the variable to effectively discriminate between QCD processes and processes with genuine missing energy is evidenced by the sharp edge at 0.5.	43
4.3. The distribution of the $\Delta\phi_{\min}^*$ variable in data and simulation for events satisfying the signal region selections (Sec. 4.5) except the $\Delta\phi_{\min}^*$ requirement, plus the additional requirements $n_{\text{jet}} \geq 2$, $p_T^{j_2} > 100$ GeV, and $H_T > 900$ GeV. The ability of the variable to effectively discriminate between QCD processes and processes with genuine missing energy is evidenced by the cluster of QCD events close to 0, while processes with genuine E_T take on larger values up to π radians.	45
4.4. The distribution of the \cancel{H}_T/E_T ratio in simulation for events satisfying the signal region selections (Sec. 4.5) except the \cancel{H}_T/E_T requirement. The ability of the variable to effectively discriminate between QCD processes and processes with genuine missing energy is evidenced by the population of QCD events above 1.25, while processes with genuine E_T have values more consistent with unity.	46
4.5. Efficiency of the logical disjunction of the HL triggers in the signal region as a function of offline \cancel{H}_T and H_T , measured in a data sample collected by a single electron (left) and single muon (right) trigger. Note that only events with $\cancel{H}_T > 200$ GeV are selected for the signal region.	59

4.6. Cumulative integrated luminosity of pp collisions at $\sqrt{s} = 13$ TeV delivered by the LHC, recorded by CMS, and certified as good for physics analysis per day during the year 2016 [59].	60
4.7. Distribution of the number of pileup interactions in the Monte Carlo (MC) simulation and in data. The ratio of the two is used to derive correction factors that are used to weight the simulated events. The corrected simulated distribution is also shown.	63
4.8. Result of the tag-and-probe dimuon invariant mass fitting procedure to passing (left) and failing (right) probes for an example isolation efficiency measurement in data for muons with $50 < p_T < 60$ GeV. The blue (red) curves are the fitted signal (background) distributions. The fitted efficiency in this example is 96.0%.	67
4.9. The data-to-simulation ratio of event counts as a function of H_T for two example (n_{jet} , n_b , H_T) categories, along with the fit of a linear (and constant) function.	75
4.10. The distribution of the z-scores of the linear parameter fitted to the H_T distributions for all (n_{jet} , n_b , H_T) categories in both the $\mu + \text{jets}$ and $\mu\mu + \text{jets}$ control regions. A fitted Gaussian distribution is overlaid.	76
4.11. The estimated number of QCD events in each (n_{jet} , H_T) bin of the signal region (top), and the corresponding ratio of expected QCD and electroweak events (bottom).	78
4.12. The ratio of the $T(\mu \rightarrow W/t\bar{t})$ (top) and $T(\mu\mu \rightarrow Z)$ (bottom) transfer factors in each (n_{jet} , n_b , H_T) bin when varying the pileup correction factors by $+1\sigma$ (left) and -1σ (right) with respect to their nominal values.	80
4.13. Closure tests relating to extrapolations in α_T (top), $\Delta\phi_{\min}^*$ (middle), and W boson polarisation (bottom), as a function of H_T (left) and n_{jet} (right). The level of closure obtained via a maximum likelihood method is indicated by the open circles. The blue lines represent the resulting systematic uncertainties that are assigned to the relevant transfer factors. A linear fit is also shown.	86

5.1. Expected signal events for split SUSY simplified models with a range of values of $(c\tau, m_{\tilde{g}}, m_{\tilde{\chi}_1^0})$, overlaid on the expected standard model background counts, using an aggregated binning scheme.	90
5.2. Efficiency of the b-tagging algorithm for displaced jets originating from long-lived gluinos, compared to standard model bottom and light quarks, for jets with $100 < p_T < 140$ and $0 < \eta < 0.5$	92
5.3. Number of events observed (solid markers) and expected number of Z, W/t̄ and QCD background events (histograms, with shaded bands representing the statistical and systematic uncertainties) in every n_b , H_T and \mathcal{H}_T bin of the jet categories $n_{jet} = 1, \geq 2a$ (top), $n_{jet} = 2$ (middle), and $n_{jet} = 3$ (bottom), as determined from the maximum likelihood fit to the control regions. The centre panel of each sub-figure shows the ratios of the observed and expected counts, while the lower panel shows the corresponding z-score, as defined in the text.	97
5.4. Number of events observed (solid markers) and expected number of Z, W/t̄ and QCD background events (histograms, with shaded bands representing the statistical and systematic uncertainties) in every n_b , H_T and \mathcal{H}_T bin of the jet categories $n_{jet} = 4$ (top), $n_{jet} = 5$ (middle), and $n_{jet} \geq 6$ (bottom), as determined from the background-only maximum likelihood fit to the control regions. The centre panel of each sub-figure shows the ratios of the observed and expected counts, while the lower panel shows the corresponding z-score, as defined in the text.	98
5.5. Histograms of the ratios of the observed and expected event counts (left) and corresponding z-scores (right), as defined in the text, for all (n_{jet}, n_b, H_T) bins, as determined from the background-only maximum likelihood fit to the control regions.	99

- 5.6. Observed and expected mass exclusions at 95% confidence level (indicated by solid and dashed contours, respectively) for various families of simplified models. The upper subfigure summarises the mass exclusions for five model families that involve the direct pair production of squarks (T2bb, T2tt, T2cc, T2qq_8fold and T2qq_1fold). The grey shaded region denotes T2tt models that are not considered for interpretation. The lower subfigure includes three models that involve the production and prompt decay of gluino pairs (T1bbbb, T1tttt, and T1qqqq). A final scenario involves the production of gluinos that are assumed to be metastable on the detector scale (T1qqqqLL). 102
- 5.7. Observed upper limit in cross section at 95% confidence level (indicated by the colour scale) as a function of the \tilde{g} and $\tilde{\chi}_1^0$ masses for the split SUSY simplified models. Each subfigure represents a different gluino lifetime. The thick (thin) black line indicates the observed excluded region assuming the nominal ($\pm 1\sigma$ in theoretical cross section uncertainty) production cross section. The red dashed (dashed and dotted) represents the median ($\pm 1\sigma$ and $\pm 2\sigma$ in experimental uncertainty) expected excluded region. 105
- 5.8. Observed upper limit in cross section at 95% confidence level (indicated by the colour scale) as a function of the \tilde{g} and $\tilde{\chi}_1^0$ masses for the split SUSY simplified models. Each subfigure represents a different gluino lifetime. The thick (thin) black line indicates the observed excluded region assuming the nominal ($\pm 1\sigma$ in theoretical cross section uncertainty) production cross section. The red dashed (dashed and dotted) represents the median ($\pm 1\sigma$ and $\pm 2\sigma$ in experimental uncertainty) expected excluded region. 106
- 5.9. Observed upper limit in cross section at 95% confidence level (indicated by the colour scale) as a function of the \tilde{g} and $\tilde{\chi}_1^0$ masses for the slit SUSY simplified models. Each subfigure represents a different gluino lifetime. The thick (thin) black line indicates the observed excluded region assuming the nominal ($\pm 1\sigma$ in theoretical cross section uncertainty) production cross section. The red dashed (dashed and dotted) represents the median ($\pm 1\sigma$ and $\pm 2\sigma$ in experimental uncertainty) expected excluded region. 107

5.10. Summary of observed and expected excluded regions at 95% confidence level as a function of the \tilde{g} and $\tilde{\chi}_1^0$ masses for various gluino lifetimes for the split SUSY simplified models.	108
5.11. Observed and expected lower limit at 95% confidence level on $m_{\tilde{g}}$ as a function of the gluino's lifetime for fixed $m_{\tilde{\chi}_1^0} = 100$ GeV and for $m_{\tilde{g}} - m_{\tilde{\chi}_1^0} = 100$ GeV. The cases of a prompt and metastable gluino are also indicated.	109
A.1. The ratio of the $T(\mu \rightarrow W/t\bar{t})$ (top) and $T(\mu\mu \rightarrow Z)$ (bottom) transfer factors in each $(n_{\text{jet}}, n_b, H_T)$ bin when varying the pileup correction factors by $+1\sigma$ (left) and -1σ (right) with respect to their nominal values.	113
A.2. The ratio of the $T(\mu \rightarrow W/t\bar{t})$ (top) and $T(\mu\mu \rightarrow Z)$ (bottom) transfer factors in each $(n_{\text{jet}}, n_b, H_T)$ bin when varying the jet energy correction factors by $+1\sigma$ (left) and -1σ (right) with respect to their nominal values.	114
A.3. The ratio of the $T(\mu \rightarrow W/t\bar{t})$ (top) and $T(\mu\mu \rightarrow Z)$ (bottom) transfer factors in each $(n_{\text{jet}}, n_b, H_T)$ bin when varying the b-tagging correction factors for bottom and charm quarks by $+1\sigma$ (left) and -1σ (right) with respect to their nominal values.	115
A.4. The ratio of the $T(\mu \rightarrow W/t\bar{t})$ (top) and $T(\mu\mu \rightarrow Z)$ (bottom) transfer factors in each $(n_{\text{jet}}, n_b, H_T)$ bin when varying the b-tagging correction factors for light partons (u, d, s, gluon) by $+1\sigma$ (left) and -1σ (right) with respect to their nominal values.	116
A.5. The ratio of the $T(\mu \rightarrow W/t\bar{t})$ (top) and $T(\mu\mu \rightarrow Z)$ (bottom) transfer factors in each $(n_{\text{jet}}, n_b, H_T)$ bin when varying the trigger correction factors by $+1\sigma$ (left) and -1σ (right) with respect to their nominal values.	117
A.6. The ratio of the $T(\mu \rightarrow W/t\bar{t})$ (top) and $T(\mu\mu \rightarrow Z)$ (bottom) transfer factors in each $(n_{\text{jet}}, n_b, H_T)$ bin when varying the boson p_T dependent NLO correction factors by $+1\sigma$ (left) and -1σ (right) with respect to their nominal values.	118

A.7. The ratio of the $T(\mu \rightarrow W/t\bar{t})$ (top) and $T(\mu\mu \rightarrow Z)$ (bottom) transfer factors in each $(n_{\text{jet}}, n_b, H_T)$ bin when varying the $t\bar{t}$ ISR correction factors by $+1\sigma$ (left) and -1σ (right) with respect to their nominal values.	119
A.8. The ratio of the $T(\mu \rightarrow W/t\bar{t})$ (top) and $T(\mu\mu \rightarrow Z)$ (bottom) transfer factors in each $(n_{\text{jet}}, n_b, H_T)$ bin when varying the W cross section correction factors by $+1\sigma$ (left) and -1σ (right) with respect to their nominal values.	120
A.9. The ratio of the $T(\mu \rightarrow W/t\bar{t})$ (top) and $T(\mu\mu \rightarrow Z)$ (bottom) transfer factors in each $(n_{\text{jet}}, n_b, H_T)$ bin when varying the $t\bar{t}$ cross section correction factors by $+1\sigma$ (left) and -1σ (right) with respect to their nominal values.	121
B.1. Number of events observed (solid markers) and expected number of Z , $W/t\bar{t}$ and QCD background events (histograms, with shaded bands representing the statistical and systematic uncertainties) in every n_b , H_T and \cancel{H}_T bin of the jet categories $n_{\text{jet}} = 1, \geq 2a$ (top), $n_{\text{jet}} = 2$ (middle), and $n_{\text{jet}} = 3$ (bottom), as determined from the maximum likelihood fit to the signal and control regions. The centre panel of each sub-figure shows the ratios of the observed and expected counts, while the lower panel shows the corresponding z-score, as defined in the text.	131
B.2. Number of events observed (solid markers) and expected number of Z , $W/t\bar{t}$ and QCD background events (histograms, with shaded bands representing the statistical and systematic uncertainties) in every n_b , H_T and \cancel{H}_T bin of the jet categories $n_{\text{jet}} = 4$ (top), $n_{\text{jet}} = 5$ (middle), and $n_{\text{jet}} \geq 6$ (bottom), as determined from the background-only maximum likelihood fit to the signal and control regions. The centre panel of each sub-figure shows the ratios of the observed and expected counts, while the lower panel shows the corresponding z-score, as defined in the text.	132

B.3. Maximum likelihood values of the nuisance parameters related to the systematic uncertainties derived from variations in the simulation correction factors, as determined from the background-only fit to the signal and control regions. From left to right: p_T dependent NLO QCD+EWK corrections; b-tagging efficiency for light and heavy quarks; jet energy; lepton identification, isolation and trigger; ISR jets; pileup; signal region triggers; W and $t\bar{t}$ cross sections.	133
B.4. Maximum likelihood values of the nuisance parameters related to the systematic uncertainties derived from the α_T closure tests, as determined from the background-only fit to the signal and control regions.	134
B.5. Maximum likelihood values of the nuisance parameters related to the systematic uncertainties derived from the $\Delta\phi_{\min}^*$ closure tests, as determined from the background-only fit to the signal and control regions.	134
B.6. Maximum likelihood values of the nuisance parameters related to the systematic uncertainties derived from the W^+/W^- closure tests, as determined from the background-only fit to the signal and control regions.	135
B.7. Maximum likelihood values of the nuisance parameters related to the H_T -dependent systematic uncertainties on the \mathcal{H}_T shape of the $W/t\bar{t}$ processes, as determined from the background-only fit to the signal and control regions.	136
B.8. Maximum likelihood values of the nuisance parameters related to the n_{jet} -dependent systematic uncertainties on the \mathcal{H}_T shape of the $W/t\bar{t}$ processes, as determined from the background-only fit to the signal and control regions.	136
B.9. Maximum likelihood values of the nuisance parameters related to the H_T -dependent systematic uncertainties on the \mathcal{H}_T shape of the $Z(\rightarrow \nu\nu) + \text{jets}$ process, as determined from the background-only fit to the signal and control regions.	137

B.10. Maximum likelihood values of the nuisance parameters related to the n_{jet} -dependent systematic uncertainties on the \mathcal{H}_T shape of the $Z(\rightarrow \nu\nu) + \text{jets}$ process, as determined from the background-only fit to the signal and control regions.	137
B.11. Maximum likelihood values of the nuisance parameters related to the systematic uncertainties on the QCD estimation, as determined from the background-only fit to the signal and control regions.	138

List of tables

2.1.	Fundamental particles of the standard model of particles physics and some of their properties [2].	4
2.2.	Supersymmetric particles (observable mass eigenstates) within the MSSM and their spin quantum numbers. The first and second groups are the sfermions and (superpositions of) gauginos, respectively. The Higgs bosons are superpositions of higgsinos.	8
2.3.	Summary of the simplified SUSY models used to interpret the result of this search.	12
4.1.	The p_T and η thresholds for physics objects that are used to either select events or veto them.	33
4.2.	Quality requirements imposed on the constituents of jets.	34
4.3.	Summary of selections as part of the definition of the signal and control regions.	47
4.4.	The α_T thresholds as a function of H_T for events containing at least two jets. No requirement is made on events containing only one jet.	48
4.5.	The definitions of the sideband regions employed in the estimation of the QCD background.	50

4.6. Summary of all bins in the signal region. The listed numbers correspond to the lower boundaries of the \mathcal{H}_T bins in each $(n_{\text{jet}}, n_b, H_T)$ bin; the final number in the list is always an open bin. A single-element list is equivalent to no binning in \mathcal{H}_T . A dash means a particular $(n_{\text{jet}}, n_b, H_T)$ bin is not used, and so the previous H_T bin (if applicable) is an open bin. The muon control regions are binned identically, except that they are not binned in \mathcal{H}_T , and the largest n_b category in the $\mu\mu + \text{jets}$ control region is ≥ 1	52
4.7. List of L1 and HL triggers utilised in this search, grouped by family, indicating in parentheses their varying thresholds throughout the 2016 LHC run. All quantities related to energy and momentum are quoted in GeV units. The muon trigger is employed in the muon control regions, while all other triggers listed are employed in the signal region and hadronic control regions. The $H_T\text{-}\alpha_T$ triggers also have a minimum requirement of 90 GeV on the average p_T of the two leading jets, which did not change throughout run. Also provided is the fraction of the 2016 run for which a given trigger version was the lowest-threshold unprescaled trigger.	56
4.8. Cross section correction factors for the three dominant standard model background processes, along with an indication of the most constraining sideband region for each process.	70
4.9. Summary of systematic uncertainties on the $T(\mu \rightarrow W/t\bar{t})$ and $T(\mu\mu \rightarrow Z)$ transfer factors, derived from variations of the data-to-simulation correction factors (Sec. 4.12.1) and data-driven closure tests (Sec. 4.12.2). The quoted ranges correspond to the $\pm 1\sigma$ quantiles of the transfer factor changes across all $(n_{\text{jet}}, n_b, H_T)$ bins.	79
5.1. Summary of uncertainties (%) on the simplified long-lived gluino models for various values of $(m_{\tilde{g}}, m_{\tilde{\chi}_1^0})$ [GeV]. The quoted ranges correspond to the $\pm 1\sigma$ quantiles of the yield changes across all $(n_{\text{jet}}, n_b, H_T, \mathcal{H}_T)$ bins.	91
5.2. Summary of the observed largest excluded mass at 95% confidence level for the parent SUSY particle (gluino or squark) and the LSP ($\tilde{\chi}_1^0$), for each family of simplified models.	101

B.1. Observed data counts and background expectations from the background-only likelihood fit to the control regions, for the $n_{\text{jet}} = 1$ category. The uncertainties in the background expectations include statistical as well as systematic contributions.	123
B.2. Observed data counts and background expectations from the background-only likelihood fit to the control regions, for the $n_{\text{jet}} \geq 2$ category. The uncertainties in the background expectations include statistical as well as systematic contributions.	124
B.3. Observed data counts and background expectations from the background-only likelihood fit to the control regions, for the $n_{\text{jet}} = 2$ category. The uncertainties in the background expectations include statistical as well as systematic contributions.	125
B.4. Observed data counts and background expectations from the background-only likelihood fit to the control regions, for the $n_{\text{jet}} = 3$ category. The uncertainties in the background expectations include statistical as well as systematic contributions.	126
B.5. Observed data counts and background expectations from the background-only likelihood fit to the control regions, for the $n_{\text{jet}} = 4$ category. The uncertainties in the background expectations include statistical as well as systematic contributions.	127
B.6. Observed data counts and background expectations from the background-only likelihood fit to the control regions, for the $n_{\text{jet}} = 5$ category. The uncertainties in the background expectations include statistical as well as systematic contributions.	128
B.7. Observed data counts and background expectations from the background-only likelihood fit to the control regions, for the $n_{\text{jet}} \geq 6$ category. The uncertainties in the background expectations include statistical as well as systematic contributions.	129